Development of an innovative PET module

Study of the performances of a LYSO crystal based detector for small PET devices

By

GIANLUCA STRINGHINI
MAT. 735984

Scuola di dottorato
UNIVERSITA' DEGLI STUDI MILANO BICOCCA
DEPARTMENT OF PHYSICS "G. OCCHIALINI"
CYCLE XXXI

ACCADEMIC YEAR 2017 / 2018

Tutor: Prof. Marco Paganoni,
Cotutor: Dott. Etiennette Auffray
Coordinator: Prof. Marta Calvi

Abstract

Positron emission tomography (PET) is a technique based on the detection of two back to back 511 keV gamma rays originated by a positron-electron annihilation. The aim of this project is to develop an innovative PET detector module with high performances, in term of spatial, energy and timing resolution while maintaining the overall complexity reasonably low. The proposed module is based on a pixellated LYSO matrix and MPPC detector. Compared to double side readout configuration in which the scintillators are read on both sides by detectors, one detector is replaced by an optical light guide and a reflector. The light collected by the second detector in the double side readout approach is instead recirculated and collected by the nearby detectors thanks to the light guide on top of the module. Enabling this light sharing mechanism allows reaching the same performances of a double side readout configuration decreasing the number of detector channels needed. Furthermore, it is possible to adopt a more than one to one coupling between scintillators and detector in order to further decrease the number of channels needed and to improve the spatial resolution of the system. Studying the shared light distribution allows identifying the crystal in which the gamma ray interaction took place. Several matrices are tested with different coupling between scintillators and detectors (one to one, four to one and nine to one) and the results show good crystals identification capabilities and an energy resolution in the order of 12% FWHM (one to one and four to one configurations) and 16% FWHM (nine o one configuration). For small animal and organ dedicated PET devices, there is a spatial resolution degradation close to the edges of the field of view (FOV) due to parallax error. This effect is mitigated by knowing the interaction position along the crystal main axis and this information is known as depth of interaction (DOI). The DOI capabilities of the proposed module are tested and a value of 3 mm FWHM DOI resolution is reached for the one to one and four to one coupling configuration. For the nine to one configuration a DOI resolution of 4 mm FWHM is obtained. In order to reach the DOI information, an attenuation behavior over the crystal length is introduced but, as drawback, it decreases the timing performances of the proposed module. A method to reduce this effect is presented by including the DOI information in the evaluation of the timing resolution. The module shows a coincidence time resolution of 353 ps FWHM.
The second part of this project is focused on the development of an image reconstruction software able to include both the DOI and timing information. The reconstruction algorithm is described and presented and a simulation study is performed in order to confirm the benefits of the DOI and timing in the image quality. Furthermore, a complete time of flight (TOF) study is performed evaluating the improvement of the signal to noise (SNR) ratio and spatial resolution as a function of the timing performances.

Dedication and acknowledgements

At the end of this PhD project, I really want to express my gratitude to my supervisor Prof. Marco Paganoni. He gave me the possibility to be part of a great research group and he supported me in every step of my first experience in the research world. Thanks to him, I had an incredible professional growth in these years being able to work at CERN, one of the most incredible research centers. I also want to thank Dott. Etiennette Auffray who supervised my activities at Lab. 27 giving me the possibility to be part of the Crystal Clear Collaboration. Her suggestions were fundamental to complete my project.
I would like to thank Dott. Marco Pizzichemi who is like a mentor for me. I learned more from him than in my entire educational experience.
I would like to express my gratitude to the CERN Knowledge Transfer Group, in particular to Dott. Manuela Cirilli, for supporting the research project. I want also to thank all the people with whom I shared the office: Giacomo, Andrea and in particular Matteo, a friend who shared with me every step of this PhD experience. A big thanks to all the "tenants" of Lab. 27. It is impossible to express my gratitude individually without writing a very long list but, thanks to them, I really enjoyed my time there.
Outside the office, I really want to thank Vittorio and Francesco, friends with whom I had the best time in Geneva. A big thank goes also to Silvia and Giuliano for the incredible time spent together. I want also to thank all my friends in Italy especially Matteo, Paolo, Alessandro and Michele. I consider them my second family.
I want also to mention my family and thank them for the incredible support they gave me in these years. And Sara, for being the best person I have by my side.

TABLE OF CONTENTS

List of Tables

List of Figures

List of acronyms

ADC - Analog to Digital Converter
APD - Avalanche PhotoDiode
CT - Computer Tomography
CTR - Coincidence Time Resolution
DOI - Depth Of Interaction
ESR - Enhanced Specular Reflector
FBP - Filter Back Projection
FDG - Fludeoxyglucose
FOV - Field Of View
FWHM - Full Width Half Maximum
LOR - Line of Response
LYSO - Lutetium yttrium orthosilicate
ML-EM - Maximum Likelihood Expectation Maximization
MPPC - MultiPixel Photon Counters
MRI - Magnetic resonance imaging
PDE - Photon Detection Efficiency
PET - Positron Emission Tomography
PMT - Photon Multiplier Tube
ROI - Region Of Interest
SiPM - Silicon Photon Multiplier
SNR - Signal to Noise Ration
SPAD - Single Photon Avalanche Diode
TDC - Time to Digital Converter
TOF - Time Of Flight
TOT - Time Over Threshold

CHAPTER 1

INTRODUCTION

Positron emission tomography (PET) is a medical examination which provides metabolical images. It plays a key role in several applications as oncology, neuroimaging, cardiology and pharmacokinetics. It relies on radio-tracer injection in the human body which follows the metabolic behavior of glucose in tissues. The radio-tracer is labeled by a positron emitter.

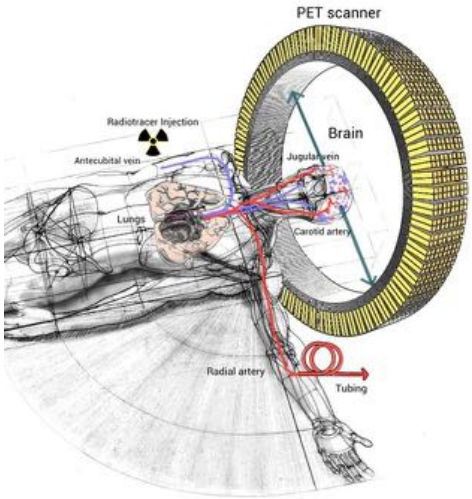

FIGURE 1.1. A pictorial scheme of the positronium state (picture from "The methodology of TSPO imaging with positron emission tomography",F. E. Turkheimer).

The positrons annihilate with human body electrons producing two 511 keV back-to-back gamma rays. If detected by a coincidence detection system, these gamma rays provide the information

about the line along which annihilation took place. The detection system is based on a scintillating material and a photodetector. The first one converts the gamma ray energy into optical light which is collected by the second one generating a voltage signal. The collection of lines, called lines of response (LORs), is processed by dedicated reconstruction algorithms that recover the activity distribution images. The radio-tracer distribution is linked to glucose concentration and, in oncology, higher consumption regions are indicators of cancer lesions.
The accuracy with which lesions are diagnosed is related to the precision of LORs identification achieved by recovering the three dimensional detection point of gamma rays. The accuracy of the interaction point determination is dominated by scintillator transverse dimensions. This precision improves by adopting smaller scintillators but this leads to a higher number of channels needed increasing the complexity and the costs of the system.
Current commercially available systems for whole body PET examination show a spatial resolution in the order of 4-6 mm. For example, Vereos and Ingenuity TF by Philips have both a transaxial and axial resolution at 1 cm of 4.7 mm and 4 mm. Discovery 710 and Discovery IQ (5 rings) show both a transaxial resolution of 4.9 mm and an axial resolution of 5.6 mm and 5.1 mm. For the Siemens Biograph mCT Flow (True V) the resolution is 4.4 mm (transaxial) and 5.9 mm (axial) [1]. For small animal and preclinical system, the spatial resolution is in the order of 1.6-2.4 mm FWHM. In particular for the Siemens devices the resolution is 2.24 mm for the microPET P4, 2.20 mm for microPET R4, 1.78 mm for the microPET Focus 120 and 1.74 for the microPET Focus 220. For the Philips Inveon scanner the resolution reaches 1.64 mm and for the ClearPET scanner by Raytest GmbH the results show a 2.02 mm resolution [2]. In small animal and organ dedicated PET scanners, knowing the interaction position along the scintillator main axis represents a fundamental information to avoid parallax error which is responsible for spatial resolution deterioration. This information, called depth of interaction (DOI), can be reached by several methods that include scintillators multilayer structure, pulse shape discrimination and double side readout configuration. In the latter method, the scintillators are read on both sides by photodetectors and the DOI is recovered by the asymmetry of collected light if there is a light attenuation behavior along the scintillator main axis.
In this study, a new approach to overcome the double side readout configuration is presented based on pixellated scintillators in a single side readout configuration. The purpose is to reduce by a factor two the number of photodetectors and electronic channels needed to detect gamma rays while maintaining the same performances of a double side readout. The idea is to replace a detector on one side with an optical light guide and a reflecting material layer as presented in Fig. 1.2.
In this single side readout configuration, the light that otherwise will escape from one scintillator end is spread by the optical light guide and recirculated by the reflecting material in the module. This light is collected by the nearby photodetectors. Enabling the optical light spread, it is possible to adopt a greater than one to one coupling between the scintillators and the photodetectors. This

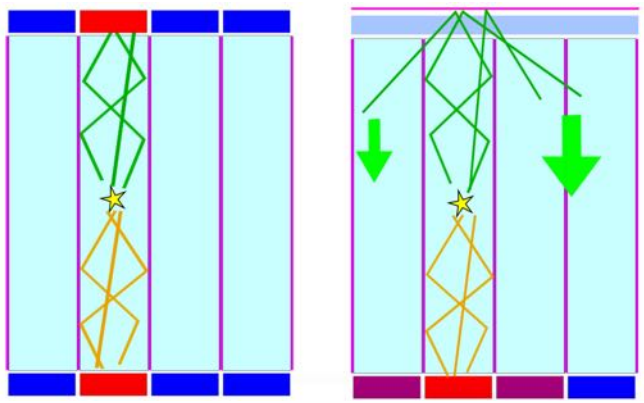

FIGURE 1.2. The light collection difference between double and single side readout configuration. In double side readout configuration, the two components of light are collected by two photodetectors (red) coupled to the hit scintillator. In single side readout approach, the light which propagates along photodetector direction (orange) is collected by the detector directly coupled while the other component (green) is spread in the others (purple) by means of the light guide and the reflecting material on top.

allows reducing the transverse scintillator dimension without increasing the number of readout channel. In this configuration, the interaction events position can be recovered by studying the light sharing behavior. Furthermore, DOI can be obtained by comparing the light collected by the directly coupled photodetector and the component shared in the nearby ones.
Attenuation behavior along the scintillator main axis is needed to evaluate DOI information but this leads to a deterioration of the system timing performances. In this work, a procedure to correct for this effect is presented by including DOI information in the detection time evaluation improving the timing resolution of the system.
In this study, a PET module prototype based on single side readout configuration is presented and tested showing high performances in term of interaction point identification, energy, DOI and timing resolution. The effect of these high performances is proven by an image reconstruction study performed by a dedicated algorithm especially developed to include both timing and DOI information.
The project was supported by the CERN Knowledge Transfer Group thanks to two KT projects ("New ClearPEM module" and "Detector module development for Whole Body PET").

CHAPTER 2

POSITRON EMISSION TOMOGRAPHY

PET principles are presented in this chapter with particular attention to radio-tracer description, positron-electron annihilation process, gamma ray detection and classification of coincidence events. The fifth section is dedicated to factors which influence the spatial resolution of PET scanners. These factors are detector geometry and parallax error. The last section is dedicated to time of flight (TOF) PET approach.

2.1 $^{18}F-FDG$ radio-tracer in oncology applications

PET examinations rely on radio-tracer injection in the patient body that follows the metabolic path of glucose. The reason why glucose behavior plays an important role in tumor lesion diagnosis is the Warburg effect which consists in an aerobic glycolysis in cancer tissues. This means that, in an oxygen rich environment, the energy production in unhealthy cancer cells is dominated by an high rate glycolysis which produces fermentation of lactic acid. The efficiency of this mechanism is lower compared to the energy production in healthy cells originated a higher need of glucose. This link between higher glucose consumption and ill cells represents the basis of PET. In other words, identifying regions with a higher concentration of radio-tracer allows detecting anomalies in glucose consumption which acts as indicator of tumor lesions.
An example of radio-tracer is a biomolecule of glucose where a OH^- group is replaced by a positron emitter as presented in Fig. 2.1. One of the most common positron emitter is fluorine ^{18}F that, when inserted in the glucose structure, combines into fludeoxyglucose $^{18}F-FDG$.
This positron emitter is produced in dedicated cyclotrons or linear accelerators where oxygens molecules (^{18}O) are irradiated by protons creating ^{18}F unstable state. The half-life of ^{18}F is 109 minutes: this is sufficient for the production and transportation of the radio-tracers in hospitals. When the $^{18}F-FDG$ is injected in the patient body, it follows the glucose metabolic path

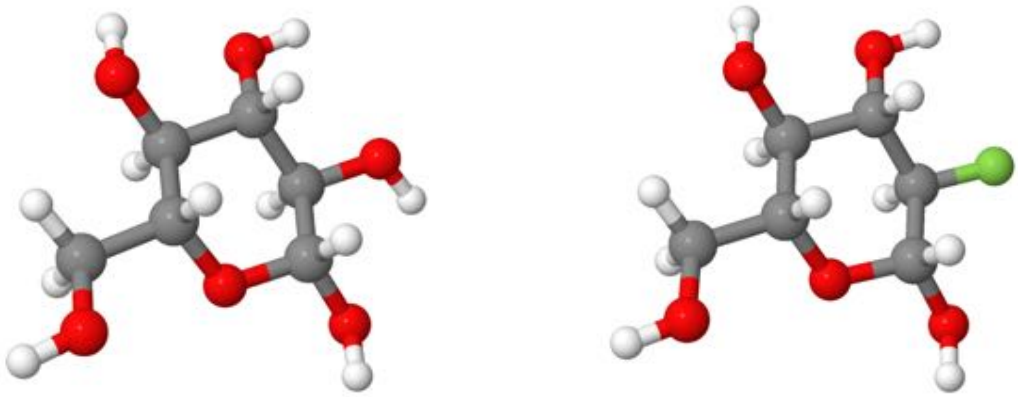

FIGURE 2.1. Molecular structure of the glucose and the $^{18}F-FDG$. In grey the molecules of Carbon, in red the Oxygen ones, in white the Hydrogen and in green the molecule of ^{18}F (picture from Wikipedia).

concentrating in regions where glucose is absorbed. The unstable fluorine naturally decays in the stable state ^{18}O through a β^+ decay that can be described as follow.

$$p \rightarrow n + e^+ + \nu \tag{2.1}$$

where a proton p of fluorine decays in a neutron n, a neutrino ν and a positron e^+. The latter loses its kinetic energy traveling through the human body until it annihilates with a nearby electron. This annihilation produces two back-to-back gamma rays each with an energy of 511 keV that corresponds to the electron or positron mass as described in Eq. 2.2.

$$e^- + e^+ \rightarrow 2\gamma\,(511\ keV) \tag{2.2}$$

Before the annihilation, the electron-positron system transits through an exotic atom called positronium (Ps) that is a highly unstable state. It is characterized by the two particles which rotate around their center of mass electromagnetically bound as presented in Fig. 2.2.
Positronium has a singlet and a triplet state at lower energy level. The singlet state, known as parapositronium (p-Ps), is characterized by an antiparallel spin $^1S_0$ configuration and it decays in an even number of gamma rays. The $p-Ps$ standard decay involves two gamma rays while the probability of having four gamma rays is 1.439×10^{-6} lower. The most probable two gamma ray emission from this singlet state is the one exploited in PET applications. If the electron-positron system is not at rest the two gamma rays are not emitted exactly back-to-back but with an emission angle variance in the order of 0.3° due to momentum conservation law. The deviation from back-to-back configuration has to be properly treated in PET scanner in order

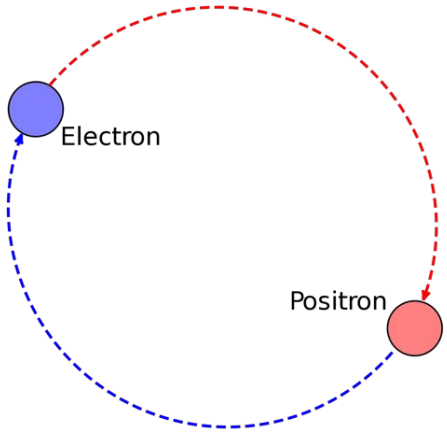

FIGURE 2.2. A scheme of the positronium state (picture from Wikipedia).

to avoid performances degradation of the entire system. This affects particularly whole body PET system while it is negligible for small devices. The second positronium configuration is the ortopositronium (o-Ps) which is a triplet state with a parallel spin configuration $^3S_1$. The typical decay consists in three gamma rays emission. Emission of more than three gamma rays is possible but it is a highly suppressed decay channel. Compared to parapositronium, the decay products collinearity is lost in ortopositronium due to the fact that the final system represents a classic three-body problem. This decay channel is useless in PET application.

2.2 Light detection: scintillating materials

The element that plays a fundamental role in PET is the detection system. The mechanism behind gamma ray spectroscopy is to convert the energy information of incoming radiation into visible light. There are materials, called scintillators, that are able to perform this energy conversion through a scintillation mechanism. In fact, crossing a scintillating material, radiation loses its energy by ionization which is converted into optical light.
Scintillating materials can be divided in two families, organic and inorganic scintillators and they differ by the process in which energy is converted. In PET applications the widely used materials are the inorganic scintillators and therefore this section is dedicated to a detailed description of scintillation mechanism in these materials.
As presented in the work of G. F. Knoll entitled "Radiation detection and measurement" [3], energy conversion into optical light finds its origin in the crystal lattice band structure. In details, the material energy states allow electrons to occupy only discrete bands as presented in Fig. 2.3. The ground state is represented by the valence band where electrons are bound to the material atomic structure while the excited state is represented by the conduction band.

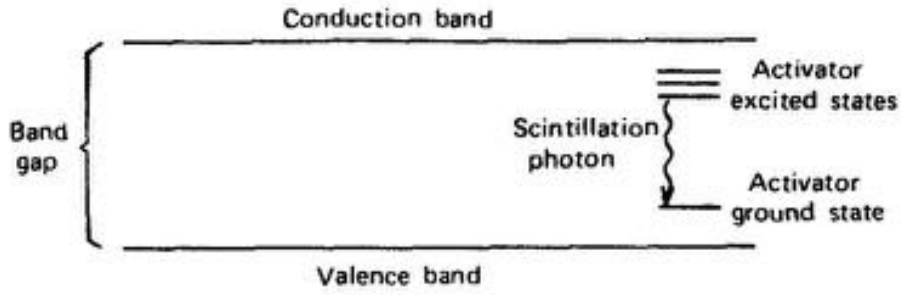

FIGURE 2.3. Band structure of inorganic scintillators with activator sites. (picture from "Radiation detection and measurement", G. F. Knoll)

In between the two energy states there is the forbidden band or band gap in which electrons presence is prohibited. The energy amplitude of the gap is a materials intrinsic feature. When radiation crosses a scintillator it interacts with the atomic lattice. Its energy is transferred to valence band electrons that jump into conduction band if their energy exceeds the forbidden gap amplitude. These electrons are free to migrate in the material lattice. When an electron reaches the conduction band, it leaves a positively charged hole in the valence band originating an unstable state. In nature, all systems tend to reach the minimum energy configuration and therefore excited electrons in conduction band return to ground state losing energy by emitting light. The emitted light wavelength is determined by the energy amplitude of the forbidden gap. Usually, in pure crystals, this mechanism is inefficient or it is characterized by amplitude values which return non-visible light emission. To improve the efficiency or force visible range emission, activators center are added in the structure of scintillators in order to create an intermediate energy state inside the band gap. These defects in the material lattice, knows as luminescence centers, work as a wavelength shifter enabling visible light emission and avoiding reabsorption processes. The reason is a lower amplitude energy gap which characterizes the activators centers. The energy needed to relocate an electron from valence to conduction band is, in fact, higher than the light energy emitted by the luminescence center avoiding overlaps between absorption and emission spectra as presented in Fig. 2.4 for the specific case of LYSO scintillator.
To summarize, when a radiation passes through a scintillating material, its energy excites valence band electrons creating electron-hole pairs. The holes rapidly drift to activation centers while electrons take more time moving in the conduction band. When they reach an activator center, the recombination takes place emitting visible light. The lattice structure of the scintillating material determines the time needed by electrons to recombine with holes and defines the decay time of scintillation processes.
Gamma rays can transfer energy to electrons in scintillators through three processes. The first

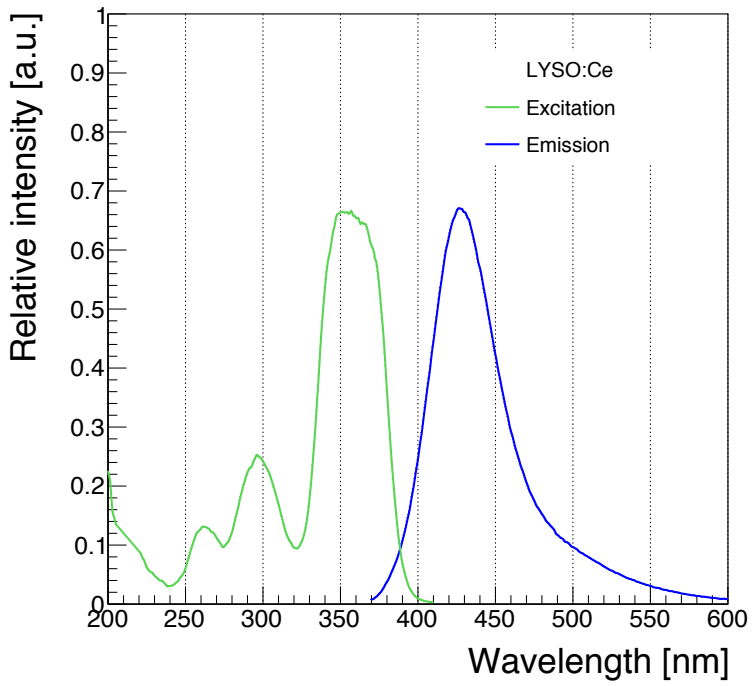

FIGURE 2.4. Absorption and emission spectra of LYSO.

one, known as photoelectric effect, occurs where gamma rays are completely absorbed by material atoms which emit a photoelectron. The process can be described by Eq. 2.3.

$$E_{e^-} = E_\gamma - E_b \tag{2.3}$$

E_b is the electron binding energy in the atomic shell and E_γ is the energy of the incoming gamma ray. The emitted electron transfers its energy to electrons in valence band exciting them to conduction band. Additional X-rays are produced in this reaction as results of de-excitation of the ionized atom by absorption of a free electron. Photoelectric effect is the predominant mechanism of interaction between gamma rays and matter and its probability τ can be described as follow.

$$\tau \cong constant \times \frac{Z^n}{E_\gamma^{3.5}} \tag{2.4}$$

where n is in between four and five and Z is the atomic number.
The second interaction mechanism is the Compton scattering in which part of the incoming radiation energy is transferred to a material electron by scattering. The overall effect is a variation of gamma ray direction and the presence of a recoiling electron which transports the

energy lost by incident radiation. It can be described by Eq. 2.5.

$$E'_\gamma = \frac{E_\gamma}{1 + \frac{E_\gamma}{m_0 c^2} \times (1 - cos\ \theta)} \tag{2.5}$$

where $m_0 c^2$ is the 511 keV electron mass, θ is the deviation of the gamma ray trajectory, E_γ and E'_γ are respectively the gamma ray initial and final energy. The Compton scattering interaction probability σ can be approximated by Eq. 2.6.

$$\sigma \sim \frac{\rho\, Z}{E_\gamma} \tag{2.6}$$

where ρ is the electron density.
The last interaction mechanism between gamma rays and matter is the production of an electron and a positron. It is a threshold process in which the initial energy has to be higher than 1022 keV. This value represents the energy needed to generate an electron-positron pair at rest corresponding to the sum of their masses. According to the fact that gamma rays energy is 511 keV, this process does not take place in PET applications.
The deposited energy spectrum for a 511 keV consists in a continuous originated by Compton scattering and a photopeak in which the entire energy is transferred to the scintillator. Ideally, it can be represented by Fig. 2.5 (left part).

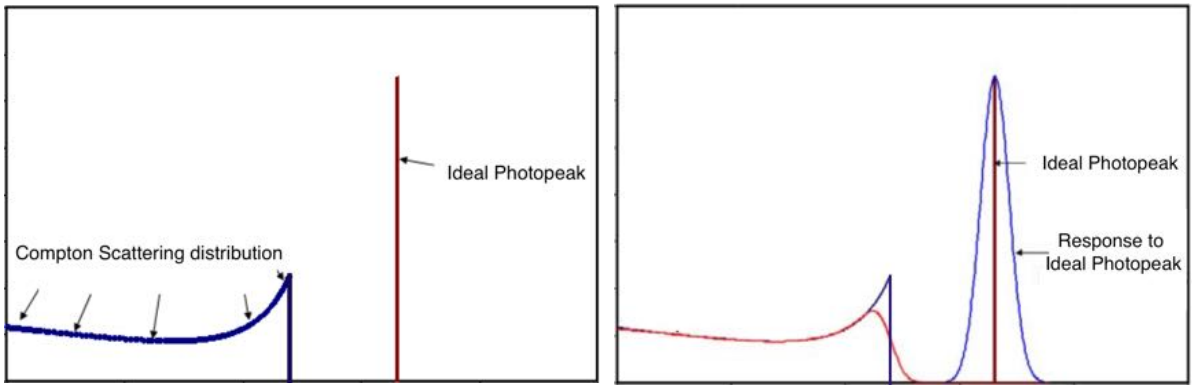

FIGURE 2.5. Typical deposited energy spectrum in scintillators (picture from "The Compton Effect - Compton Scattering and Gamma Ray Spectroscopy",J. E. Parks).

Photoemission statistic, scintillators defects and absorption processes affect the theoretical spectrum which appears, in reality, more blurred (right part of Fig. 2.5). The parameter which acts as indicator of this blurring is the energy resolution defined as:

$$E_{res} = \frac{Photopeak\ FWHM}{Photopeak\ Position} \tag{2.7}$$

The energy resolution depends on the scintillating material. In a complete PET system also photodetectors and readout chain play a role in the energy resolution of the detected spectrum.

2.2.1 Scintillators for PET application

Scintillators are widely used in high energy physics, homeland security and medical application but requirements are different from field to field. The intrinsic properties of these materials rule the interaction and scintillating mechanism and they are summarized in Table 2.1. PET devices require small scintillators dimension in order to guarantee a high accuracy in determination of interaction position.Furthermore, scintillators must be able to stop and detect the higher number of gamma rays to ensure high detection sensitivity. Increasing the sensitivity has the effect of shortening PET examination time. This means a reduction of stress and possible patient movements which can degrade the quality of reconstructed images. As presented in the previous section, to maximize the gamma ray interaction probability, high density and high effective atomic number are fundamental requirements for PET.

	NaI(Tl)	BGO	GSO:Ce	LSO:Ce	LYSO:Ce	$LaBr_3$	BaF_2
Density (gm/cm^3)	3.67	7.13	6.7	7.4	7.1	5.3	4.89
Effective atomic number (Z)	51	74	59	66	64	47	54
Linear attenuation coefficient (cm^{-1})	0.34	0.92	0.62	0.87	0.86	0.47	0.44
Light yield (% NaI(Ti))	100	15	30	75	75	160	5
Decay time (ns)	230	300	60−65	40	41	16	0.8
Hygroscopic	yes	no	no	no	no	yes	slightly
Photoelettric effect (%)	17	40	25	32	33	13	12
Refractive index	1.85	2.15	1.85	1.82	1.81	1.88	1.56
Emission maximum (nm)	410	480	440	420	420	370	220

TABLE 2.1. The main properties of different scintillators. (Magdy M. Khalil, "Basic science of PET images")

Light yield is the number of optical photons generated per MeV during scintillation events. Due to the fact that the gamma ray energy is 511 keV, the number of photons generated in

the scintillation events has to be high in order to provide good energy resolution. In fact, more optical photons are generated, better will be the energy resolution, being able to better separate Compton scattering and photopeak events. Optical photons need to cross the crystal-detector interface to be collected. According to Snell's law, to avoid internal reflection, the scintillator index of refraction needs to approximately match the detector surface one. Furthermore the emitted light wavelength needs to be in the range of maximum detection efficiency of the photodetector in order to maximize the light collection. In addition, a fast scintillator response is mandatory to achieve high timing performances and to reduce the collection of false coincidences events as explained later in this chapter.

2.2.2 LYSO

For the requirements presented above, the scintillator that is more suitable for PET application is the LYSO:Ce. Lutetium yttrium orthosilicate ($Lu_1.8Y_2SiO_5$:Ce) belongs to rare earth orthosilicates ($RE(SiO_4)O$) and it requires cerium codoping in order to activate its scintillation properties. Cerium replaces part of lutetium atoms creating Ce^{3+} ion. This ion has an electron in the 4f shell that can be excited into the 5d level. Scintillation processes take place from radiative transition from lowest 5d energy level to two 4f ground levels as explained in the work of H. Suzuki in 1993 ([5]) and in the work of J. D. Naud in 1996 ([6]).

2.3 Photodetectors

In scintillating crystals, the gamma ray information is carried by optical photons generated after its interaction with the medium. These photons need to be converted into voltage pulse in order to be recorded and re-elaborated by the acquisition system. The component dedicated to this task is the photodetector. The principle is that optical light interaction with photodetectors generates free electrons which are multiplied generating an electric current. When collected, it arises a voltage pulse. Photodetectors can be divided into categories according to the relation between charge collected and incoming radiation energy. If there is a proportionality between these variables, the detector is able to perform spectroscopy working in the so called proportional region. If the collected charge collected is always the same and does not have an energy dependency, the photodetector works in the so called Geiger mode. In this working region the multiplication stage saturates the signal for each detected event making impossible to perform energy measurement. The only information that can be recovered is the presence of an interacting radiation. In order to better understand working principle and differences between these two different detection modalities, it is worth to describe an example for each category: the photomultiplier tube (PMT) for the proportional detection and the multi-pixel photon counter (MPPC) that is based on Geiger

mode. A more detailed description of the latter is provided according to the fact that it is the detector used in this research study.

2.3.1 Photomultiplier tube

PMT is probably one of the most used detectors in spectroscopy due to its ability to convert even low amounts of light into electrical pulses thanks to a high multiplication factor. Furthermore, PMT linearity ensures precise energy measurements of incident light. The PMT is essentially a vacuum tube in which optical light conversion is performed by a photocathode. It represents the detector active area as presented in Fig. 2.6 and it absorbs and converts the incident optical photons energy into electrons. These are accelerated to the first dynode by a voltage difference. The dynode is made by a material which emits secondary electrons after being hit by primary ones performing a multiplication stage. A numerical example that helps in the understanding of this process is presented by G. F. Knoll in "Radiation detection and measurement" [3]. Usually, electrons originated in the photocathode are emitted with a kinetic energy of 1-2 eV. This means that, if the first dynode is positively charged with 100 V and an energy of 2-3 eV is needed to create secondary electrons, one incident electron can generate 30 secondary electrons. This number is in reality reduced due to geometrical inefficiencies and to the production of low energy secondary electrons which are not able to escape from the dynode.

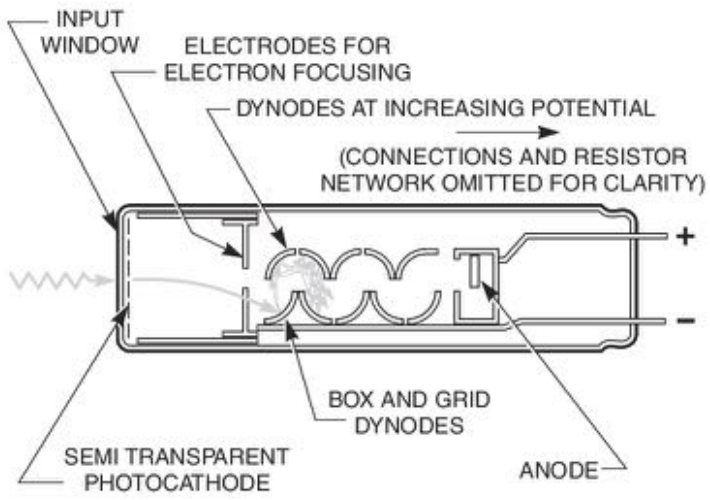

FIGURE 2.6. Structure of a PMT (picture from Newport.com).

This multiplication stage is repeated by means of several dynodes with increasing voltage difference and, in general, each dynode multiplication factor can be expressed as follow.

$$\delta = \frac{number\ of\ secondary\ electrons}{incident\ electron} \tag{2.8}$$

The PMT is able to multiply the initial current by a factor 10^8 making possible single photon detection. One disadvantage of this technology is magnetic fields sensibility. The path that electrons follow from their production point in the photocathode until the anode can be modified by magnetic force according to Lorentz law. This effect limits these photodetectors application in high energy physics experiment as CMS and ATLAS at CERN where high magnetic fields are applied. Also in medical applications, if PET examination needs to be combined with other medical techniques based on magnetic fields, as for examples the magnetic resonance (MRI), the choice of PMTs is discouraged.

2.3.2 Multi pixel photon counter

MPPC is a silicon-based avalanche photodiode that works in Geiger regime ([7], [8]). The interest around this device increased a lot in the last years due to its possible application in several fields such as high energy physics, astronomy but also medical application. The main reason is that it is considered a good substitute of conventional photomultipliers thanks to magnetic fields insensitivity, robustness and uniformity of response. To understand the properties of this detector, its functioning has to be described in details starting from silicon response to radiation. Silicon belongs to semiconductor elements. The silicon energy gap is 1.17 eV at 0° K and 1.11 at 300° K (Data from Kittel, C., Introduction to Solid State Physics. [4]) and, if a photon that travels through this material releases enough energy, one or more valence band electrons jump into the conduction band creating electron-hole pairs. The silicon is a good candidate as a photodetector material thanks to an efficient absorption among a vast range of incoming radiation wavelength. Furthermore, tens of micron in depth of silicon are enough to convert the energy of optical photons. The detection mechanism can be described as follow:

- A silicon p-n junction creates a depletion region in the material that it is free of charge carriers originating a so called photodiode.
- An inverted bias is applied establishing an electric field in that area.
- The incoming radiation releases energy into the silicon creating electron-hole pairs.
- The electric field makes the charges accelerate to the anode (holes) and the cathode (electrons).

What it is worth noting is that, during the acceleration, electrons and holes have enough energy to generate secondary particles via impact ionization. This cascade of charges develops across the silicon region where the electric field is applied making the silicon itself breaks down and be conductive. To quench the current flow during the breakdown, resistors are placed in series with the photodiode. The overall effect is a macroscopic current flow that takes place in Geiger regime. A p-n junction which operates in this regime is called single photon avalanche diode (SPAD).

The main advantage of this technology is a high gain (order of 10^6) but there is a drawback due to the SPAD detection mechanism. The silicon breakdown removes the correlation between initial energy of the incident photon and final current generated during the amplification process. Therefore SPADs can be considered as photon-triggered switches which give a binary output, as on and off state. Due to this lack of proportionality, it is not possible to use individual SPAD for spectroscopy measurements. This problem can be solved by using an array of independent SPADs, called SiPM. The advantage of using this design is that the avalanche which develops during the amplification stage, does not propagate across all the components but it is confined to the single SPAD. This feature raises the possibility of performing energy measurements by counting the number of SPAD activated by radiation. In more specific words, the photocurrents which are originated by the amplification avalanche in each SPAD, are summed up together to transform the individual binary signals in a quasi-analog output proportional to the photon flux magnitude.
It is worth to underline the main features of SiPMs as a photodetector starting from the output pulse of a SiPM presented in Fig.2.7.

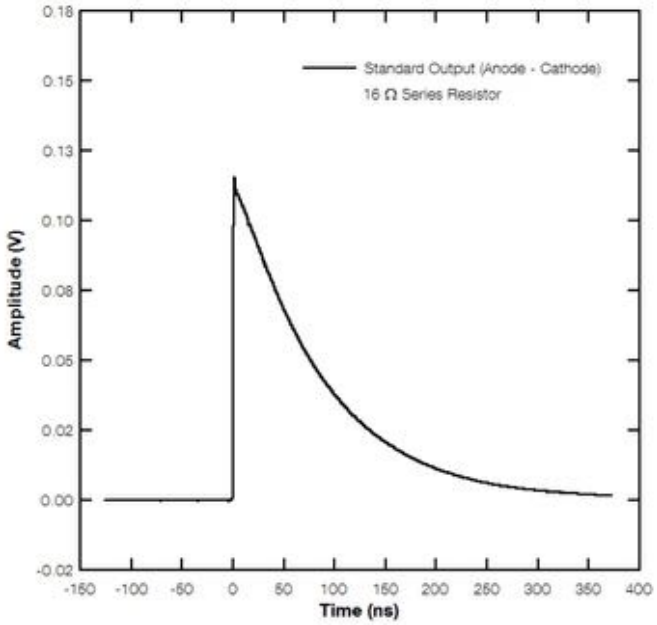

FIGURE 2.7. A typical SiPM pulse shape. (picture from "An Introduction to the Silicon Photomultiplier-Sensl")

The rise time is driven by how the avalanche develops inside each SPAD and by the arrival time jitter of the photocurrents which originate in different detectors regions. The decay time instead is determined by the recharge time constant of microcells and it can be evaluated as follow:

$$\tau_{RC} = C_d \times (R_q + R_s \times N) \tag{2.9}$$

where C_d is the capacitance of the SPAD, R_q is the quench resistor and R_s are all the possible resistances in series with the N cells.
As described before, the main advantage of this device is the high gain. It can be defined as the number of the secondary charges generated by each incident photon. Translating this definition into an equation, the result is:

$$G = \frac{C \times \Delta V}{q} \tag{2.10}$$

where the numerator represents the microcells charges (capacitance multiplied by voltage) and the denominator is the charge unit. After defining the gain, it is possible to write an equation which sums up the general functioning of the SiPM.

$$Q = N_{fired} \times G \times q \tag{2.11}$$

The overall photocurrent generated in the SiPM, Q, is the results of pixels fired number N_{fired} and gain G, multiplied by the electron charge. This equation underlines the importance of pixels number (SPAD) which are switched on by photons detection. Considering this equation and the binary output of the single SPAD, microcells density and dimensions play a key role in term of detector performances. It leads to the definition of the fill factor which is the percentage of detector area that is radiation sensitive. Technically speaking, it is not possible to cover the entire SiPM area with SPADs due to the fact each cell needs to be isolated and independent from the others. Furthermore, there are electrical and readout components that need to be arranged close to the microcells originating a radiation insensitive region. The last parameter that needs to be described is the photon detection efficiency (PDE). The PDE is the measurement of detector sensitivity as function of wavelength, fill factor and applied voltage. This notion is the probability of an incoming photon to detected by the SiPM. It can be represented as follow:

$$PDE(\lambda, V) = \eta(\lambda) \times \epsilon(V) \times F \tag{2.12}$$

where $\eta(\lambda)$ is the silicon quantum efficiency, $\epsilon(V)$ is the probability to generate an avalanche and F is the fill factor.

2.4 Coincidence PET acquisition chain

As described by A. Del Guerra in "Positron Emission Tomography: Its 65 years" [9], PET acquisition chain is based on a coincidence circuit and on a digital energy converter as presented in Fig.

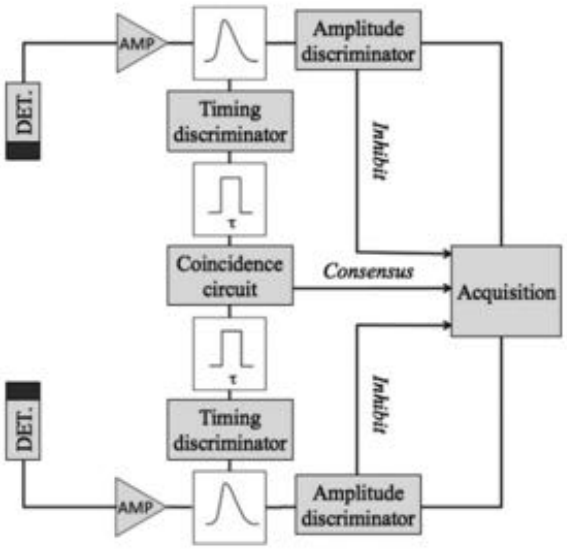

FIGURE 2.8. A typical acquisition chain for PET application (picture from "Positron Emission Tomography: Its 65 years", A. Del Guerra).

2.8.

Two detected events are considered and recorded as a coincidence when the difference between arrival times is less than a fixed value called coincidence time window τ. This time interval depends on the geometry of the scanner and, usually, it is set equal to the time needed to light to cover the maximum detectors distance. In order to recognize a coincidence event, the timing information of detected radiation is re-elaborated by a time discriminator. This produces a digital signal with a width equal to half of the coincidence window $\frac{\tau}{2}$. A dedicated circuit compares the digitalized pulse. The events are recorded as a coincidence pair if there is a timing overlap between them. Also their energy is digitalized and stored.

In PET acquisition there are different categories of events which are able to pass the coincidence selection and they are described by the help of Fig. 2.9.

The first category of events is represented by true coincidences. These are the only events that describe a real LOR along which the positron-electron annihilation takes place. In Fig. 2.9 they are represented by annihilation which takes place in 1. The two gamma rays are detected without interacting before reaching the i and j scintillators. Another possibility is represented by one gamma ray which interacts with human tissues changing its direction by scattering (2). These events are called scatter coincidences. The last events category are random coincidences in which detected gamma rays are not originated from the same annihilation (3 and 4). The small arrival time difference in detectors m and n allows them to be recorded as a coincidence. LORs identified by scatter and random events do not contain information about annihilation position and therefore they are considered sources of noise in PET acquisition. Corrections need to be

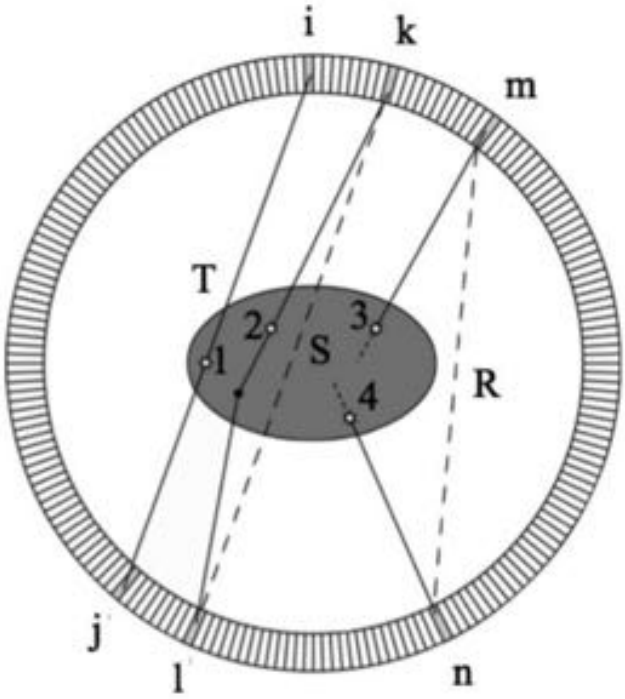

FIGURE 2.9. Possible coincidence events in PET acquisition (picture from "Positron Emission Tomography: Its 65 years", A. Del Guerra).

applied in order to mitigate the effect of these events in the metabolic images reconstruction.

2.5 Factors which influence the spatial resolution in PET devices

The spatial resolution is the resolving power of a PET device. It consists in the minimum distance between two radioactive objects that can be reconstructed separately. Many factors play a role in the spatial resolution determination and the main ones are described in the following sections.

2.5.1 Scintillators geometry

Spatial resolution is linked to LORs identification accuracy. It depends on the interaction position determination of gamma rays in detectors and it improves by reaching better accuracy in scintillation events positioning. A key aspect is the scintillator geometry. There are many approaches to obtain good accuracy and one of them is described in the work of D.Schaart "Sub-200 ps CRT in monolithic scintillator PET detectors using digital SiPM arrays and maximum likelihood interaction time estimation."[11]. This approach is based on a monolithic LYSO scintillator in which scintillation events position is reconstructed by using a dedicated algorithm. This

algorithm is able to correlate collected light distribution and emitted light position inside the scintillators. Stronger is this correlation, higher will be the position identification accuracy. This approach can exploit system high sensitivity due to block scintillator configuration and it does not present geometrical limitation on spatial resolution. On the other hand, the complexity of applying dedicated algorithms is not always negligible and can arise problems in crystals edges where only a light fraction is collected by detectors. An alternative approach is based on the different idea of using pixelated scintillator. Instead of having a monolithic bulk, the scintillator is divided in smaller crystals arranged as a matrix. Interaction position is then obtained by knowing which crystal is hit by radiation. The interaction point identification accuracy is related to the transverse size of scintillators. Compared to monolithic scintillators, algorithms with light distribution encoding are not needed but the sensitivity is reduced due to scintillators fragmentation. Example of pixelated scintillators can be found in the ClearPEM scanner developed by the Crystalclear collaboration (J. A. Neves et al, "The ClearPEM breast imaging scanner" [12]) or in the EndoTOFPET project (Milan Zvolsky et al., "EndoTOFPET-US - A Miniaturised Calorimeter for Endoscopic Time-of-Flight Positron Emission Tomography" [13]).

2.5.2 Parallax error

In PET scanners, long crystals are needed in order to provide good sensitivity by detecting the higher number of gamma rays. At the edges of the scanned area, called field of view (FOV), crystals length leads to accuracy deterioration of LORs identification due to parallax error. LORs identification uncertainty is dominated by the crystal section which faces the gamma ray origin position. In the FOV center, this section corresponds to the crystal transverse dimension which is usually in the order of mm. Moving far from the center, this section starts to be dominated by the axial crystal dimension that instead is in the order of 15-20 mm. The result is a non uniform spatial resolution in the FOV which is characterized by degradation close to edges as presented in Fig. 2.10.
Parallax error is the dominant effect for spatial resolution determination in small PET devices while it is negligible in whole body PET scanners. In order to recover uniformity in LORs determination accuracy, the position along the crystals main axis has to be reached. Knowing the DOI information allows avoiding performances degradation due to parallax error as presented in Fig. 2.11.
DOI information can be achieved by means of different techniques. C.S. Levin in "Design of a High-Resolution and High-Sensitivity Scintillation Crystal Array for PET With Nearly Complete Light Collection" [14] proposes a multilayer structure along the axial direction. Each layer is read independently by photodetectors providing the DOI information. J. S. Karp and M. E. Daube-Witherspoon in "Depth-of-interaction determination in NaI(TL) and BGO scintillation crystals using a temperature gradient" [15] develop a PET module based of two different scintillators in the axial direction. Scintillators have different timing profiles and, thanks to a pulse shape

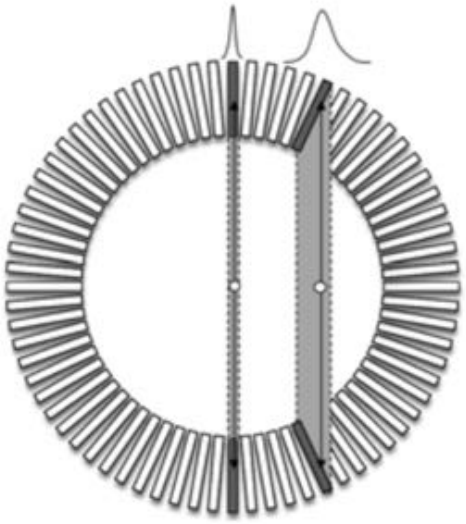

FIGURE 2.10. LORs accuracy degradation due to parallax error (picture from "Positron emission tomography (PET) detectors with depth-of- interaction (DOI) capability", M. Ito et al.).

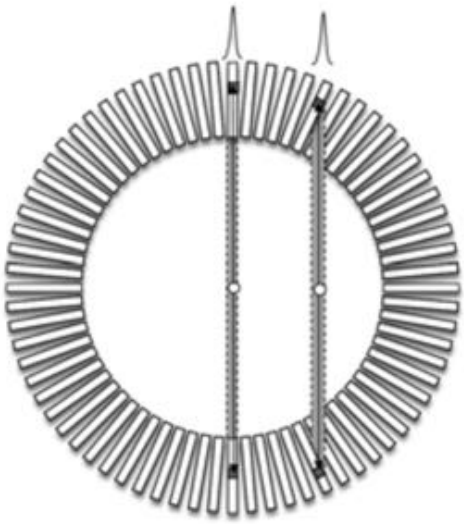

FIGURE 2.11. Effect of DOI information on spatial resolution uniformity (picture from "Positron emission tomography (PET) detectors with depth-of- interaction (DOI) capability", M. Ito et al.).

discriminator, it is possible to identify in which one the gamma ray interaction occurs. Another method is based on double side readout configuration in which scintillators are read on both sides by photodetectors. If a light attenuation behavior is induced along the crystal main axis

the collected light asymmetry provides the DOI information. This approach was chosen in the ClearPEM scanner developed by the CrystalClear Collaboration. This device is a breast dedicated PET scanner based on two heads which rotate simultaneously composed by 96 modules each. ClearPEM module consists of a 8x4 matrix of LYSO scintillators. Each crystal has $BaSO_4$ coating to avoid optical light crosstalk and it is read by a Hamamatsu APD on both sides. DOI information and collected light asymmetry are related by the following equation.

$$C_{DOI} = \frac{Crystal\ length}{Asymmetry\ edge\ one\ -\ Asymmetry\ edge\ two} \tag{2.13}$$

where at denominator there is the collected light asymmetry at the two photodetectors. As final result, ClearPEM DOI performances consist in 5.9 %/mm variation as presented by R. Bugalho et al. in "Experimental characterization of the Clear-PEM scanner spectrometric performance" [16].

2.6 TOF-PET approach

In PET application, the LOR is the only information which is extracted from detectors without any knowledge about the annihilation position along it as presented by M. Pizzichemi in "Positron Emission Tomography: state of the art and future developments" [10]. The emission probability of the two back-to-back gamma rays is constant along the LOR. If the detection time difference of gamma rays in the detectors is registered, ideally the annihilation position can be evaluated as follow:

$$\Delta x = \frac{c \times \Delta T}{2} \tag{2.14}$$

where Δx is the displacement from the LOR center O, ΔT is the detection time difference of two gamma rays and c is the speed of light. Due to detectors finite precision, the uncertainty on timing measurements σ_T propagates to the annihilation point determination as described in the Eq. 2.15.

$$\sigma_x = \frac{c \times \sigma_T}{2} \tag{2.15}$$

TOF-PET technique relies on the introduction of detection time information to calculate the emission probability distribution along LORs. This becomes a gaussian function centered in $O + \Delta x$ with a sigma of σ_x.
Commercial PET scanners provide a FWHM time resolution in the order of 1-2 ns resulting in annihilation position uncertainty equal to 15-30 cm FWHM. Prototypes can achieve 250 ps timing resolution that drops the σ_x value to 3.75 cm FWHM. The ultimate time resolution is 10 ps with which the positron range limit of 1.5 mm is reached. Current values are quite far from this target but there is an effort in the scientific community to push the state of the art limits in order to reach this result.

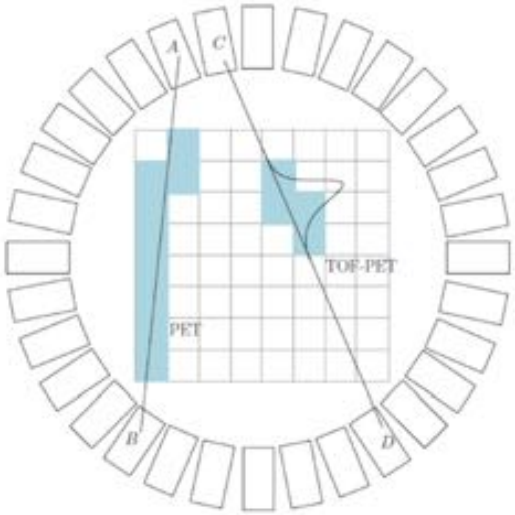

FIGURE 2.12. The TOF-PET principle (figure from S. Surti, J.S. Karp - Physica Medica 32 (2016) 12-22).

TOF-PET approach plays a key role in term of signal to noise ratio (SNR). This can be determined as function of the timing resolution.

$$SNR_{TOF} = \sqrt{\frac{D}{c \times \sigma_T}} \times SNR_{non-TOF} \tag{2.16}$$

where D is the FOV diameter. In the table below, some results of the gain in the SNR by applying the TOF method are reported for small PET scanners and for whole body PET systems (fixed to one for the less than one values).

Timing resolution	30 cm FOV diameter	80 cm FOV diameter
3 ns	1.0	1.0
2 ns	1.0	1.15
1 ns	1.0	1.6
500 ps	1.4	2.3
100 ps	3.2	5.2
10 ps	10.0	16.3

TABLE 2.2. SNR gain of TOF approach.

From Tab. 2.2, reaching a time resolution in the order of hundreds of picoseconds will have an impact on reconstructed image quality. The SNR improves by a factor 3.2 (small animal and organ dedicated PET scanners) and a factor 5.2 (whole body PET devices). The targeted value of 10 ps could represent a milestone for PET application reaching a gain of 10 and 16.3 respectively in reconstructed images contrast.

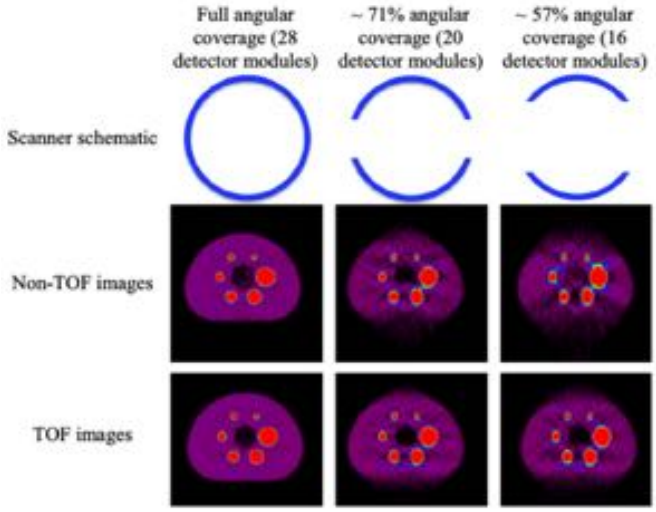

FIGURE 2.13. The comparison between TOF and non-TOF reconstructed images in PET scanners with different detectors coverage (figure from S. Surti, J.S. Karp, "Design considerations for a limited-angle, dedicated breast, TOF PET scanner".

Another TOF-PET benefit is related to the scanner geometry. The annihilation position information is more precise and therefore the scanner angular coverage can be reduced resulting in a lower number of detectors needed to recover metabolic images. An interesting study of S. Surti and J.S. Karp (S. Surti and J.S. Karp in the work "Design considerations for a limited-angle, dedicated breast, TOF PET scanner" [17].) demonstrates this concept and the results are shown in Fig. 2.13. According to these benefits, it is clear why the scientific community is focusing on the achievement of 10 ps timing resolution. This process is not trivial and it is worth to describe the effects which play a role for in the timing resolution improvement. The detection time of incoming gamma rays can be described as follow.

$$t_{det} = T + t_{scint} + t_{trans} + t_{SPTR} + t_{TDC} \tag{2.17}$$

T is the time that gamma rays spend in the crystal before the scintillation takes place. t_{scint} is the time needed to convert the gamma rays into optical photons. t_{trans} is the transit time needed by optical photons to reach the detectors and t_{SPTR} is the detector single photon time spread. t_{TDC} is the time required by the TDC to convert the time information into a digital signal. In order to reach 10 ps timing resolution, all these components need to be improved not only individually but optimizing them all together.

2.7 Commercially available and preclinical PET systems

In this section, an overview of the commercially available PET systems is provided with particular focus on the performances like spatial and timing resolution. The main features of whole-body PET scanners manufactured by Philips, GE and Siemens are listed in the following table.

PET Model	Ingenuity TF (Philips)	Discovery 710 (GE)	Biograph mCT Flow (Siemens)	Discovery IQ (5 Rings) (GE)	Vereos (Philips)
Patient port (cm)	70 Open view	70	78	70	70
Patient scan range (cm)	190	200	195	200	190
Crystal size (mm^3)	4x 4x22	4.2x6.3x25	4x4x20	6.3x6.3x30	4x4x22
Number of crystals	28336	13824	32448	19200	23040
Number of PMTs	420	256	768	720	SiPM
Detector material	LYSO	LYSO	LSO	BGO	LYSO
Transaxial resolution @ 1 cm (mm)	4.7	4.9	4.4	4.9	4.0
Transaxial resolution @ 10 cm (mm)	5.2	5.5	4.9	5.5	4.5
Axial resolution @ 1 cm (mm)	4.7	5.6	4.5	5.1	4.0
Axial resolution @ 10 cm (mm)	5.2	6.3	5.9	5.5	4.5
Time-of-flight resolution (picoseconds)	550	544	540	n.a.	345
Time-of-flight localization (cm)	8.9	8.2	8.1	n.a.	5.2
Concidence window (nanoseconds)	4.5	4.9	4.1	9.5	1.5

TABLE 2.3. Specification of commercially available PET scanners (from P. J. Slomka, T. Pan and G. Germano. "Recent Advances and Future Progress in PET Instrumentation."

The spatial resolution is in te order of 4-6 mm and the timing resolution, if available, is in the range of 345-550 ps resulting in a localization of 5.3-8.9 cm. Four scanners exploit the LYSO-LSO crystal as detector material while the scintillators are made by BGO for the Discovery IQ (5 Rings) manufactured by GE.
Regarding the timing resolution, in 2017 Siemens developed a new PET device, the Biograph Vision, based on LSO crystal able to reach a resolution of 249 ps defining the benchmark of the

field. This scanner is able to recover the smallest sphere (5 mm) in a torso-phantom with a spatial resolution of 3.8 mm FWHM (axial) and 3.9 mmFHWM (transaxial).
Preclinical PET systems are usually characterized by a smaller FOV and the main features of different scanner are shown and listed in the table 2.4.For these preclinical PET devices, the spatial resolution drops in the order of 1.6-2.4 mm.

Manufacturer	Model	Detector design	Scintillator	Ring diameter (mm)	Crystal size (mm^3)	Transaxial resolution FWHM (mm) at 5 mm
Concorde Microsystems, Siemens	microPET P4	Block, 8x8 array with PSPMT	LSO	261	2.2 x2.2x10	2.24
Concorde Microsystems, Siemens	microPET R4	Block, 8x8 array with PSPMT	LSO	148	2.2 x2.2x10	2.20
Concorde Microsystems, Siemens	microPET Focus 200	Block, 12x12 array with PSPMT	LSO	258	1.51 x1.51x10	1.74
Concorde Microsystems, Siemens	microPET Focus 120	Block, 12x12 array with PSPMT	LSO	147	1.51 x1.51x10	1.78
Siemens	Inveon	Block, 20x20 array with PSPMT	LSO	161	1.51x1.51x10	1.64
Philips	Mosaic HP	Pixelated Anger logic, 19 mm PMTs	LYSO	197	2x2x10	2.34
Raytest GmbH	ClearPET	Block, 8x8 dual-layer phoswich array with PSPMT	LYSO/LuYAP	135-225	2x2x10	2.02
Sedecal	Argus (formerly GE eXplore Vista)	Block, 13x13 dual-layer phoswich array with PSPMT	LYSO/GSO	118	1.45x1.45 x7 (LYSO); 1.45x1.45x8 (GSO)	1.66

TABLE 2.4. Specification of preclinical PET systems (from A. L. Goertzen et al. "NEMA NU 4-2008 Comparison of Preclinical PET Imaging Systems."

CHAPTER 3

TOMOGRAPHIC IMAGE RECONSTRUCTION

In this chapter, image reconstruction theory is presented by introducing analytic and iterative reconstruction methods. ClearPEM list-mode algorithm is used in this work and therefore is described in this chapter. The modifications needed to include TOF information are explained in the last section.

3.1 Introduction on reconstruction algorithms

The role of PET reconstruction algorithms is to translate the coincidence events information into positron emitter concentration maps in human tissues. The idea behind image reconstruction can be expressed by the following equation as suggested by A. Alessio and P. Kinahan in their work entitled "PET Image Reconstruction" published in 2006 [18].

$$p = H \times f + n \tag{3.1}$$

where p represents the collected information (the LORs), H is the system response, f is the activity distribution and n is the noise that affects PET acquisitions. In Eq. 3.1 the p variable has to be organized before being analyzed by reconstruction software. A well known method to collect LORs is to organize them in sinograms. The activity distribution is projected along LORs with same ϕ orientation as function of the LORs distance s from the FOV center. This procedure is called line integral. Repeating line integration for all orientations arises a collection of projections $p(s,\phi)$, as presented in Fig. 3.1: the sinogram. The reason for this name has to be found in the sinusoidal behavior that a point source draws in the (s,ϕ) space.
In sinograms, projections have to rely on the same plane and the number of collected sinograms depends on scanner geometry and acquisition mode. There are two modalities, 3D and 2D PET

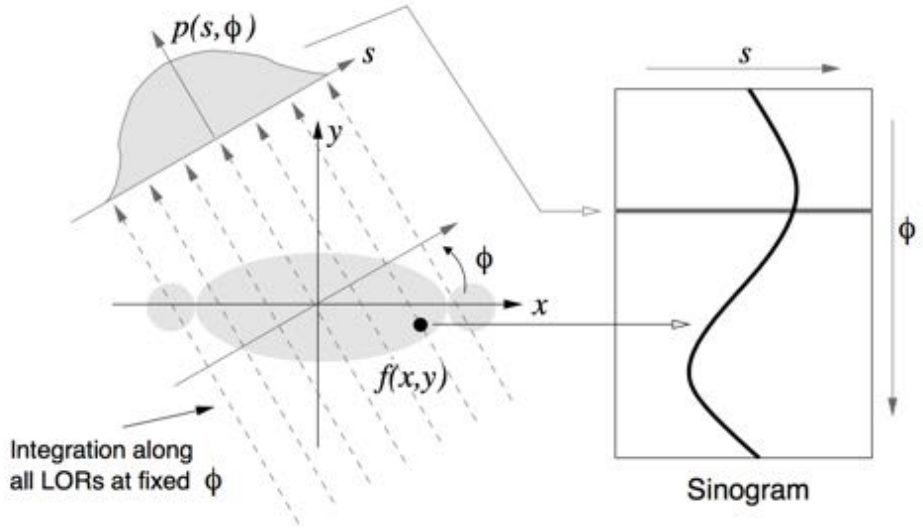

FIGURE 3.1. The line integral along the detected LORs arises a set of projections as a function of the orientation and the distance of the LORs from the center of the FOV that represents the sinogram (picture from A. Alessio and P. Kinahan "PET Image Reconstruction").

acquisition. The latter accepts only coincidences from detectors which belong to the same ring (direct plane) or if detectors rings difference is equal to one (cross plane). For this acquisition mode the total number of sinograms is:

$$N_{sinograms} = 2 \times N_{rings} - 1 \tag{3.2}$$

The patient is scanned in parallel slices along the axial direction. Each slice has a thickness equal to the rings one and 3D image is obtained by joining all slices together. This modality is the easiest one because it is able to maintain the reconstruction complexity low reducing the storage memory needed to register LORs.
3D PET modality allows taking coincidences from detectors in different rings increasing the sinograms number needed to describe the entire system. The advantage of this approach is a sensitivity improvement but reconstruction complexity is increased compared to 2D PET. A comparison between the two different modalities is presented in Fig. 3.2.
Considering Eq. 3.1, reconstruction algorithms allow to recover the activity distribution f starting from the collected information p. Two approaches can be exploited based on the theoretical assumption on deterministic or stochastic data nature. According to the selected hypothesis, reconstruction algorithms can be divided into analytic and iterative respectively for deterministic and stochastic approach.
Considering deterministic data means that no statistical noise affects the data. Therefore knowing

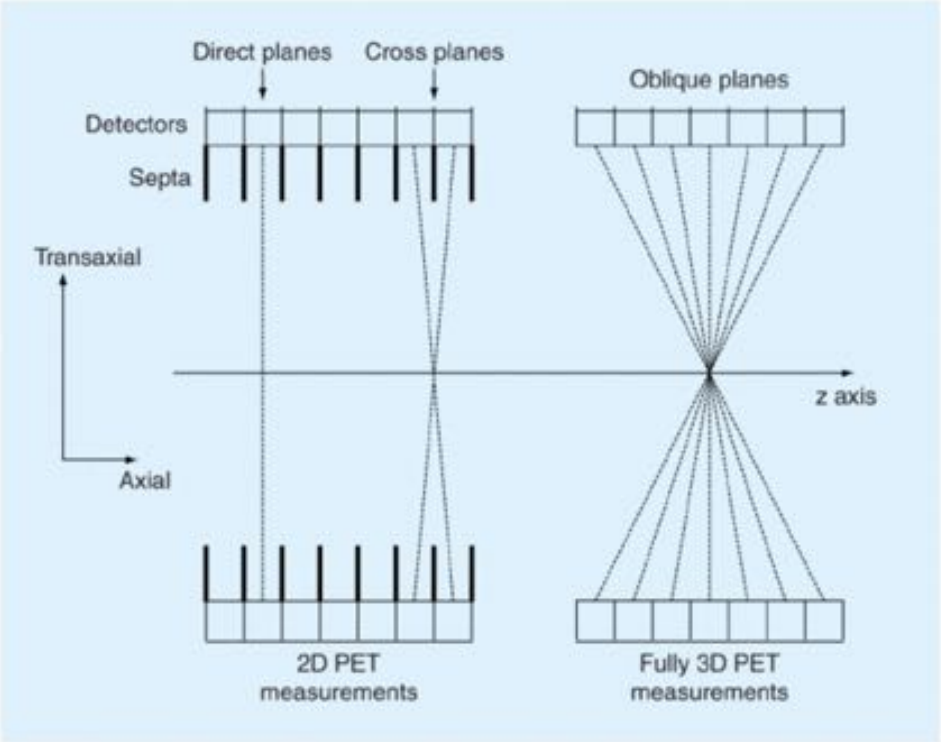

FIGURE 3.2. The difference between the 2D and 3D PET acquisition modalities (picture from A. Alessio and P. Kinahan "PET Image Reconstruction").

n in Eq. 3.1 allows recovering the activity distribution by direct mathematical calculations. This approach is able to quickly perform images reconstruction but considering deterministic noise behavior leads to low resolution images and artifacts. The reason is that PET data follow a stochastic behavior dominated by detection processes, positron annihilation mechanism, random and scatter effects. Introducing a data stochastic model improves the quality of the activity concentration image. On the other hand, it does not allow to address the reconstruction problem by a direct mathematical approach due to complexity. Image reconstruction is performed by iteration methods which converge to an approximated solution of the Eq. 3.1. These reconstruction algorithms have the advantage of achieving better quality but they show high computational costs.

3.2 Analytic reconstruction: the filtered-back projection

As mentioned in the previous section, starting from an activity distribution $f(x,y,)$ it is possible to achieve the projection $p(s,\phi)$ for each orientation thanks to the line integral. This procedure is

known as the Radon's transform presented in 1917 by James Radon and reported below.

$$p(s,\phi) = \int_{-\infty}^{\infty}\int_{-\infty}^{\infty} f(x,y)\cdot\delta(x\ cos\phi + y\ sin\phi - s)\mathrm{d}x\mathrm{d}y \tag{3.3}$$

δ ensures that the integrand is different from zero only on the line that is described by (s,ϕ).
In PET reconstruction, the procedure is to recover the activity distribution $f(x,y,)$ starting from projections $p(s,\phi)$. The Eq. 3.3 is then inverted into what is known as the Randon's antitransform. To recover $f(x,y,)$, the activity concentration needs to be redistributed from projections to $(x,y,)$ space but the activity position information along LORs is lost during the $p(s,\phi)$ construction. To overcome this issue, the simplest approach is to associate a constant value along LORs which corresponds to the $p(s,\phi)$ value as presented in Fig. 3.3. This operation is called backprojection $b(x,y)$ and it can be mathematically described as follow.

$$b(x,y) = \int_0^{\pi} p(s,\phi)|_{s=x\ cos\phi+y\ sin\phi}\ \mathrm{d}\phi \tag{3.4}$$

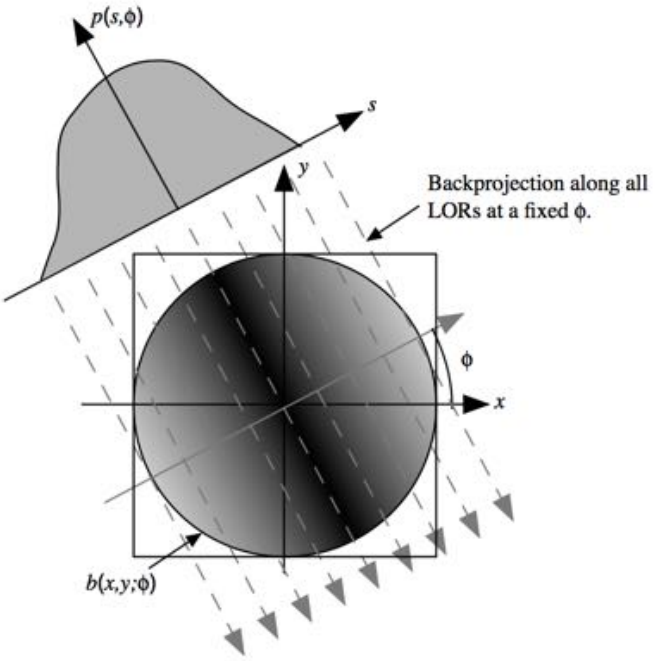

FIGURE 3.3. The backprojection mechanism. The projection $p(s,\phi)$ is redistributed along the LORs at fixed ϕ (picture from A. Alessio and P. Kinahan "PET Image Reconstruction").

Thinking that simple backprojection returns the activity distribution image is a misunderstanding

and the reason behind it has to be found in the connection between Radon's and Fourier's transform described by the Central Slice Theorem (CST). To understand this theorem, it is important to describe the Fourier's transform which is used to rewrite a time dependent function in frequency domain. It can be written by means of polar coordinate as follow.

$$\mathscr{F}\{p(s,\phi)\} = P(w) = \frac{1}{\sqrt{2\pi}} \int_{-\infty}^{\infty} p(s)\, e^{-iws} \mathrm{d}s \tag{3.5}$$

As an example, it is possible to appreciate the Fourier's transform effect on a rectangular pulse function in frequency domain in Fig. 3.5. This is one of the most powerful mathematical tools which finds application in several scientific fields as of differential equations analysis, signal processing, quantum mechanics, magnetic resonance imaging and mass spectroscopy.

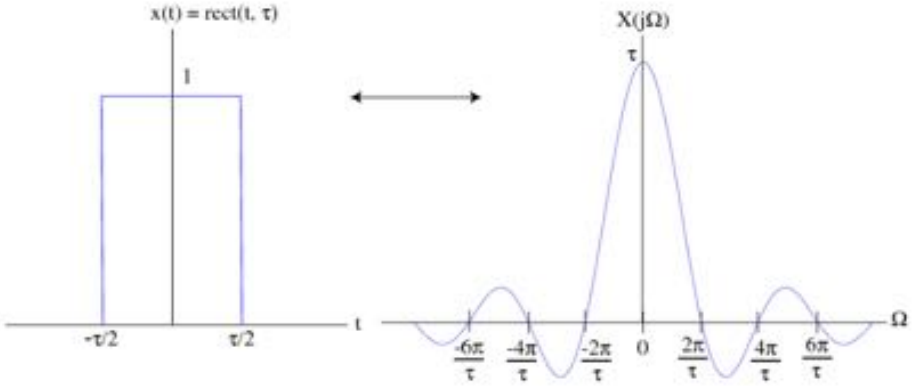

FIGURE 3.4. Scheme of the Fourier's transform applied on a rectangular pulse function.

The central slice theorem states that the following two operations are equivalent:

- Consider a distribution f in the (x,y) space, perform a projection for a fixed angle ϕ and evaluate the 1D Fourier's transform.
- Perform the 2D Fourier's transform as first step and take a slice which crosses the frequency space center with same orientation ϕ.

This theorem connects Randon's to Fourier's transform according to the fact that the 2D Fourier's transform of a two-dimensional function $f(x,y)$ is equal to the 1D Fourier's transform of the Radon's transform at the same angle ϕ.
The backprojection discussed in Eq. 3.4 arises an overestimation of the activity distribution in the FOV center originated by oversampling in the central region of the frequency domain. To overcome this issue, the procedure is to apply a filter in the Fourier space obtaining uniform

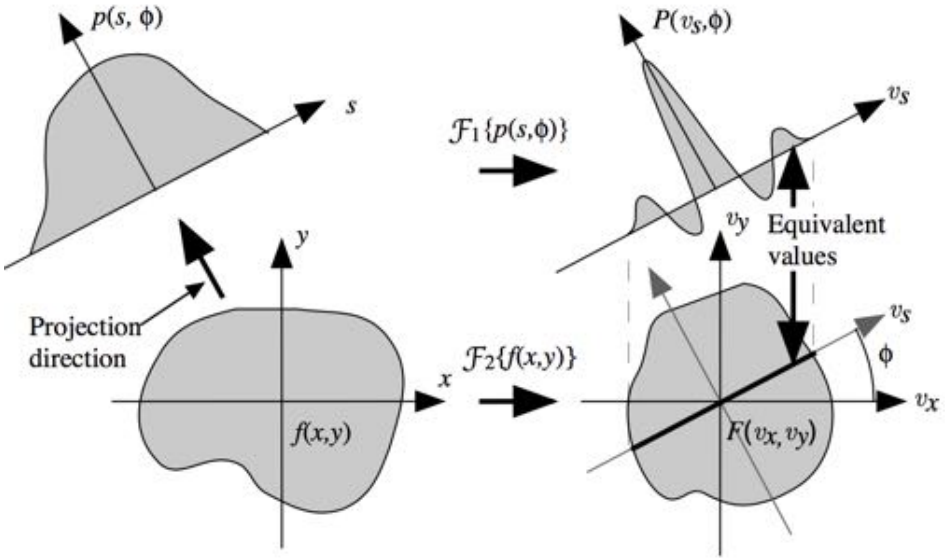

FIGURE 3.5. Schematic representation of the Central Slice Theorem (picture from A. Alessio and P. Kinahan "PET Image Reconstruction").

sampling. The best candidate is a cone filter $v = \sqrt{v_x^2 + v_y^2}$ that amplifies the edge of the Fourier space while reducing the central part. A backprojection with a frequency filter is known as filtered back projection (FBP). v_x and v_y coordinates can be obtained by the polar ones (w, ϕ) as $v_x = w\ cos\phi$ and $v_y = w\ sin\phi$.

Filtered back projection belongs to analytic reconstruction methods in which the solution can be reached by direct mathematical approach starting from the definition of the activity distribution image:

$$f(x,y) = \mathscr{F}_2^{-1}\{F(v_x,v_y)\} = \int_{-\infty}^{\infty} dv_x \int_{-\infty}^{\infty} dv_y\ F(v_x,v_y)\ e^{2\pi i(v_x\ x + v_y\ y)} \tag{3.6}$$

The next step is a polar coordinate translation according to their definition:

$$v_x = w\ cos\phi \quad , \quad v_y = w\ sin\phi \quad , \quad dv_x dv_y = w dw d\phi \tag{3.7}$$

By applying this conversion $f(x,y)$ becomes:

$$f(x,y) = \int_0^{2\pi} d\phi \int_0^{\infty} dw w\ F(w\ cos\phi, w\ sin\phi)\ e^{2\pi i\ w\ (x\ cos\phi + y\ sin\phi)} \tag{3.8}$$

Knowing that $F(w\ cos\phi, w\ sin\phi)$ is equal to $P(w)$ for the central slice theorem and that $x\ cos\phi + y\ sin\phi$ is equal to s, Eq. 3.6 can be rewritten as:

$$f(x,y) = \int_0^{2\pi} d\phi \int_0^{\infty} dw w\ P(w)\ e^{2\pi i\ w\ s} \tag{3.9}$$

Integration limits can be modified because integrating between 0 and 2π does not add any information compared to 0 and π. Furthermore, the absolute value of w is introduced modifying the w integration limits.

$$f(x,y) = \int_0^{\pi} \mathrm{d}\phi \int_{-\infty}^{\infty} \mathrm{d}w \; |w| \; P(w) \; e^{2\pi i \; w \; s} \tag{3.10}$$

In Eq. 3.10 the inverse Fourier's transform of the function $P(w)$ filtered by $|w|$ can be recognized. This is the filtered back projection and, defining it as $p'(s,\phi)$, the result is:

$$f(x,y) = \int_0^{\pi} \mathrm{d}\phi \mathscr{F}^{-1}\{|w| \; P(w)\} = \int_0^{\pi} \mathrm{d}\phi \; p'(s,\phi) \tag{3.11}$$

Integration among all possible orientation of $p'(s,\phi)$ returns the activity distribution image. To summarize filter back projection consists in five steps:

- Fourier's transform of the projection $p(s,\phi)$.
- Application of the filter $|w|$ in the frequency domain.
- Inverse transform of the filtered product.
- Backprojection.
- Sum of each orientation contribution.

In Eq. 3.7 the calculated solution is unstable. If small variations are applied to the initial data, the final result will dramatically change. To solve this instability of the analytic approach, a smoothing can be applied in order to reduce contributions from high frequency noise. Eq. 3.7 can be rewritten as follow.

$$f(x,y) \approx \int_0^{\pi} \mathrm{d}\phi \mathscr{F}^{-1}\{W(w)|w| \; P(w)\} \tag{3.12}$$

Where $W(w)$ is the smoothing function.
Analytic reconstruction methods can be extended to 3D PET. This is not trivial because truncated projections arise by accepting coincidences in between different rings. The result is that the system response to same activity concentration varies along the axial direction. In reconstruction processes, this variation of sensitivity does not allow to apply simple Fourier's transform. A common approach to 3D analytic reconstruction method is the 3D reprojection (3DRP) algorithm in which the unmeasured projections are obtained by forward projecting an image estimation. This estimation is obtain by considering only coincidences that take place between same rings detectors as in 2D PET reconstruction.

3.3 Iterative reconstruction: the maximum likelihood expectation maximization

Iterative methods are based on stochastic data model and realistic noise description. This leads to complexity in the solution evaluation of the reconstruction problem. Due to this complexity, it is not possible to achieve the exact solution of the Eq. 3.1. The reconstruction problem is tackled by multi-step methods in which the activity distribution estimation is improved in each iteration. This approach is known as iterative method. A. Alessio and P. Kinahan in their work entitled "PET Image Reconstruction" were able to summarize the basic concept of these methods underlining five fundamental components.
The first one is to find a way to model the image in such a way that can be analyzed and processed. The most used model is the division of image domain into voxels or pixels for 3D or 2D reconstruction.

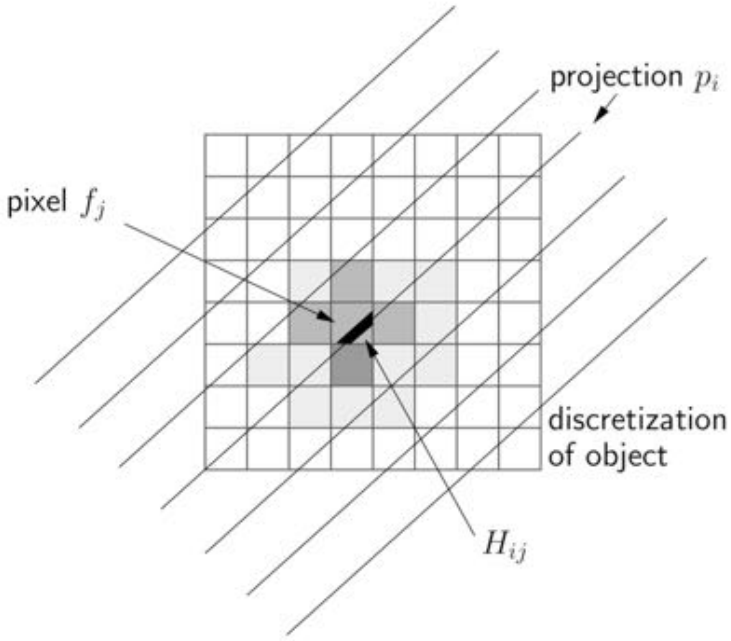

FIGURE 3.6. A pictorial view of the system model expressed in Eq. 3.9 (picture from A. Alessio and P. Kinahan "PET Image Reconstruction").

The second step is to create a system model that links image to data as expressed in the following equation.

$$\bar{p}_i = \sum_{j=1}^{N} H_{ij} f_j \tag{3.13}$$

$\bar{p}_i$ is the mean of the i-th projection and the model is represented by matrix H. This collects the

probability that a detection in the projection i is originated by an emission in the j voxel in which an activity f is contained as shown in Fig. 3.6.
The third component is the distribution model of measured data around the expected mean value $\bar{p}$. This distribution model is determined by physics processes behind the data behavior. In PET, the choice is the Poisson model. Defining L the probability that the Poisson distributed photons counts P is equal to the true photon rate p given the emission f rate vector, the Poisson model states that:

$$L(P = p \mid f) = \prod_{i=1}^{M} \frac{\bar{p}_i^{p_i} \; e^{-\bar{p}_i}}{p_i!} \tag{3.14}$$

The fourth step is the definition of the governing principle which mathematically defines the concept of best image. A well known statistical tool is the Maximum Likelihood (ML) method. In Eq. 3.14, L is the likelihood as a function of f and this technique consists in finding the $\hat{f}$ value that maximizes L.
The fifth component represents the connection of the first four components into an algorithm. The algorithm takes the measured data as input, constructs the model that links data and image and computes the optimum of the ML function. In literature, there are several algorithms dedicated to image reconstruction and one of the most used is the Maximum Likelihood Expectation Maximization (ML-EM).
L. A. Shepp and Y. Vardi are the fathers of this reconstruction method introduced for the first time in 1982 [19]. Since then, it remains the landmark for this field. This method can be expressed by the following equation.

$$f_j^{(n+1)} = \frac{\hat{f}_j^{(n)}}{\sum_{i'} H_{i'j}} \sum_i H_{ij} \frac{p_i}{\sum_k H_{ik} \hat{f}_k^{(n)}} \tag{3.15}$$

where $f_j^{(n+1)}$ is the estimation of the j voxel activity at $(n+1)$ iteration starting from the previous estimation $\hat{f}^{(n)}$. Again A. Alessio and P. Kinahan in "PET Image Reconstruction" introduced a simple scheme which is able to explain the ML-EM algorithm mechanism.
The entire reconstruction process starts with an initial guess $\hat{f}^{(0)}$ usually set to a constant value when no additional information are provided. This algorithm steps can be described as follow:

- The initial guess is moved to projection domain by $\sum_k H_{ik} \hat{f}_k^{(n)}$.
- A comparison is made between evaluated projections and measured ones. It returns multiplication factors in the projections domain.
- These factors are backprojected into image domain and applied to the initial image guess.
- The initial image is corrected and updated by weighting terms according to the system model.

- The obtained image is considered the initial guess for the next iteration and the algorithm is repeated until image convergence.

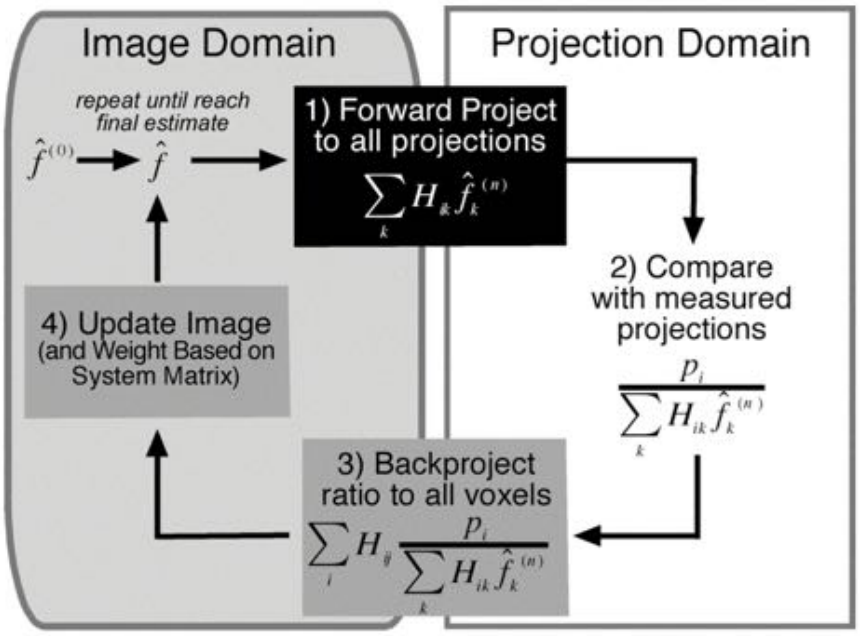

FIGURE 3.7. The relation between the image and the projection domain in the ML-EM algorithm (picture from A. Alessio and P. Kinahan "PET Image Reconstruction").

The ML-EM approach has a different convergence behavior for low and high frequency image components. In details, low frequency components converge after few iterations while high frequency ones need more iterations to converge. Low frequency components correspond to signal while high frequency ones add noise to reconstructed images. To avoid noise amplification, the algorithm stops earlier or the image is post-smoothed. Compared to filtered backprojection technique, ML-EM is more time consuming because it has to compute a forward and a backprojection for each iteration but it provides higher quality images due to a better reconstruction system description.

3.4 The ClearPEM reconstruction algorithm

As previously described in the introduction, the CrystalClear collaboration designed, projected and built a dedicated breast PET scanner focused. ClearPEM scanner consists in two detector plates that rotate simultaneously around the patient. The CrystalClear collaboration developed a C++ based reconstruction algorithm able to fully exploit the high performances of the detection system. In particular, it includes DOI information in reconstruction processes thanks to a list-mode approach. Data are analyzed and store individually without being collected in sinograms.

LORs are described by (x,y,z) coordinates of their extremities. The core of the reconstruction is a ML-EM with the same structure expressed in Eq. 3.15. The system model H is obtained for each voxel by the LOR length contained by the voxel itself. This process is based on a raytracing methods, the Siddon's algorithm that will be largely discussed in the next section. In reconstruction processes, ClearPEM algorithm includes the FOV sensitivity variation originated by geometrical reason and by detectors performances differences. This sensitivity map can be evaluated by an uniform source acquisition and by correcting the system response. Due to the ClearPEM dual heads configuration, the uniform source is represented by a planar flood phantom placed in between the two plates. After a long acquisition, the results are used to correct the data collected with patients compensating for the non uniform sensitivity. As shown in the work of B. Frisch, "Towards Multimodal Positron Emission Mammography and Ultrasonography: the ClearPEM-Sonic Project" [20], the metabolic images obtained by ClearPEM are combined with an ultrasound technique providing the morphologic images. Results of a clinical case of a multifocal breast cancer are shown in Fig. 3.8 and compared with the most common imaging techniques as CT and MRI.
In Fig. 3.8, it is possible to observe that there are small detected lesions around the main tumor mass in the left breast in MRI examination while whole-body PET/CT is not able to distinguish them. ClearPEM instead is able to observe multifocal lesions. To summarize, the ClearPEM reconstruction algorithm is a powerful tool to recover high resolution images. Its simple architecture for ray tracing algorithm allows modifications for other geometry configurations.

3.5 The Siddon's algorithm

Siddon's algorithm was introduced for the first time in 1984 by R. L. Siddon in the work "Fast calculation of the exact radiological path for a three-dimensional CT array" [21]. The aim of this algorithm is to find a way to describe radiological paths across a volume without high computational costs. Siddon's algorithm is one of the best raytracer method for a list-mode reconstruction which aims to include DOI information.
Considering a voxelated space, a path d can be described as follow:

$$d = \sum_i \sum_j \sum_k l(i,j,k)\ \rho(i,j,k) \tag{3.16}$$

where $\rho(i,j,k)$ is the voxel density and $l(i,j,k)$ is the path length contained by (i,j,k) voxel. Solving Eq. 3.16 with an exact path description running over all voxels, it is not a feasible approach from the computational cost point of view. The number of computing operations scales with the voxels number which is usually in the order of millions.
The basic idea of the Siddon's algorithm is a paradigm change in voxels interpretation: instead of considering them individually, they are treated as a collection of parallel planes. These planes are equally spaced by a distance equal to the voxels size. As presented in Fig. 3.9, this paradigm shift

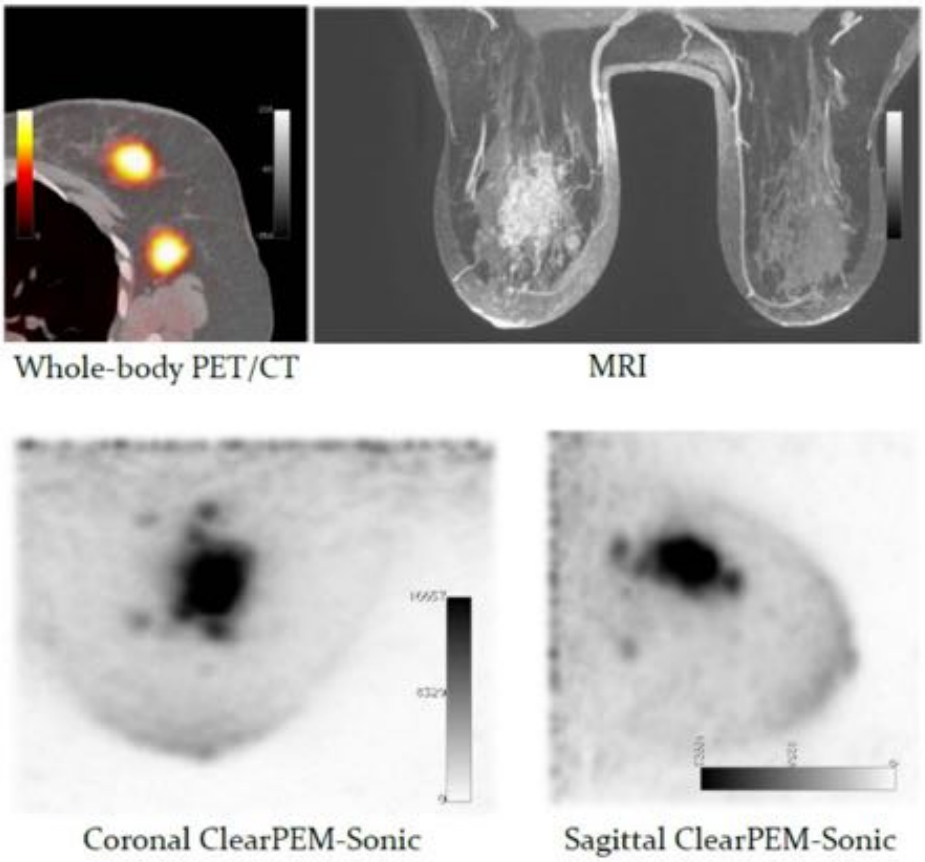

FIGURE 3.8. A comparison between a whole-body PET/CT, MRI and ClearPEM-Sonic exams of the same multifocal breast cancer (picture from B. Frisch "Towards Multimodal Positron Emission Mammography and Ultrasonography: the ClearPEM-Sonic Project").

is not responsible for any generality losses. The intersections between (1,2) line and voxels are the same in both cases. The advantage of Siddon's approach consists in the fact that only the first path-voxels intersection has to be calculated while the next ones can be evaluated by recursion. The (1,2) path can be described in the 3D space by using parametric equation as expressed in Eq. 3.17.

$$X(\alpha) = X_1 + \alpha(X_2 - X_1), \qquad Y(\alpha) = Y_1 + \alpha(Y_2 - Y_1), \qquad Z(\alpha) = Z_1 + \alpha(Z_2 - Z_1) \tag{3.17}$$

Where (X_1, Y_1, Z_1) and (X_2, Y_2, Z_2) are coordinates of path start and end and α is a parameter which runs over the path length. It assumes the value of zero at the beginning and one at the end. According to Eq. 3.17, the way a path intersects the voxel space edges arises four possible scenarios:

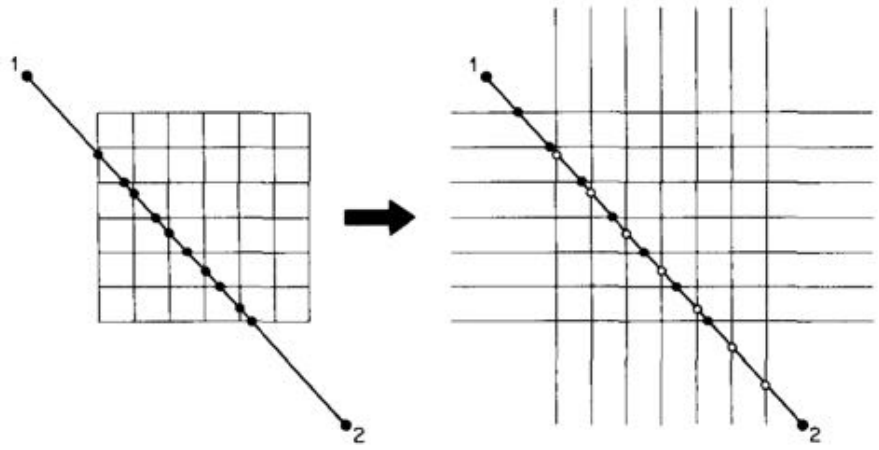

FIGURE 3.9. The change of voxels interpretation in the Siddon's algorithm (picture from R. L. Siddon "Fast calculation of the exact radiological path for a three-dimensional CT array").

- Points 1 and 2 are both outside the voxels space. The minimum value of α, defined as α_{min}, and the maximum value of α, α_{max}, are both in between zero and one.
- If point 1 is outside the voxels space while point 2 is not, α_{min} is in between zero and one while α_{max} is equal to one.
- In the opposite scenario with the point 2 that is outside the voxels and the point 1 is not, α_{max} is in between zero and one while α_{min} is equal to zero.
- When both points 1 and 2 are inside the voxels space, α_{min} is equal to zero and α_{max} is equal to one.

After calculating $(\alpha_{min}, \alpha_{max})$ range, the next steps are the evaluation of the ray intersection with each parallel and orthogonal planes by calculating a set of α values for each (X,Y,Z) direction. The three sets of α values are then merged together to create a single set. As an example, if the three sets are $(1,4,7)$, $(2,5,8)$ and $(3,6,9)$, the single set will be $(1,2,3,4,5,6,7,8,9)$. In the merged α set, the information to fully described a path d is provided. The path-voxels intersection length is obtained by the difference between two consecutive parametric values. For each intersection length, the indices that define the crossed voxel are evaluated and multiplied by the intersected length. These operations are the basis for this ray tracing algorithm that is reported in details in the R. L. Siddon's work "Fast calculation of the exact radiological path for a three-dimensional CT array". The first version introduced in 1984 was then revisited and improved by F. Jacobs and E. Sundermann in the 1998 work "A fast algorithm to calculate the exact radiological path

through a pixel or voxel space". The structure is the same as the Siddon's algorithm but the computational cost are reduced thanks to an improvement in the inner loop timing performances resulting in a faster reconstruction.

3.6 TOF-PET reconstruction

ClearPEM scanner has a coincidence time resolution in the order of 2 ns and therefore the first algorithm version does not perform TOF-PET reconstruction. Our idea is to upgrade the ClearPEM algorithm into a complete TOF-PET method in order to include the timing information in images reconstruction processes.
We directly modify Siddon's algorithm structure starting from the definition in Eq. 3.16. A radiological path d is fully described by two components, the voxels density and the length of the line inside each single voxel. Our TOF approach is reached by introducing a third component as expressed in the following equation.

$$\tilde{d} = \sum_i \sum_j \sum_k l(i,j,k)\ \rho(i,j,k)\ G(i,j,k,\Delta x,\sigma x) \tag{3.18}$$

Where $G(i,j,k,\delta x,\sigma x)$ is a 3D gaussian centered in Δx (Eq. 2.14), with a sigma in the three directions of σx (Eq. 2.15) and evaluated in the (i,j,k) voxel center. In other words, the original LOR description is reweighed by the probability calculated by the detection time difference of back-to-back gamma rays.
The first test to prove the exactness of this approach is to analytically simulate parallel LORs with a fixed σx and vary the detection time difference. In details, the chosen σx is 85 ps (200 ps FWHM) and the detection time difference is modified between -200 ps, 0 ps and 200 ps. These simulated data are reconstructed by the upgraded ClearPEM algorithm and the results of the TOF and non-TOF approach are compared in Fig. 3.10. The proof of principle of the upgraded algorithm shows the expected results: the LORs reconstructed without the timing information have uniform probability along their length. By introducing the TOF information the LORs assume a gaussian behavior. Furthermore the center of this gaussian moves according to the detection time difference as presented in Fig. 3.11.
To summarize, we successfully develop a TOFPET algorithm, based on the ClearPEM one, able to include timing and DOI information in the list-mode ML-EM reconstruction and its application will be discussed in chapter 9.

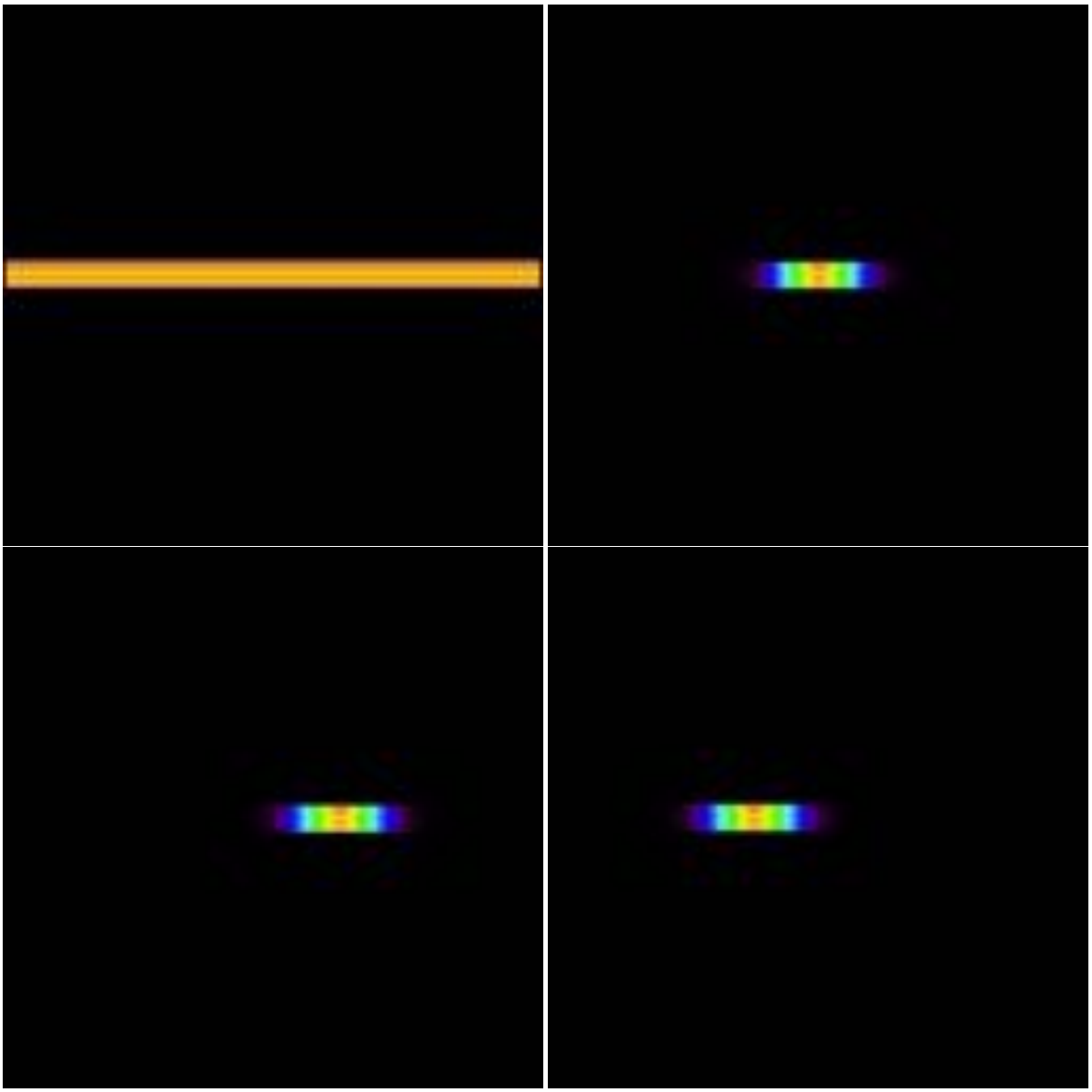

FIGURE 3.10. The working principle of the TOF upgrade of the ClearPEM reconstruction algorithm. On the left-top part the non-TOF reconstruction of parallel LORS. The other three parts represent the TOF reconstruction and it is possible to appreciate that the gaussian behavior center is moving according to the detection time difference (0 ps for the top-right, 200 ps for the lower-left, -200 ps for the lower-right part.

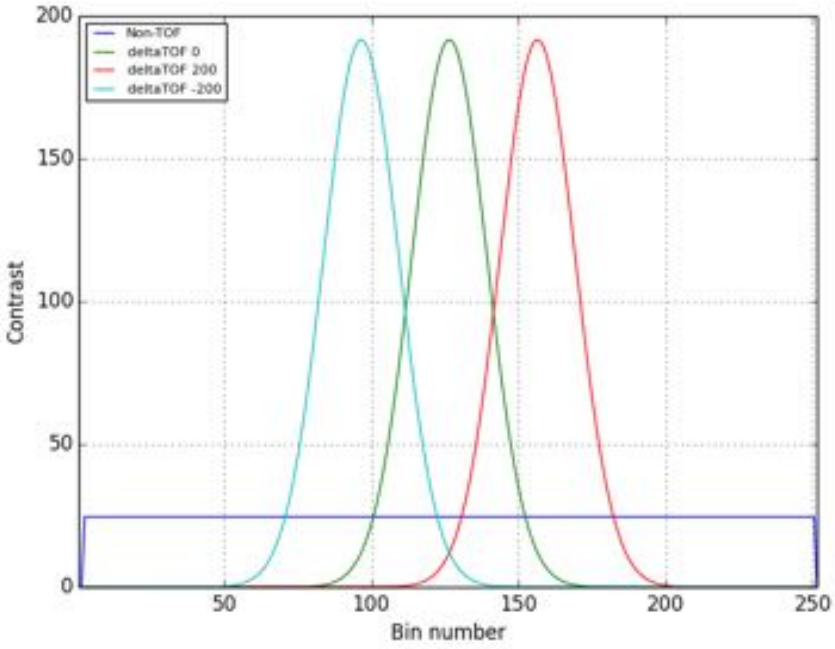

FIGURE 3.11. The profile of the reconstructed images of Fig. 3.10.

CHAPTER 4

A NEW METHOD TO EXTRACT THE INTERACTION POINT POSITION IN PET MODULE

The aim of this research work is to develop a PET module capable of reaching high performances in term of spatial and time resolution while maintaining the system complexity reasonably low. A single side read out approach is chosen able to reach the same performances of double side readout configuration. The core part of the chapter is dedicated to the method to identify the crystal in which scintillation events take place and in particular to achieve DOI information. This information is also included in the detection time evaluation in order to reach better timing resolution. The description of PET prototype modules and the experimental equipment are presented at the end of the chapter.

4.1 Single side readout PET module with high granularity

In PET systems, the spatial resolution is determined by the accuracy with which the gamma ray interaction point is recovered. Several approaches can be exploited in order to fulfill this purpose as described in chapter 2. In particular, ClearPEM scanner consists in pixellated scintillators and it exploits a double side readout in which each crystal is read by APDs on both sides. The transverse position of the interaction point is provided by identifying the hit crystal while the axial one by measuring the collected light asymmetry at the two sides of scintillators determined by an induced attenuation behavior over the crystal length.
In this study, a new approach is presented based on pixellated module in a single side readout configuration. The advantages of this approach are previously described in the introduction and they basically consist in a detector and electronic number reduction.
Compared to a double side readout approach, in the proposed single side readout configuration

the second detector is replaced by an optical light guide and an ESR layer. After the scintillation, the produced optical light spreads isotropically in the crystal. The component which travels in the direction of the photodetectors is collected by the directly coupled SiPM. The other direction component is recirculated by the light guide into the nearby crystals where it is collected by the nearby photodetectors. Studying the light distribution behavior it is possible to recover the gamma ray interaction position. In other words, the idea behind this single side readout configuration is the sharing and recirculation of the optical light which otherwise will escape from the matrix. This optical light is collected by the nearby detectors as presented in Fig. 1.2 in the introduction.

In pixellated geometries, the accuracy in the interaction point determination is dominated by the scintillators section. Decreasing this section returns better spatial resolution but it leads to a higher number of detectors. Enabling light sharing mechanism among crystals opens the possibility to exploit smaller crystals without increasing the detectors number. This is possible thanks to a greater than one to one coupling between scintillators and detectors. The hit crystal identification is achieved by studying the collected light distribution in the crystals matrix. An example of this light sharing behavior can be found in Fig. 4.1. Red lines and capitals letters represent a detector array while the scintillators are represented in blue. A four to one coupling configuration is described but the idea can be applied to a generic $m \times m$ scintillators matrix and $n \times n$ detectors array. For simplicity, only four crystals coupled to the central detector are schematized in green. The idea is that if the scintillation takes place, for example, in the right-upper crystal more light will be shared through the light guide on top in scintillators close to that region (B,C,E) compared to the light that reaches the ones coupled to (D,F,G) detectors. If the hit crystal is the one on left-lower corner, light sharing will be in opposite direction distributing more light in regions (D,F,G) than in (B,C,E).

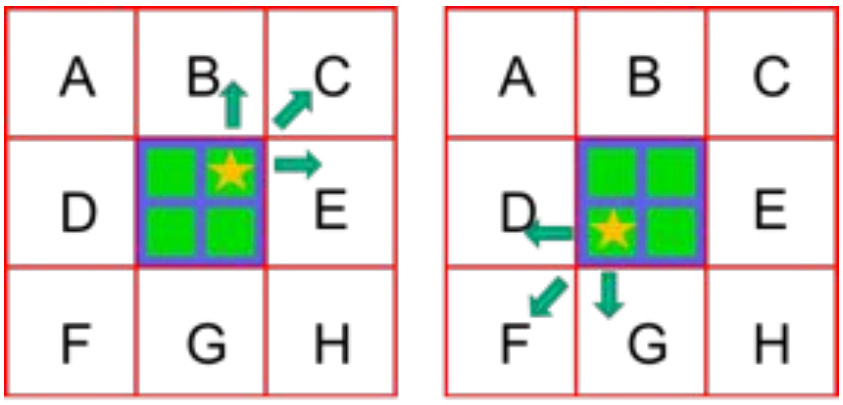

FIGURE 4.1. The different way in which the light is shared among the nearby scintillators according to the position of the hit crystal.

The interaction axial position corresponds to DOI information and several methods to reach this information are presented in the introduction. In the proposed single side configuration, the light asymmetry of double side readout configuration is overcome by evaluating the light difference between directly coupled and nearby detectors. Furthermore, light attenuation behavior needs to be introduced along the scintillator main axis in order to correlate interaction position and collected light distribution. A simple way is an optical treatment of scintillators lateral surface: the depolishing. It consists in an increased roughness of the crystal surface which leads to light attenuation over the length of the crystal as presented in Fig. 4.2. This mechanism was already demonstrated in double side readout configuration by ClearPEM scanner.

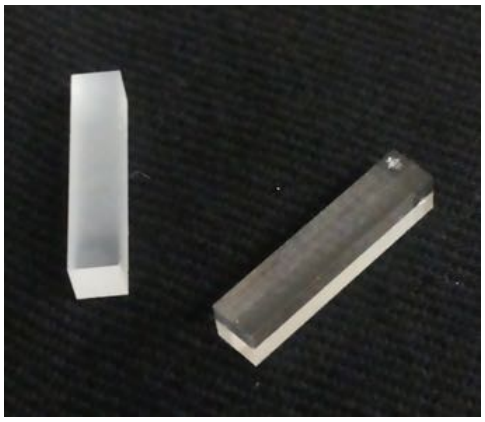

FIGURE 4.2. The effect of the depolishing on a crystal on the left compared to one that does not undergo to the optical treatment.

Depolishing the scintillators lateral surfaces enables the module DOI capability while it affects timing performances. Timing resolution is determined by time spread Δt of optical photons collected by detectors and it can be described as follow.

$$\Delta t \propto \sqrt{\frac{\tau_d \times \tau_r}{LY_{out}}} \tag{4.1}$$

τ_d is the decay time, τ_r the rise time and LY_{out} the light yield extracted from scintillators. τ_d and τ_r are properties of the scintillator mean. The attenuation behavior induced by depolishing affects the detected light distribution increasing the LY_{out} spread. According to Eq. 4.1, this leads to broaden detection time distribution resulting in worse timing resolution. Light sharing mechanism can be exploited also to correct for this effect by including DOI information in the detection time evaluation. This deconvolution allows separating the depolishing contribution from the timing resolution evaluation.

4.2 Procedure to extract the interaction point position

Considering a pixellated module based on $m \times m$ scintillators matrix coupled to $n \times n$ detectors array, for each gamma ray interaction, the energy deposited in the scintillators arises a voltage signal in each detector. Starting from the collected charges the purpose is to recover the (x, y, z) interaction position. The idea is to consider a set of variables which are combinations of the collected information and linked them to the position coordinates.
For the transverse position, a well know method is the Anger logic scheme presented for the first time in 1958 by H. O. Anger [22]. If p_i is the charge collected by the i-th detector and X_i and Y_i are the positions of the i-th detector center, the following equations can be written:

$$u = \frac{1}{P} \sum_{i}^{N} p_i \times X_i \tag{4.2}$$

$$v = \frac{1}{P} \sum_{i}^{N} p_i \times Y_i \tag{4.3}$$

$$P = \sum_{i}^{N} p_i \tag{4.4}$$

where u and v are indicators of the interaction position in (X, Y) space, N the number of photodetectors involved in the calculation and P is the total light collected by N photodetectors. Usually, the light sharing concerns crystals coupled to photodetectors which surround the one coupled to the hit crystal and therefore N can be restricted to nine. Thanks to the position dependent distribution of shared light, u and v pinpoint the crystal in which the gamma ray interacts. The idea behind this method does not present any constraint to the number of scintillators coupled to a single detector.
The axial position Z represents the DOI information [23]. In the proposed single side readout approach, this information is recovered by the ratio between light collected by the directly coupled detector and light shared in the nearby ones. This idea can be written as follow:

$$w = \frac{p_{max}}{P} \tag{4.5}$$

where p_{max} is the maximum of light which is collected by the detector directly coupled to the hit crystal.

4.3 DOI correction for detection time evaluation

The induced attenuation behavior over the crystal length is mandatory to achieve the DOI information but it leads to timing resolution degradation as explained in section 4.1. If known,

the correlation between DOI and detection time distribution of optical photons can mitigate this effect as presented in Fig. 4.3.

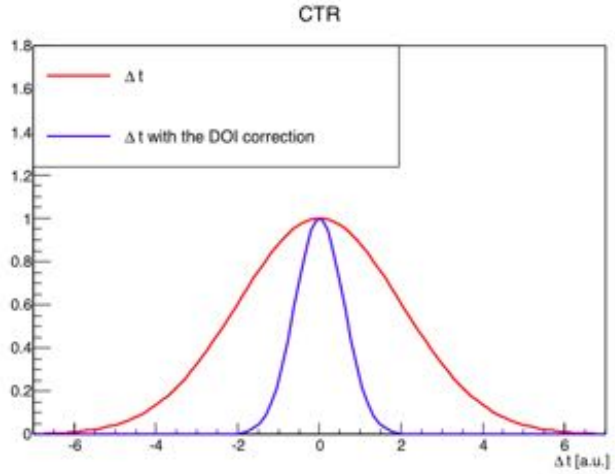

FIGURE 4.3. The proposed idea of correcting the detection time distribution by exploiting DOI information.

The proposed procedure to include DOI information in the detection time evaluation can be applied to a generic pixellated system based on light sharing mechanism in single side readout configuration. The speed v with which the optical photons travel through a medium can be derived by the Eq. 4.6.

$$v = \frac{c}{n} \tag{4.6}$$

Where n is the medium index of refraction and c is the speed of light in vacuum. According to the LYSO index of refraction (1.8), in a 15 mm long crystal, the optical photons have a time jitter in the order of 30 ps between optical photons generated in the crystal top part and close to the detector. This time jitter depends only on the crystal length regardless the optical treatment of lateral surfaces. As previously mentioned in Eq. 4.1, the depolishing affects the LY spread deteriorating the system timing performances. Furthermore, the attenuation behavior is responsible for increasing the collection time jitter of optical photons modifying the transmission behavior along the crystal length. This jitter in the detection time distribution is proportional to DOI as presented in Fig. 4.4.
Knowing the DOI information it is possible to correct for this position dependent delay by eliminating the jitter contribution from the detection time distribution of optical photons. Furthermore, if the timing information of shared light is available, it can be combined in the DOI dependent delays evaluation. As previously described, also the shared light distribution has a DOI dependency that affects the detection time distribution. The idea to correct the interaction time with

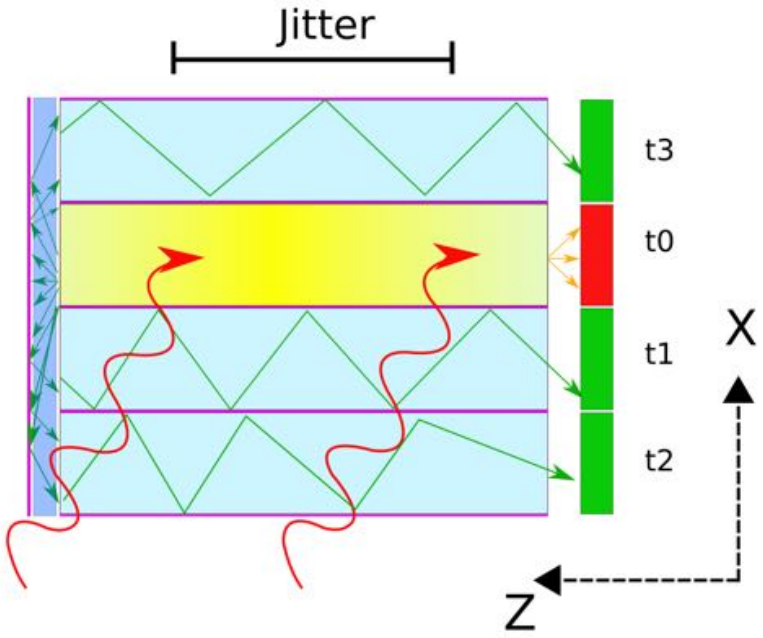

FIGURE 4.4. The DOI dependent jitter can be corrected not only by including the detection time delay t0 in the detector directly coupled but also considering the delays t1-t3 of the light collected by the nearby detectors.

the DOI induced delay of the shared light can be expressed by Eq. 4.7.

$$\hat{t} = \frac{\sum_{i}^{N}\left[(t_i - \delta_i(DOI)) \times \frac{1}{\sigma_i^2(DOI)}\right]}{\sum_{i}^{N}\frac{1}{\sigma_i^2(DOI)}} \tag{4.7}$$

Where t_i is the detection time at the i-detector, $\delta_i(DOI)$ is the detection time delay due to DOI position along the crystal main axis and $\sigma_i(DOI)$ is the sigma of the detection time distribution. These $\sigma_i(DOI)$ act as weights for timing contribution of nearby detectors. The corrected detection time $\hat{t}$ is decoupled from the jitter effect arisen by DOI and this improves the system timing performances.

4.4 Proposed modules

The method presented in the previous section aims to reach (x, y, z) interaction position and $\hat{t}$ detection time for each gamma ray interaction. To verify its correctness and accuracy, this method is tested on different PET modules.
They are based on pixelated LYSO matrix and a MPPC array in single side readout configuration. As already discussed, light sharing mechanism opens the possibility to adopt smaller crystals

without increasing the number of detectors thanks to a greater than one to one coupling configuration. Therefore matrices with different crystals dimension are tested and the dimensions are reported in Tab. 5.1.

	Number of crystals	Crystal size	Crystal length	Coupling
4x4 crystals matrix	16	3.1 mm	15 mm	1 to 1
8x8 crystals matrix	64	1.53 mm	15 mm	4 to 1
12x12 crystals matrix	144	1 mm	15 mm	9 to 1

TABLE 4.1. Crystals matrices features.

In each configuration, crystals are separated by a 70 μm foil of enhanced specular reflector (ESR) to avoid optical photons transition through lateral surfaces. Crystals and separation foils are in dry contact and therefore an external teflon layer is wrapped around the entire matrix to keep all the parts in place. The complete dimension of each matrix is 12.8x12.8x15 mm^3. For each matrix, a sample with polished and one with depolished crystals lateral surface is exploited.
As photodetector, an Hamamatsu TSV MPPC array (S12642-0404PB-50) is adopted. It is made by 16 SiPMs, each with an active area of 3x3 mm^2. Each SiPM is composed by 3464 SPADs and the distance between the center of two adjacent SiPMs (pitch) is 3.2 mm. In Fig.4.5 a dimensional outline of the Hamamatsu MPPC is provided.

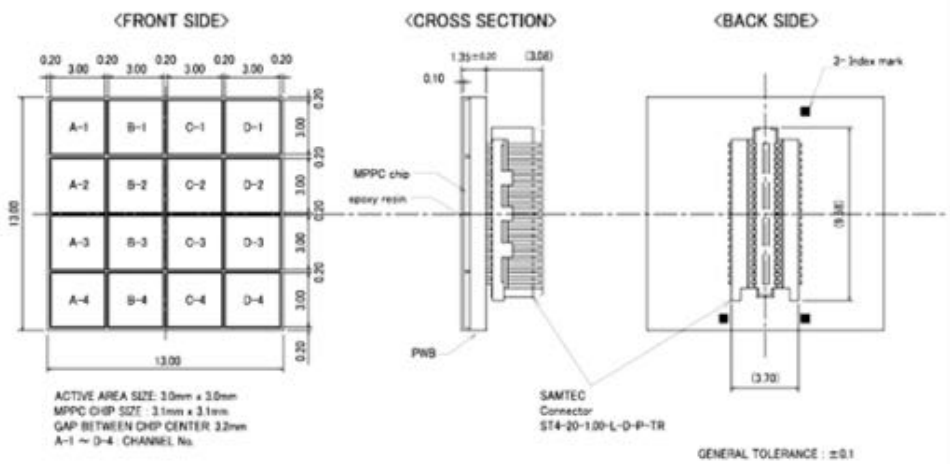

FIGURE 4.5. Dimensional outline of Hamamatsu MPPC (picture from the Hamamatsu S12642-0404PB-50(X) data sheet).

The scintillator matrix is coupled to the MPPC detector on one side. In between the two components a thin layer of Rhodorsil 47V optical grease is applied to maximize the optical transmission. If the module and the detector are in dry contact, a thin air layer (index of refraction = 1) separates the two components reducing optical transmission. Optical grease has an index of refraction of 1.4 improving the transmission efficiency of optical photons from scintillators to detectors.
Instead of a second detector, a glass light guide and an ESR layer are placed on the other side to recirculate the optical light in the matrix. The thickness of the glass layer is 1 mm. The coupling between glass and scintillators is made by using optical grease while light guide and ESR foil are in dry contact. All components are kept in place by using a dedicated 3D-printed plastic holder.

4.5 Experimental equipment

Performances evaluation of proposed modules requires dedicated experimental setups to measure the accuracy of the interaction positioning, energy, DOI and timing resolution. Three different acquisition configurations are exploited for this purpose.

4.5.1 PET-like setup

To prove interaction point identification capability and measure the energy resolution, the tested module is irradiated by a ^{22}Na radioactive source placed 10 cm above the scintillator side not coupled to detectors. The module is plugged to a custom made acquisition board which extracts the detectors signals and provides the SiPMs bias voltage. All the 16 MPPC channels are read out by an integration charge digitizer (CAEN DT5740). The entire system is placed in a black box that does not allow external light to compromise the measurements and temperature is kept constant around 18°. A scheme and a picture of the setup are shown in Fig. 4.6.
The acquisition trigger is provided internally. This trigger modality starts the acquisition every time one of the 16 channels is above a certain energy threshold. All signals are then acquired in parallel in order to collect the light shared in the matrix. The digitizer performs the integration of voltage pulses returning the digital value of collected charges.

4.5.2 External tagging setup

To prove the idea that the w coordinate acts as DOI indicator, a dedicated experimental setup is developed. The fundamental requirement is to know a priori the interaction position along the crystal main axis. The setup is based on the PET like setup and the module is placed on a x-y-z movable stage. The radioactive source is positioned on the module lateral side aligned to a tagging crystal. This consists in a LYSO crystal with dimensions of 1.5 x1.5 x 15 mm^3 coupled to a single SiPMs as presented in Fig. 4.7.

The crystal is wrapped by teflon and lateral surfaces are polished to maximize the light collection.

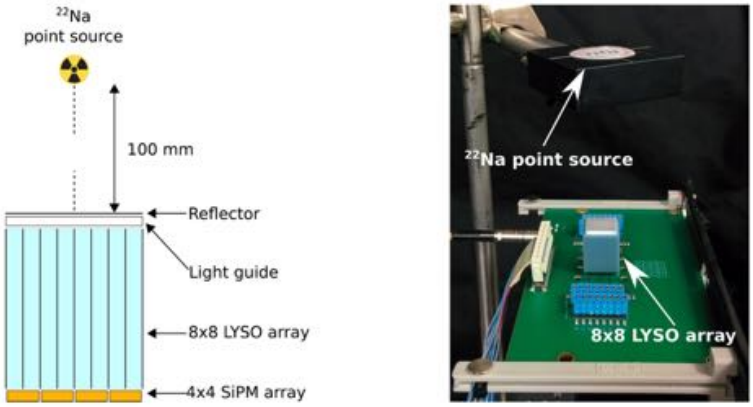

FIGURE 4.6. The experimental setup exploited to prove the possibility of separating and identifying the single crystal spectrum in different coupling configuration between scintillator and detectors.

This crystal and the source are mounted on the same support which mechanically guarantees the correct positioning. The alignment of module, source and tagging crystal is verified by a laser. The tagging crystal provides the acquisition trigger to the digitizer. Every time a scintillation event which exceeds a programmable threshold occurs in the external crystal, the charge signals of the entire system (MPPC and external SiPM) are acquired in parallel. This configuration works as an electronic collimation for the gamma ray radiation. Moving the module position is possible to perform a scan over the crystal length in order to study the w behavior at different heights. The distances between the setup components define the dimension of this vertical region. Ideally, the best condition is to maximize the distance between source and tagging crystal reducing the size of the illuminated vertical region. As drawback, the system sensitivity will drastically drop affecting the acquisition time in a negative way. On the other way, if the module-source distance is higher than the source-tagging crystal distance, the system sensitivity but also the vertical region dimension are increased affecting the measurements correctness. The target of this study is to reach a DOI resolution in the order of few millimeters. Having a vertical region with a dimension comparable or even bigger than this value represents a limit for the relevance of the entire work. The results, in fact, would be dependent just on the vertical region dimension and not on the intrinsic DOI capability of the module. According to simple trigonometric calculations, the vertical region size can be evaluated as described in the following equation.

$$Z = \left(\frac{a}{b}\right) \times (S + L) + L \tag{4.8}$$

where Z is the vertical dimension of the interaction region, a is the source-module distance, b is the tagging crystal-source distance, L is the tagging crystal size and S is the source diameter as presented in Fig. 4.8.

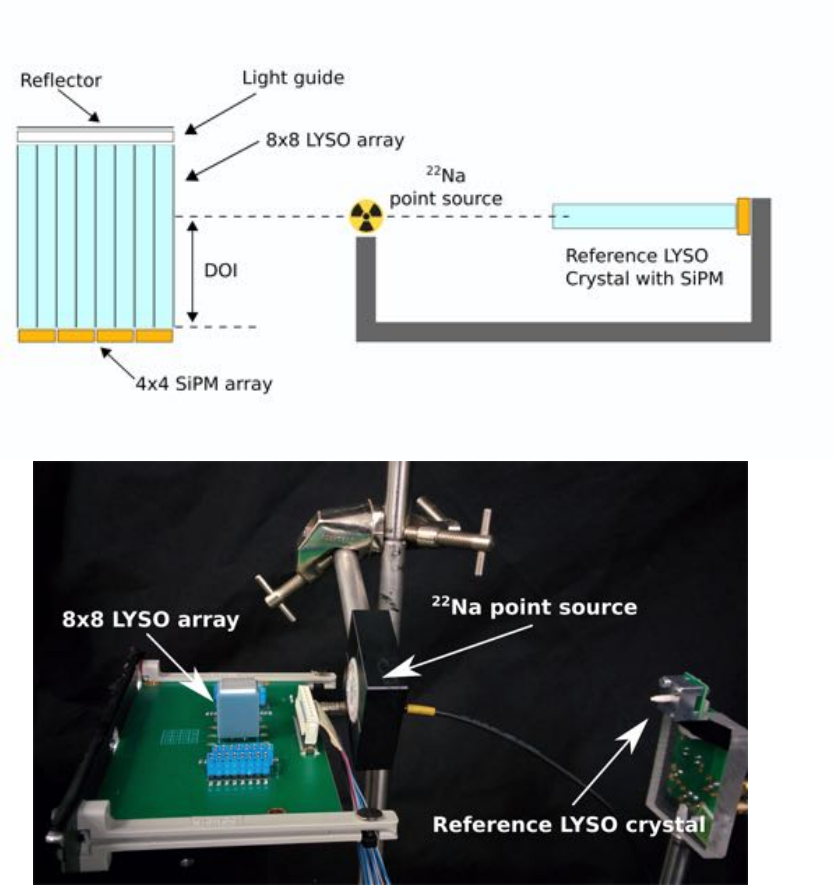

FIGURE 4.7. On top, a scheme and on bottom the picture of the electronic collimation setup.

This evaluation is limited due to the fact that the scintillator response is not included. In other words, due to the scintillation mechanism, the detection probability of a gamma ray is higher if it travels perpendicular to the crystal main axis. To evaluate the dimension of the spot, this probability variation has to be taken into account. This is achieved by GEANT4 simulation. For values of a and b respectively 2.98 mm and 6.39 mm, simulation results show a vertical region size of 1 mm (FWHM) compared to 2.2 mm expected by Eq. 4.8 as presented in Fig. 4.9.
The longitudinal dimension is equal to the vertical one and therefore only one crystals row can be simultaneously illuminated. By moving the x-y-z stage it is possible to repeat the measurements for each crystals row characterizing the entire module.

4.5.2.1 The CAEN DT5740 digitizer

Both PET like and external tagging setups exploit the CAEN DT5740 digitizer to integrate the voltage signal. This integration returns the charge collected by the detector digitizing the

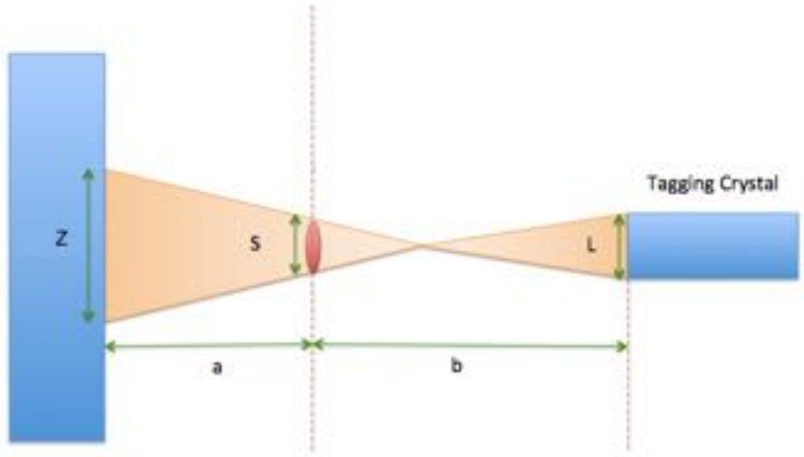

FIGURE 4.8. Scheme of the electronic collimator setup.

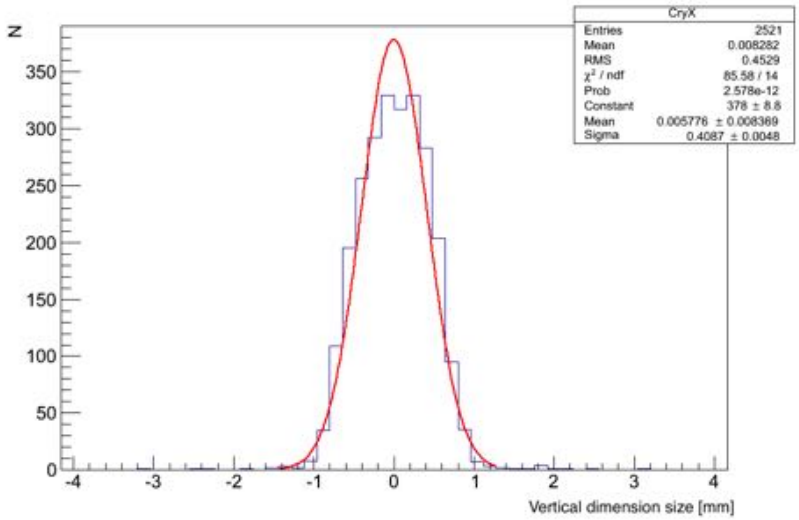

FIGURE 4.9. Vertical dimension of the illuminated spot obtained by GEANT4 simulation.

analog input signals. Due to high linearity, this digitalization method is the most suitable for spectroscopy measurements. CAEN DT5740 is a 32 Channel 12 bit 62.5 MS/s (65 MS/s using external clock) Desktop Waveform Digitizer and here the main features are listed (from caen.it):

- 12 bit 62.5 MS/s ADC.
- 16 or 32 channels.

- MCX connectors to access just 16 channels.
- ERNI SMC Dual Row 68pin connector to access the 32 channels.
- 2 Vpp single ended input range.
- USB 2.0 interface that allows data transfers up to 30 MB/s.

As described in the previous sections the acquisition trigger can be provided externally or internally from one or a group of digitizer channels.

FIGURE 4.10. The DT5740 digitizer. The MCX and the ERNI connection for the input are visible as the dedicated external trigger port.

The digitizer linearity is tested by using a pulse shape generator. The trigger is provided externally and different amplitude pulses are sent to the digitizer. The results are shown in the plot below showing a good linear response.

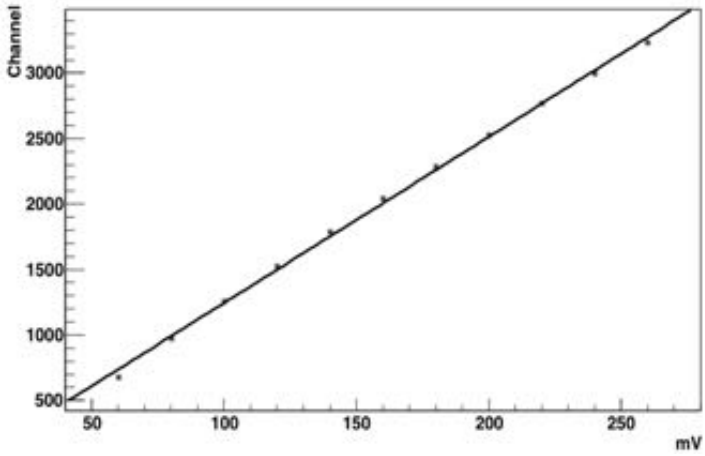

FIGURE 4.11. The linearity of the CAEN DT5740 digitizer as a function of the amplitude of the input signals.

4.5.3 Preliminary calibration of MPPC response

As described in section 2.3.2, SiPM detection system is based on several SPADs working in Geiger regime. If they are joined together in SiPMs, SPADs are able to provide energy information of detected events. The energy response linearity is limited by SPADs number in each SiPM. When the number of SPADs fired N_{fired} is comparable to the total SPADs number N_{max}, the probability of missing a photon reaches one. Additional light will not be detected saturating the output of the SiPM. This saturation behavior can be described by the following equation:

$$N_{fired} = N_{max}(1 - e^{-\epsilon \frac{E}{N_{max}}}) \tag{4.9}$$

where E is the incoming gamma ray energy and ϵ is the number of pixels activated by energy unit.
A calibration procedure is needed to correct for SiPM saturation behavior and to obtain a linear energy response. This procedure is performed by using a 4x4 LYSO matrix coupled to the 4x4 MPPC. Keeping in mind that this saturation mechanism is an intrinsic property of the detectors, the results of this calibration can be applied also to the 8x8 and 12x12 LYSO matrices. Furthermore, comparing to the configuration presented in Section 4.4, the glass light guide on top of the matrix is removed while the ESR layer is placed in dry contact with scintillators to maximize the light collection. Indeed the light sharing is not needed in this calibration procedure. This calibration is performed by several sources acquisition with different emission energies in PET like setup. In the table below the different sources and the energy of the gamma ray emitted are listed. For each acquisition, the charge collected by each detector channel is plotted in an

Source	Symbol	Gamma ray energy
Cobalt	Co_{57} Co_{60}	122 KeV 1173 KeV and 1332 KeV
Barium	Ba_{133}	356 KeV
Sodium	Na_{22}	511 and 1275 KeV
Cesium	Cs_{137}	662 KeV

energy spectrum in ADC channels unit. The peaks of all source spectra are fitted by a gaussian function and their position is plotted as function of the source energy. The Eq.4.9 is expressed in number of pixels fired while, in the plot in Fig.4.12, the response of the detector is given as ADC channel that means as collected charge. Due to a linear relation between the number of pixels fired and charge collected the saturation correction can be applied without any differences by expressing the detector response in both unit. From Eq.4.9, the saturation behavior can be written as follow in ADC channels unit.

$$ADC\ channels = p_0 \times \left(1 - e^{\frac{-Energy \times p_1}{p_0}}\right) \tag{4.10}$$

This function is used to fit the point in the graph obtaining the correction parameters p_0 and p_1 to linearize the SiPMs energy response. Comparing Eq. 4.9 and Eq. 4.11, p_0 corresponds to N_{max} meaning that it represents the maximum of collected in ADC channels reachable by the SiPM.

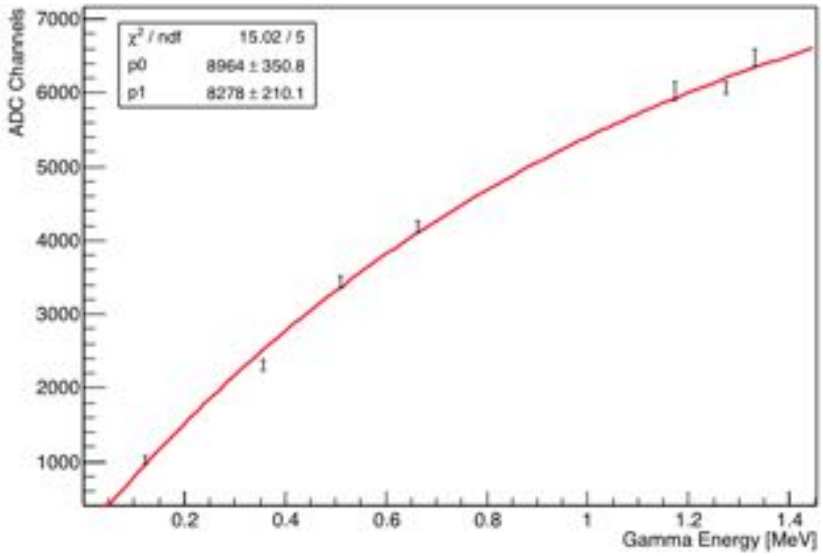

FIGURE 4.12. The saturation behavior of the SiPM as a function of the energy of the incoming gamma ray.

In particular only p_0 is involved in the ADC channels linearization which is performed by the following equation.

$$ADC\ channels_{corr} = -p_0 \times log\left(1 - \frac{ADC\ channels}{p_0}\right) \tag{4.11}$$

4.5.4 Timing setup

An indicator of timing performances is the coincidence time resolution (CTR). It is the distribution width (FWHM) of the detection time difference of back-to-back gamma rays emitted from the same position, usually a point source.

$$CTR = FWHM(t_1 - t_2) \tag{4.12}$$

where t_1 is the detection time in detector 1 and t_2 in detector 2. One of the best ways to evaluate CTR is to take advantage of an external LYSO crystal used as a reference. The dimensions are

3x3x15 mm^3, the lateral surfaces are polished and it is wrapped by teflon. It acts as the trigger of the acquisition and it faces the tested module as presented in Fig.4.13. In between these two components, a ^{22}Na radioactive source is placed.

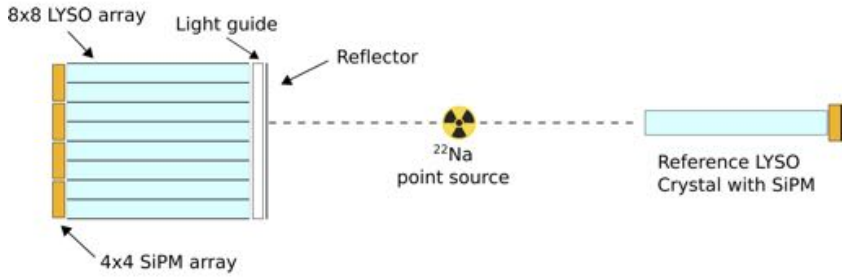

FIGURE 4.13. The timing evaluation setup. The external tagging crystal main axis relies on the direction of the main axis of the module crystals and they face each other.

The readout chain is based on Time-Over-Threshold approach obtained by a NINO chip coupled to a high performances time to digital converter (HP-TDC) from CAEN.

4.5.4.1 The NINO chip

SiPMs have pulse shape with a rise time of few nanoseconds. To evaluate the detection time difference $t_1 - t_2$, the time binning of the electronic system needs to be in the order of ten picoseconds to perform precision measurements. This is not the case of the CAEN DT4750 digitizer. SiPM pulse length is in the order of few microseconds and the digitizer integrates the entire voltage signal to ensure linear energy response. Due to limited buffer memory, CAEN DT4750 has a time binning of 16 nanoseconds making sub nanosecond timing measurements unfeasible. For this reason, the timing setup exploits the TOT technology by using a NINO chip. This was developed for the Time Of Flight (TOF) detector in the ALICE experiment at CERN in 2004 [24]. Lab27 decided to apply this technology to medical application thanks to its precision in timing measurements.
This chip is an ultrafast low-power amplifier discriminator. Starting from a input signal, it returns a square wave of a certain width as presented in Fig. 4.14. This is directly related to the time that the signal stays above a programmable threshold. In other words, when a signal exceeds the threshold, the NINO chip starts generating a square wave. It is ended when the signal drops below the same threshold. The value of the threshold has to be chosen in such a way that the noise is discarded but also that does not eliminate good events. Furthermore, it has to be reasonably lower compared to the amplitude of the signal targeted in the acquisition to reduce

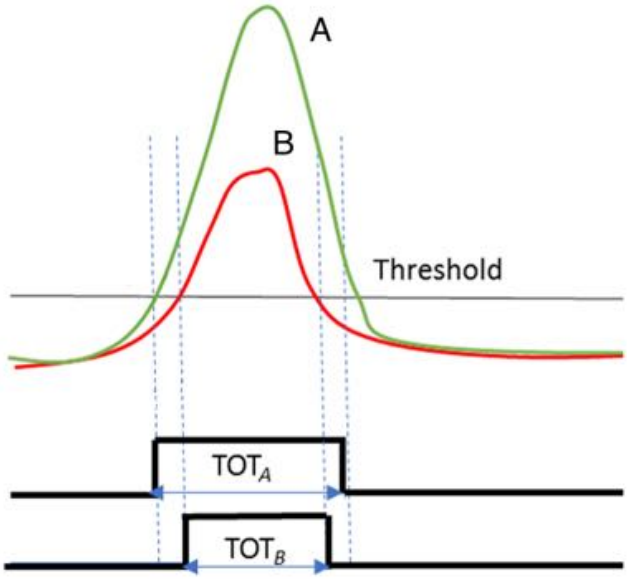

FIGURE 4.14. ToT technique. (image from "Optimization of eyesafe avalanche photodiode lidar for automobile safety and autonomous navigation systems", by G.M. Williams.)

the amplitude dependencies.

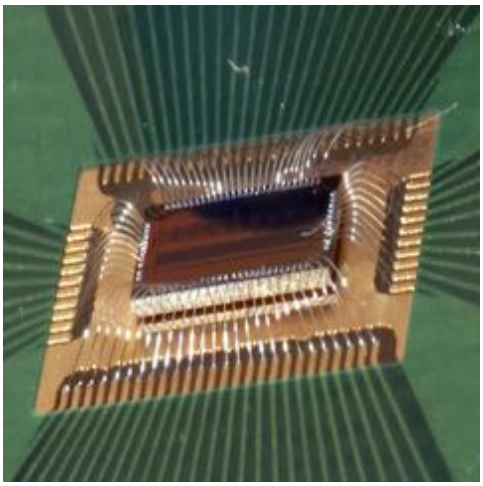

FIGURE 4.15. The NINO chip. (image from KT CERN website)

The output square wave is then processed by a TDC to digitalized the information: the outputs are the start and the end time of the signal. This acquisition chain performs precise time measurements thanks to an accurate evaluation of the start time of the signal. In principle, it

is possible also to access the energy information from the width of the square wave generated by the NINO chip. However, the energy response is not linear and is strongly dependent on the pulse shape.

CHAPTER 5

IDENTIFICATION OF THE INTERACTION POSITION AND DOI MEASUREMENTS

In this chapter, experimental measurements are performed to prove the light sharing method presented in the previous chapter. In particular, the experimental confirmation of DOI capability in single side readout configuration is presented in section 5.2.

5.1 Light sharing measurements

By using the PET-like setup presented in section 4.5.1, all coupling configurations are tested in order to confirm the hit crystal identification. The matrix crystals are irradiated by a ^{22}Na radioactive source placed 10 cm above. The acquisition provides enough data for a complete characterization in 15-20 minutes. As previously discussed, the trigger is provided internally. This means that the acquisition starts when a signal in the MPPC array is above a programmable threshold. All the pulses are collected in parallel and digitalized. For each event, the charge collected by each detector is recorded as output of the acquisition chain. Following the method described in the previous chapter, Eq. 4.2, Eq. 4.3 and Eq. 4.5 are applied to data in order to recover the interaction point of the event.
Considering the 4x4 LYSO matrix, a (u,v) graph can be obtained as presented in Fig. 5.1 where 16 accumulation regions can be identified corresponding to the 16 crystals. To provide an explanation of the (u,v) plot, the nature of the collected data has to be discussed. Incoming gamma rays can deposit all their energy in one single crystal by photoelectric interaction. These events are reconstructed in the density regions which correspond to signal events of the 16 crystals. Another possible scenario is that gamma rays release part of the energy in one crystal through Compton interaction and deposit the remaining energy in one or more other crystals. For the nature of

these events, their (u,v) coordinates are the average of hit crystals positions weighted by the energy fraction deposited in them. They arrange as a diffuse cloud under the accumulation region of the signal events. Unless the timing order of these multiple interactions is recovered, these events represent a source of interaction point misidentification. In this study, these events are considered background and discarded.

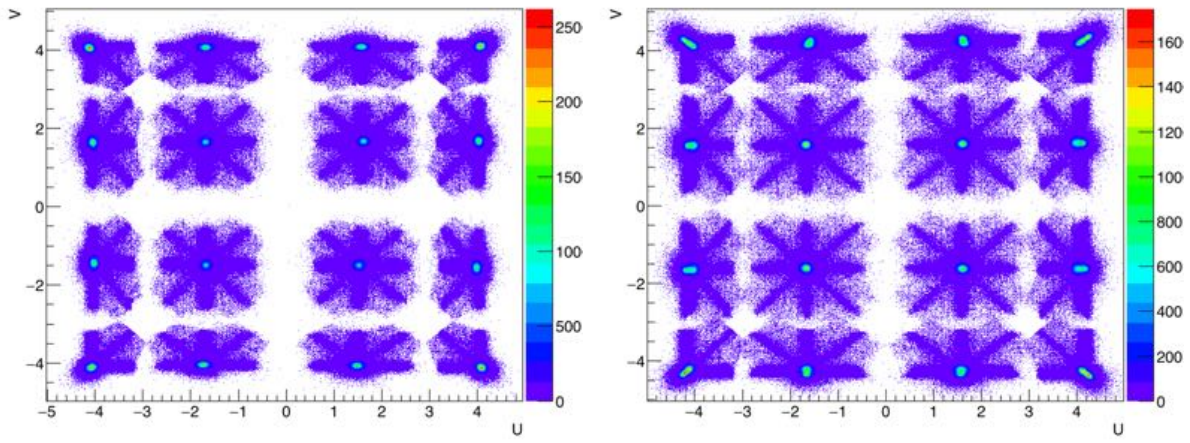

FIGURE 5.1. (u,v) plots for polished (left) and depolished (right) 4x4 LYSO matrix.

Depolished and polished samples are tested and no differences in the (u,v) plot are seen in central crystals. On edges crystals, the depolished sample shows a broader distribution of accumulation regions and a possible explanation is the light attenuation behavior induced by depolishing.
The module design is based on light sharing mechanism. This enables optical photons generated by gamma rays interaction to be spread among several detectors. In this configuration, accessing the energy spectrum by considering only the directly coupled detector is incorrect due to the fact that part of the information is carried and spread by optical photons in nearby detectors. The best approach is to sum the light collected by the detectors involved in the shared light collection in the same way as the P value is evaluated in Eq. 4.4. Recovering the hit crystal is not an issue due to the fact that only one crystal is coupled to a detector. In fact, the hit crystal is the one coupled to the detector which collects the higher charge p_{max}. Plotting P for each scintillation event, the energy spectrum is recovered for each crystal. A comparison between polished and depolished crystal is presented in Fig. 5.2.
The photopeak width is larger in the depolished sample compared to the polished. This difference is expected due to broader light output originated by depolishing as discussed later in section 5.4. The same measurement is performed with the 8x8 LYSO sample. The results are shown in Fig.5.3 confirming that signal regions are also identified in a greater than one to one coupling configuration between scintillators and detector.
The (u,v) plot plays a key role in the recovering of single crystal spectra. In details, setting proper

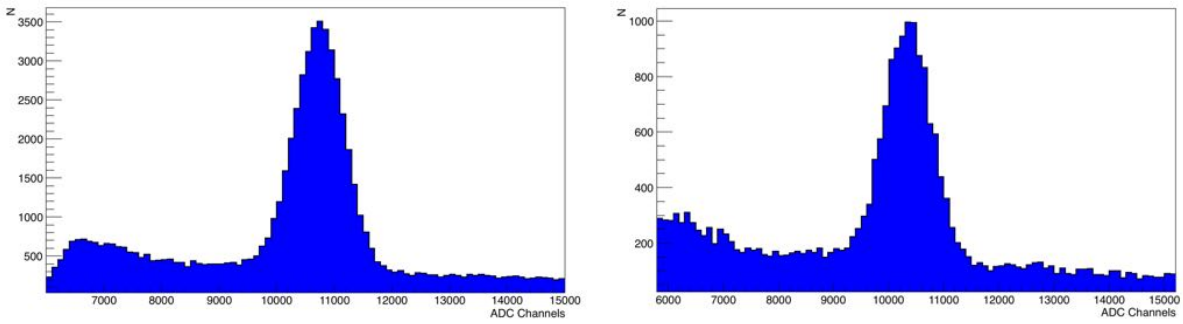

FIGURE 5.2. (u,v) plots for polished (left) and depolished (right) 4x4 LYSO matrix.

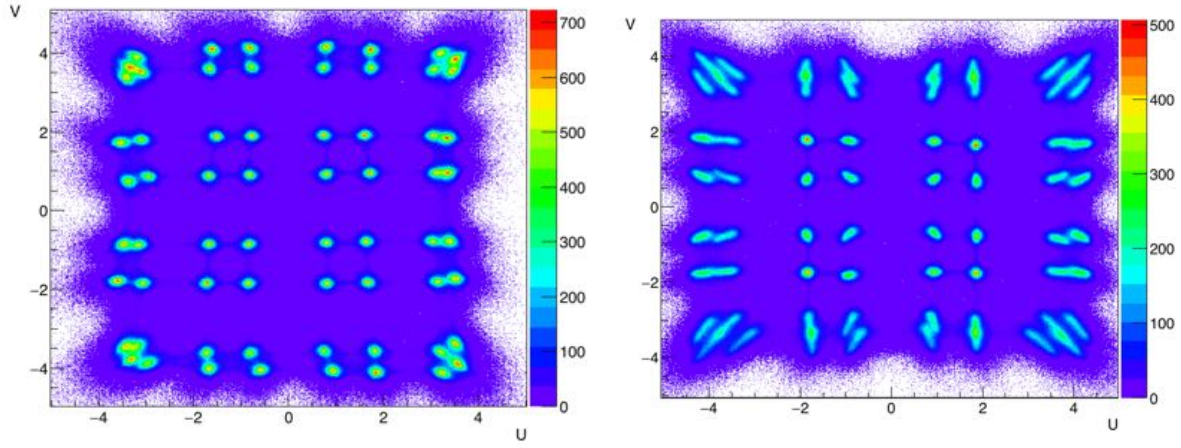

FIGURE 5.3. (u,v) plot for the 8x8 samples. On the left the polished matrix and on the right the depolished one.

limits on u and v allows accessing to single crystal energy spectra. In some lateral and corner crystals different density regions are merged together in particular in the depolished matrix. In this coupling configuration, the effect of broadening the position distributions affects the ability to identify hit crystals. Identical tests can be performed also on the 12x12 samples. In this configuration, the crystals separation is not achieved in the corners even in the polished sample as presented in Fig. 5.4. On the other hand, the separation of the central crystals is still possible. Results of crystals separation can be summarized in the table 5.1.

Separation problems in the corners arise from shared light which escapes from the matrix for geometrical reasons. There are no nearby crystals to collected these light contributions. In a complete assembled detector this light is collected by nearby modules mitigating this low separation capability in these crystals.

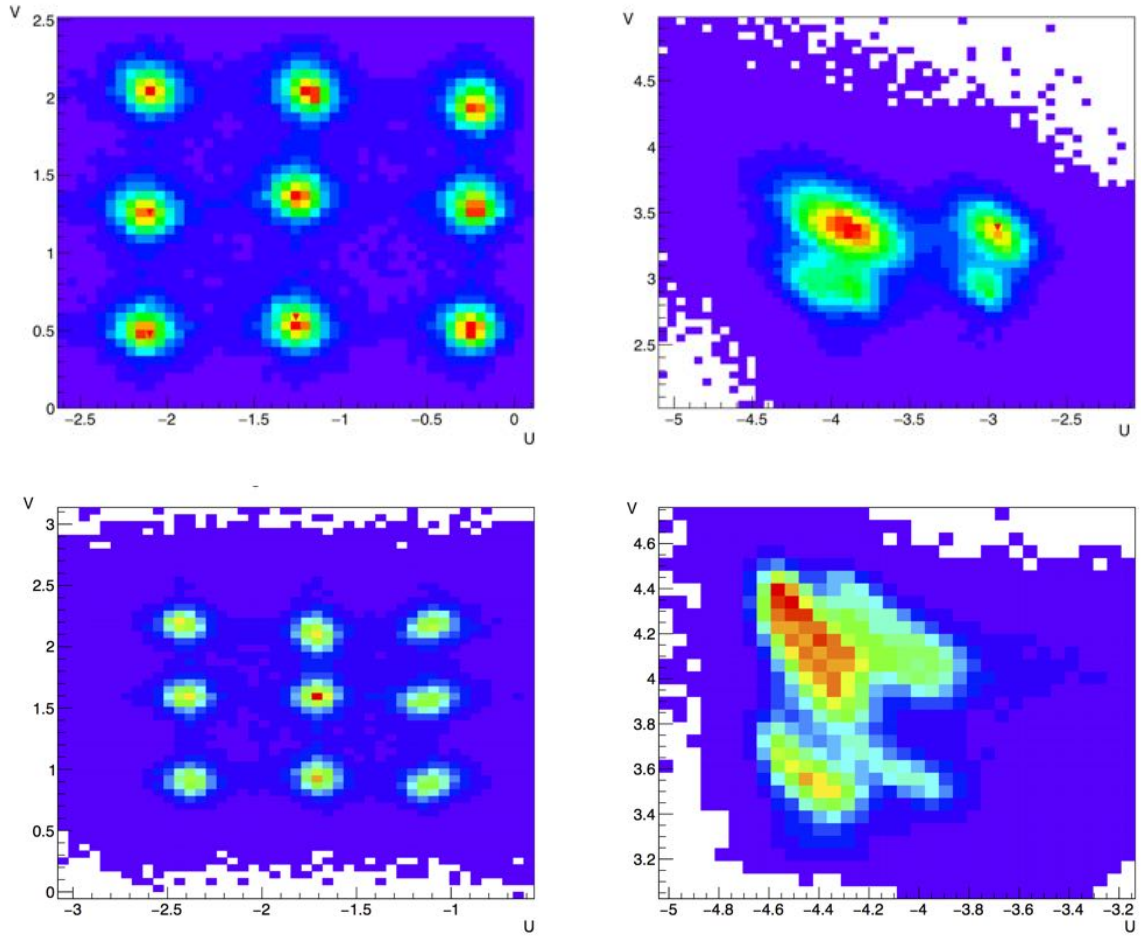

FIGURE 5.4. (u,v) plot for the 12x12 samples. On top the polished samples with central crystals (left) and lateral ones (right).Below the depolished samples with central crystals (left) and lateral ones (right)

5.2 DOI measurements

In order to verify the correlation between w and DOI, measurements with the external tagging setup are performed. Thanks to the tagging crystals, this setup acts as an electronic collimation. Working as trigger for the acquisition, it limits the vertical crystals region in which gamma rays can interact with the module as described in section 4.5.3. The tagging crystal-source distance is set to 6.39 mm while the module-source distance to 2.98 mm resulting in a vertical illuminated region of 1 mm FWHM.

In Fig.5.5, a plot of the (u,v) space is presented showing the signals of the illuminated crystals row. The measurements are performed on the 8x8 LYSO depolished matrix. The idea of starting with the four to one coupling configuration is chosen in order to test DOI capability combined with the crystals separation capability. The same procedure can be applied, without loss of generality

	Central crystals	Edges crystals
4x4 polished matrix	+++	+++
4x4 depolished matrix	+++	+++
8x8 polished matrix	+++	++
8x8 depolished matrix	+++	+
12x12 polished matrix	+++	-
12x12 depolished matrix	+++	-

TABLE 5.1. Crystals separation capability of different coupling configuration.

to each configuration mentioned above. At the end of the section, a comparison of all the modules is shown and discussed.

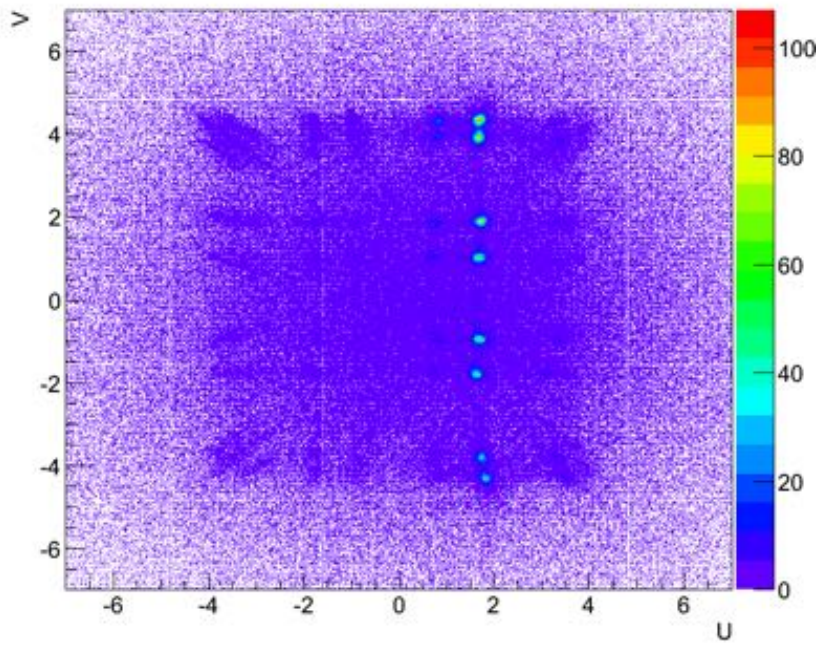

FIGURE 5.5. A typical (u,v) plot obtained by using the electronic collimator setup.

After the acquisition, for each vertical position, an energy selection is applied by selecting photopeak events in the tagging crystal. This ensures that each signal in the matrix crystal is triggered by one 511 keV back-to-back gamma ray. After this first selection, events are separated in corresponding single crystal spectrum according to a (u,v) selection. A photopeak energy

cut is applied in order to recover the second back-to-back gamma ray. For each of these events, the w coordinate is evaluated and its distribution is plotted for each vertical position of the tagging crystal. Comparing different vertical position distribution allows proving that there is a correlation between DOI and w coordinate. The results of a scan on a central crystal is shown in Fig. 5.6 and the w-DOI correlation is verified. The peak of each distribution shifts from lower to higher w value according to the scintillation position of the scintillation. In particular, lower w values correspond to scintillation events in the crystal top region and vice versa.

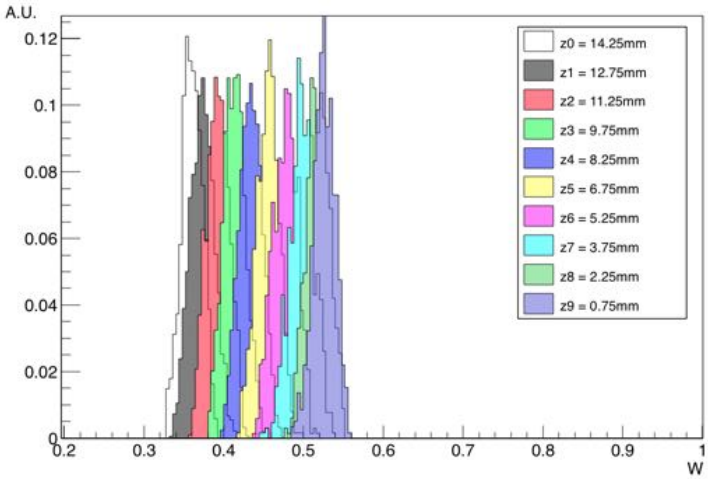

FIGURE 5.6. The w distributions at different vertical position of the tagging crystal.

A gaussian fit is performed for each w distribution plotting the corresponding vertical position of the tagging crystal as function of the peak value as presented in Fig. 5.7.

5.3 Improved crystals separation based on DOI

Proving the correlation between DOI and w coordinate opens the possibility to include this information in the crystals separation procedure. In particular, the collected events can be plotted in the (u,v,w) space instead of (u,v) one. The results are shown in Fig.5.8.
Adding the third coordinate can help in the crystals separation. The idea is that in (u,v,w) space the density regions that were merged in the two dimensional plot can be better separated if a correct procedure is applied. To reach this purpose, a clustering algorithm is developed. This separation procedure works as follow:

- The voxel V_0 that contains the maximum value of entries is found.
- Starting form V_0 the algorithm analyses the nearby voxels.

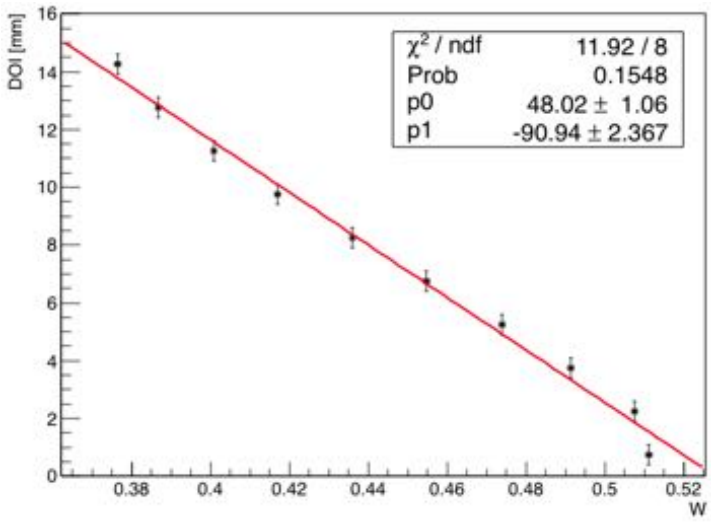

FIGURE 5.7. The DOI as function of the w distribution peak position fitted with a linear function.

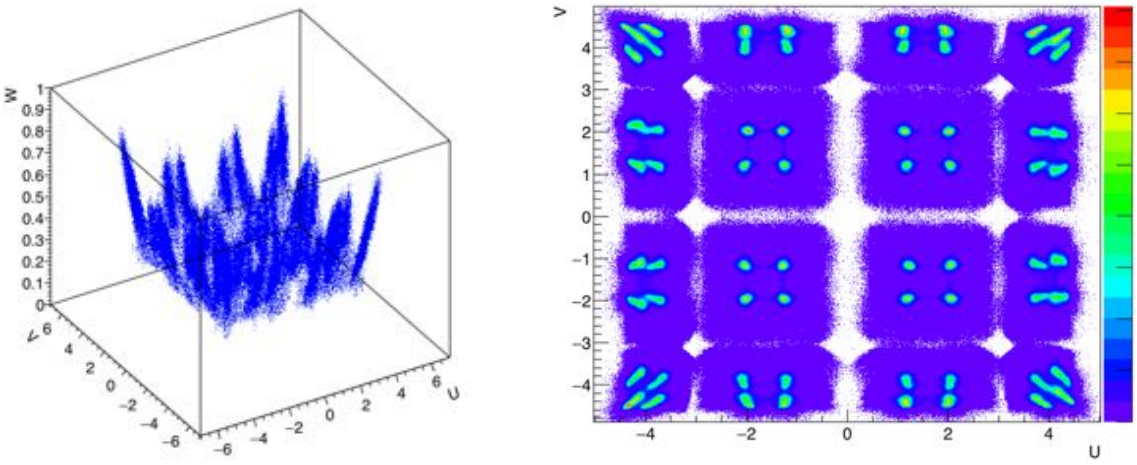

FIGURE 5.8. The collection of events in the (u,v,w) space on the left. On the right, the projection on (u,v) plane.

- If their value is higher than a preset threshold, it is considered as part of the accumulation region otherwise it is discarded.
- When all the voxels in proximity of V_0 are processed and a cluster is identified, these events are removed from the (u,v,w) space and the algorithm starts again from the beginning looking for a new V_0.
- The algorithm is iterated till 64 density regions are found.

To enlighten the functioning of the clustering algorithm, the study is focused on one detector coupled with four crystal as presented in Fig. 5.9. Starting from the entire collection of the events, the four crystals signals are selected by the algorithm identifying four density regions. The threshold of the algorithm is set in a way that the background events are discriminated without rejecting the signal events. The clustering algorithm works perfectly also in the nine to

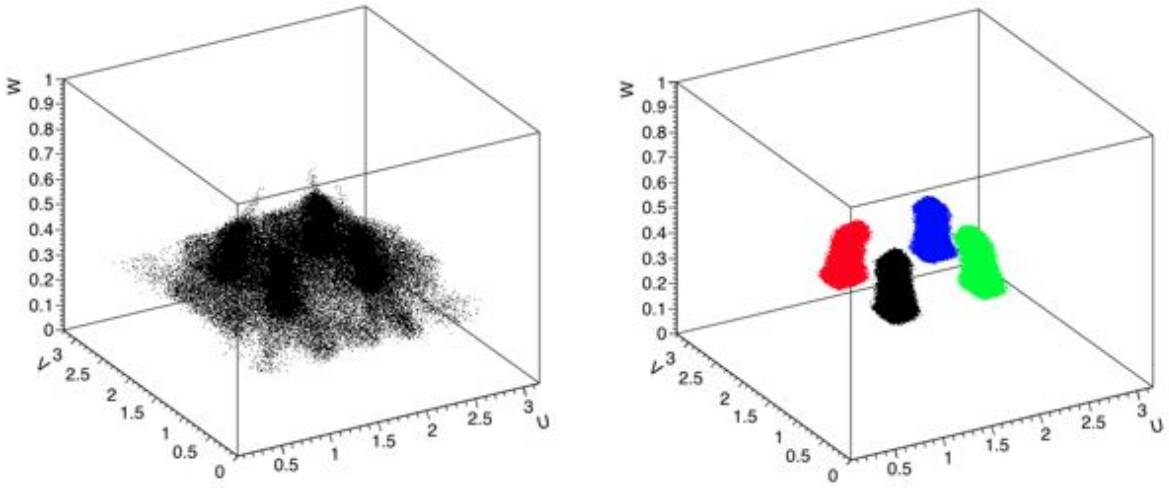

FIGURE 5.9. The result of the clustering algorithm (right) on a raw dataset (left) in the four to one coupling configuration.

one coupling configuration as shown in Fig. 5.10.

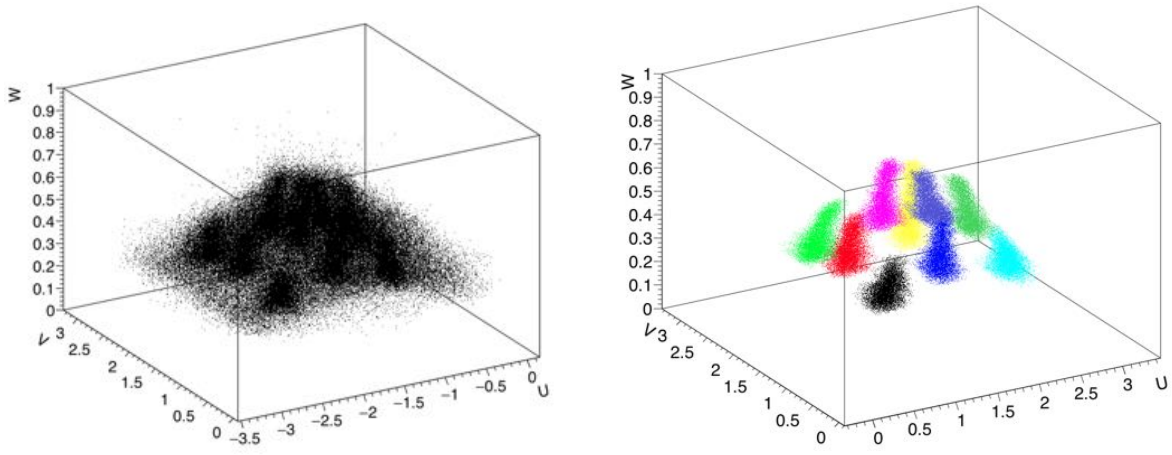

FIGURE 5.10. The result of the clustering algorithm (right) on a raw dataset (left) in the nine to one coupling configuration.

5.4 DOI based energy correction

The optical treatment of crystals lateral surfaces plays a key role in the DOI capability of the system creating an attenuation behavior over the crystal length. Collected light depends on where scintillation takes place and this broadens the energy distribution of the collected events resulting in a worse energy resolution. According to the DOI-w correlation, the energy spectrum can be corrected by including the attenuation behavior as presented in Fig.5.11. In details, if the energy spectrum is plotted as a function of w, a correlation can be established as shown in the left top part of Fig. 5.11. In the photopeak region, a fit slice is performed and the linear equation which describes this w-ADC channel correlation is evaluated. Reversing this equation the w contribution to the energy spectrum is eliminated improving the energy resolution.

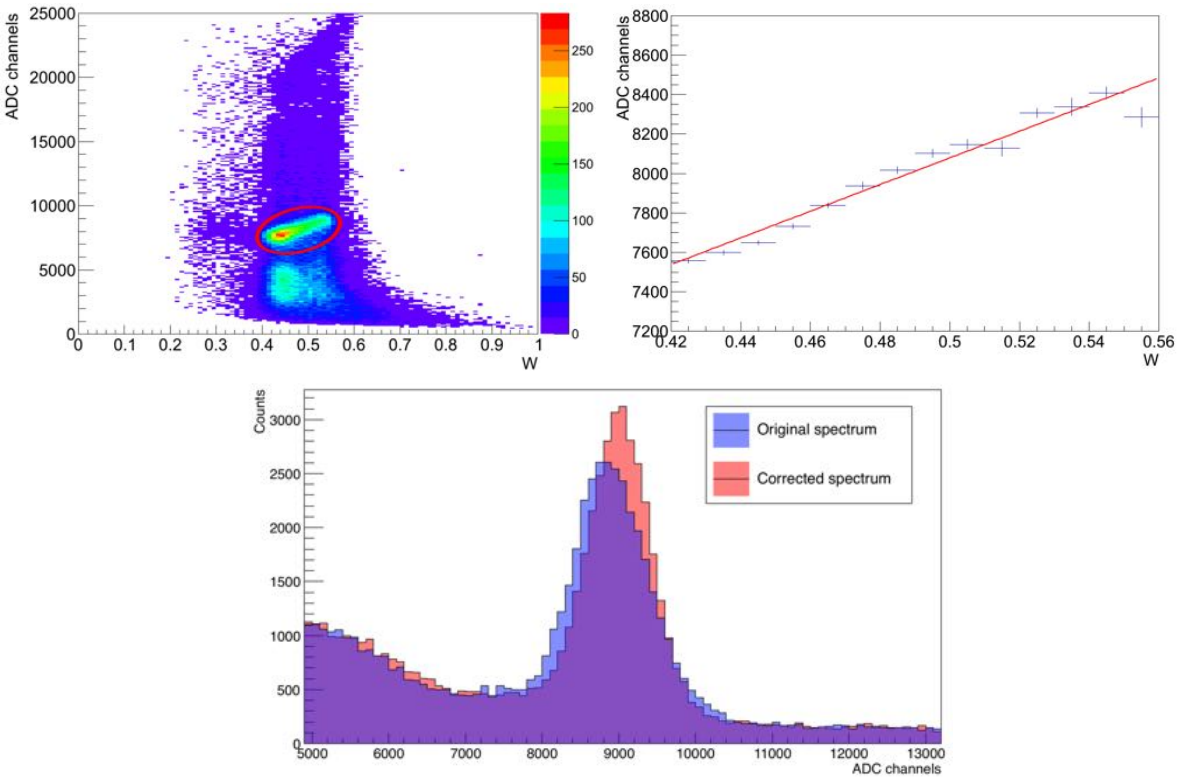

FIGURE 5.11. On the left top figure the dependency of energy spectrum to the w coordinate is enlightened by means of a scatter plot. On the right top figure, the fit slice is shown while the effect of the energy correction is presented in the bottom figure.

5.5 Modules performances evaluation

After demonstrating the DOI improved separation method and energy correction, these procedures are applied to the analysis described in section 5.2 in order to evaluate the performances of the proposed modules. To quantify the DOI resolution, the points of graph 5.7 are fitted with the following equation.

$$DOI = m \times w + q \tag{5.1}$$

Knowing w distributions width (σ_w), it is possible to compute the precision with which the interaction position is reconstructed along the crystal main axis defined as the DOI resolution (σ_{DOI}). This is evaluated by applying the Eq. 5.2.

$$\sigma_{DOI} = m \times \sigma_w \tag{5.2}$$

The average DOI resolution of the entire module is 3.15 ± 0.09 mm FWHM while considering only 16 central crystals it reaches the value of 3.0 ± 0.1 mm FWHM as presented in Fig. 5.12. The discrepancy between central and lateral crystals is expected due to the fact that part of the light which is spread from the hit crystal escapes from the matrix and it is not collected by the detectors at the edges of the module. Again, in a complete PET detector, this non uniformity in DOI performances does not represent an issue. The light that escapes from one unit, it is collected by the nearby ones.

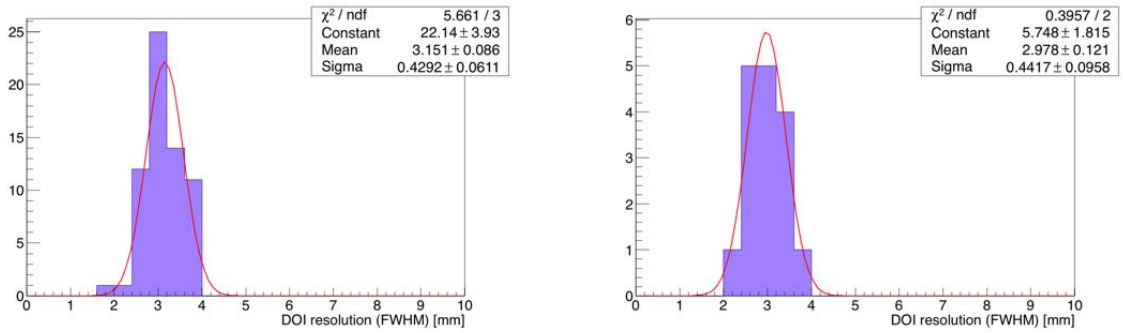

FIGURE 5.12. The DOI resolution distribution for all and for just the central crystals.

After demonstrating the DOI capabilities of the 8x8 crystals matrix, the method generality is proved by measuring the DOI performances of all the possible coupling configurations considering just the central crystals for the previously explained reason. In Table 5.2, the complete performances of the proposed modules are presented.

	4x4 matrix	**8x8 matrix**	**12x12 matrix**
Central crystal identification	+	+	+
Lateral crystal identification	+	+	-
Photopeak position (ADC channels)	(10280±125)	(10300±231)	(7333±351)
Energy resolution (FWHM)	(12.9±0.5)%	(15.2±0.7)%	(25±2)%
Corrected energy resolution (FWHM)	(11.9±0.3)%	(12.5±0.3)%	(15.5±0.7)%
Central DOI resolution (FWHM)	(3.1±0.1) mm	(3.0±0.1) mm	(4.2±0.4) mm

TABLE 5.2. Performances evaluation of the different coupling configurations.

According to the presented results, optical light recirculation in the proposed single side readout allows reaching high performances, in particular, a DOI resolution in the order of 3-4 mm (FWHM) and energy resolution below 16% (FWHM) for all the coupling configurations. The 12x12 matrix shows lower performances due to a lower amount of extracted light. This effect can be caused by the small crystals section. The performances of 4x4 and 8x8 matrices are comparable making these modules suitable for PET devices.

CHAPTER 6

DOI CALIBRATION PROCEDURE

In this chapter, a precise DOI calibration procedure is presented. This procedure is able to recover the w-DOI correlation for each scintillator without an external tagging crystal. This calibration method is suitable for complete assembled PET scanners in hospitals.

6.1 Proposed method

In a fully assembled PET scanner, reaching high performances is the key to achieve high quality metabolic images. Without a proper method to rapidly and periodically calibrate the device, PET examination results will contain misevaluation in the activity and position of tumor lesions.
In the previous chapter, DOI capabilities in the order of 3-4 mm resolution are tested and proved for a single side readout configuration based on light sharing mechanism. This proof of principle is performed thanks to the external tagging setup which provides a priori the scintillation position. By exploited the procedure described in the previous chapter, the correlation functions between DOI and w (Eq. 5.1) are recovered for each module crystal.
However, this calibration procedure is not feasible in a complete assembled scanner because it needs to access the lateral side of each module to be performed. Since gamma rays travel just few centimeters in LYSO crystals before being absorbed this scenario is not feasible unless unpractical disassemblies of the scanner. This is an inconvenient way to proceed and therefore is never performed in hospitals. Even in an unrealistic PET scanner in which the lateral side of modules is accessible, this calibration limit is represented by the time needed to calculate the DOI function for each crystal by means of the external tagging crystals. The calibration of all matrix crystals takes more than 80 hours and this time drastically increases if complete PET devices are considered. Usually, they are made by hundreds, or even thousands, of modules

making this calibration method completely useless in a hospital facility.
Therefore a new calibration method is developed without using external crystals or electronic collimator. This procedure is inspired by the work "A novel method to calibrate DOI function of a PET detector with a dual ended scintillator readout" of Y. Shao, R. Yao and T. Ma [25] in 2008 in which the authors developed a method to extract the DOI calibration function in a double side readout exploiting an uniform irradiation of the scintillators as shown in Fig. 6.2.

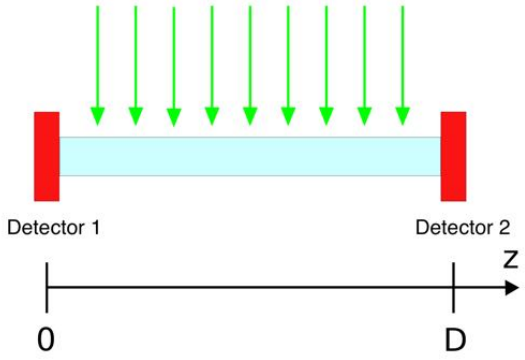

FIGURE 6.1. The double side readout used by Y. Shao, R. Yao and T. Ma.

In double side readout, defining s_1 as the light collected by the detector 1 and s_2 as the light collected by the second detector, DOI information is provided by the asymmetry R of the collected light. It can be described as follow.

$$R = \frac{s_2}{s_1 + s_2} \tag{6.1}$$

If there is no dispersion in detectors response, each interaction position z corresponds to one and one only R value. This biunique correspondence is expressed, without generality losses, by Eq. 6.2

$$\int_0^z P(z)dz = \int_0^R PDF(R)dR \tag{6.2}$$

$P(z)$ represents the probability that an incoming gamma ray interacts at the z position in the crystal. $PDF(R)$ is the probability density function that a scintillation event occurring at position z will arise a collected light asymmetry equal to R. It is worth noting that if $P(z)$ is uniform, the equation can be simplified as follow, where D is the length of the crystal.

$$z = D\int_0^R PDF(R)dR \tag{6.3}$$

$PDF(R)$ is derived by the normalized distribution $H(R)$ of the coordinate which provides DOI

information.
In this method, DOI calibration functions are obtained by Eq. 6.3 performing just one uniform irradiation of the crystal and evaluating the normalized distribution of R variable.
This procedure can be applied to the single side readout configuration proposed in this study by replacing the R variable with the w coordinate [26]. The idea is to compare the results of this calibration method with the outcome of the electronic collimator setup
To be able to derive Eq. 6.2 from Eq. 6.3, an uniform irradiation of the crystal along the main axis is needed. The natural choice is to illuminate the module from one side using a radioactive source. Having a planar source would be the best solution but also a point source kept to a distance much larger than the dimension of the crystal can ensure a uniform irradiation. This irradiation modality has the same issues of accessing the later crystals side but this approach is investigated as a comparison with the irradiation procedure presented by Y. Shao, R. Yao and T. Ma. Another interesting possibility it is to exploit ^{176}Lu internal radioactivity. Lutetium emits electrons up to an energy of 401 keV, which interact in the crystal originating three gamma rays (88 keV, 202 keV and 307 keV). This irradiation is uniform along the scintillator main axis.

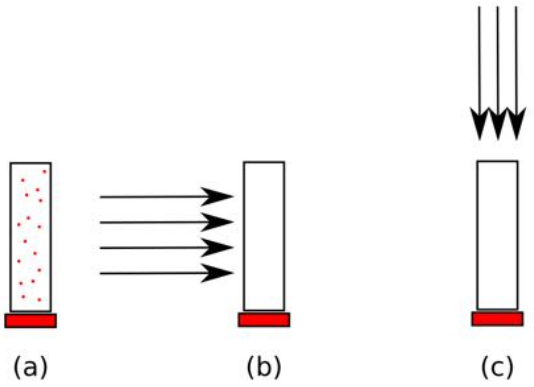

FIGURE 6.2. The three irradiation modalities: on the left, the ^{176}Lu background irradiation, in the center the lateral irradiation and on the right the irradiation from the top of the crystal.

A third modality is an irradiation from the top of the matrix. A calibration procedure, that relies on this irradiation way, is feasible in hospitals. It can be performed by placing a radioactive source in the FOV and selecting, through a coincidence system, gamma rays parallel to the scintillator main axis. This method does not provide an uniform irradiation along the main axis of the scintillator but the attenuation behavior of the scintillator crystal is a well known mechanism. Therefore a correction can be applied. Even if the radiation it is not uniform, Eq. 6.2 is still true while the mathematical passage from this equation to Eq. 6.3 can not be applied anymore. In this configuration $P(z)$ is not constant but it follows the scintillator attenuation behavior that can be

expressed as follow:

$$P(z) \sim e^{-\frac{D-z}{\lambda}} \tag{6.4}$$

where λ is the attenuation length for 511 keV in LYSO crystal. Using boundary conditions, the $P(z)$ can be written as:

$$P(z) = \frac{1}{\lambda(1-e^{D/\lambda})} e^{-\frac{D-z}{\lambda}} \tag{6.5}$$

Including this expression in Eq. 6.2, the final result is summarized in Eq. 6.6

$$z = D + \lambda \ln\left[1-(1-e^{-\frac{D}{\lambda}})\int_0^w PDF(w)dw\right] \tag{6.6}$$

Thanks to the result expressed in Eq. 6.6, radiation coming from the top of the module can be exploited for DOI calibration adding generality to the method proposed by Y. Shao, R. Yao and T. Ma.

6.2 DOI calibration results

In this section, the performances of each proposed calibration method are tested and compared with the ones obtained in the previous chapter by using the external tagging crystal. The different acquisitions configuration are presented in Fig. 6.3.
The acquisition system is the same exploited in PET-like setup. In fact, the acquisition trigger is provided internally in each calibration configuration. Every time that a signal in one channel is above a programmable threshold, all the channels are acquired in parallel. The crystals signals are separated by means of the clustering algorithm. After applying a photopeak energy selection, the w distribution is plotted for each crystal as presented in the left part of Fig. 6.4. For the ^{176}Lu internal radioactivity the energy selection is not applied due to the fact that there is no photopeak.
According to the calibration method previously discussed, normalizing the w distribution returns the $P(z)$. The last step to obtain DOI calibration functions is to perform the distribution integral by applying Eq. 6.3 for background and lateral irradiation and by Eq. 6.6 for top irradiation. In Fig. 6.4 (right) a DOI function is shown for a single crystal and it establishes the z-w correlation. Knowing the w value allows recovering the interaction position along the crystal main axis.
As presented in Fig. 6.5, comparing the results of the three different calibration modalities with the ones achieved by the external tagging setup confirms calibrations method validity and precision. It is possible to quantify the precision of each method by computing the discrepancy Δ defined as follow:

$$\Delta = z_{collimation} - z_{calibration} \tag{6.7}$$

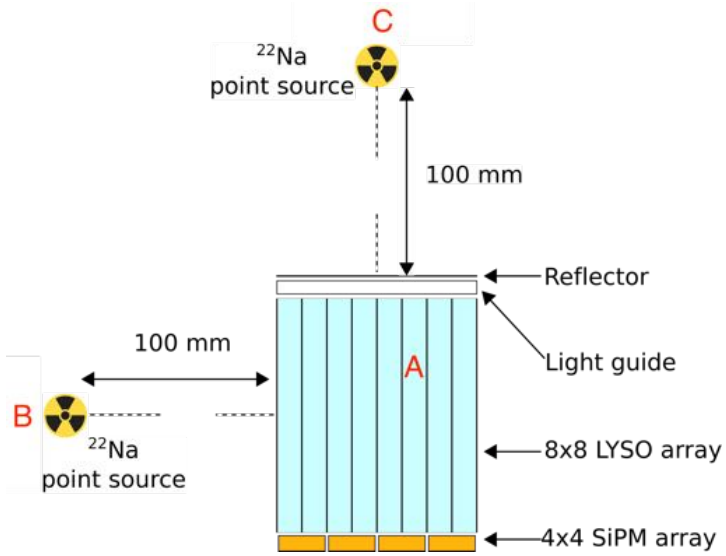

FIGURE 6.3. The calibration setups: A with lutetium radioactivity, B with the radioactive source 10 cm laterally placed and C with the radioactive source placed 10 cm above the module.

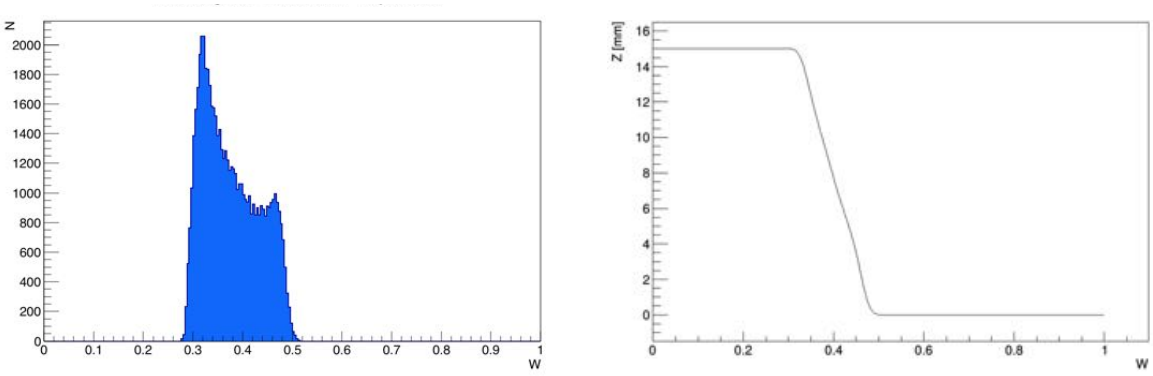

FIGURE 6.4. On the left, the w distribution for one central crystal. On the right the DOI calibration function.

where $z_{collimation}$ is the interaction position reconstructed by the external tagging method, while $z_{calibration}$ is the DOI computed by exploiting the proposed calibration methods. The distribution of Δ for all crystals and for the central ones are presented in Fig. 6.6.

For the same reason discussed in the previous chapter, the calibration accuracy evaluation is restricted only to central crystals. The results of Δ distribution RMS and mean value are summarized in the table below.

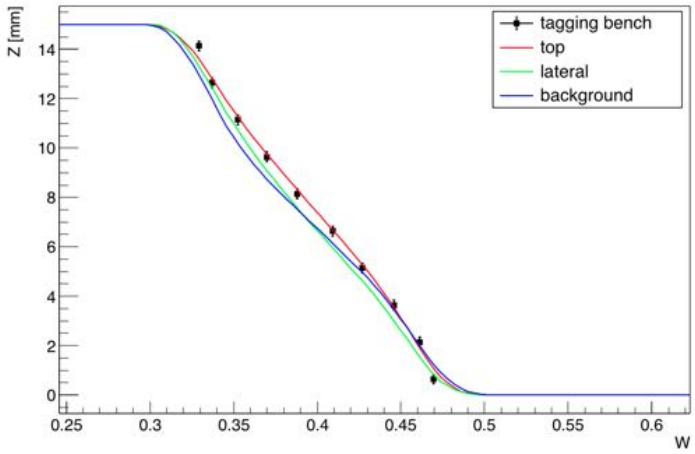

FIGURE 6.5. The comparison between the results obtained by the three different calibration modalities and the outcome of the electronic collimator setup.

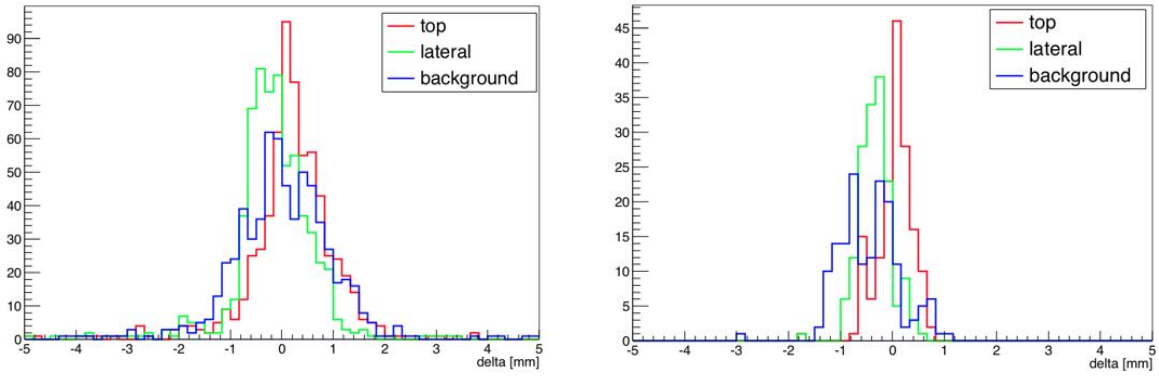

FIGURE 6.6. The Δ distributions for all the crystals (on the left) and for the central ones (on the right) for each calibration modality.

All the calibrations work properly being able to reconstruct DOI information with good agreement with results achieved with the electronic collimator calibration. Both offset and RMS of each calibration procedure are below 1 mm demonstrating their feasibility and correctness. The best calibration procedure is the one which exploits the top irradiation. It is also the most suitable methodology to be performed in a hospital facility to periodically calibrate in a fast and precise way a completely assembled PET scanner. Also the lutetium radioactivity calibration is promising but it does not provide the energy calibration of the system. As already discussed the lateral irradiation is not feasible in a complete assembled detector.
Another important outcome concerns the overcoming of w-DOI linear relation introduced in Eq. 5.1 to quantify the DOI resolution. Describing this correlation by a simple equation is a

	Average [mm]	RMS [mm]
4x4 crystals matrix		
Lateral irradiation	-0.20	0.55
Internal radioactivity irradiation	0.28	0.50
Top irradiation	0.36	0.45
8x8 crystals matrix		
Lateral irradiation	-0.33	0.32
Internal radioactivity irradiation	-0.45	0.57
Top irradiation	0.04	0.35
12x12 crystals matrix		
Lateral irradiation	-0.04	0.45
Internal radioactivity irradiation	-0.40	0.47
Top irradiation	0.61	0.45

TABLE 6.1. The evaluation of the DOI calibrations performances. The average and RMS of the Δ distribution of each calibration procedure is presented.

first approximation but, in particular at crystal edges, the linear behavior is lost leading to DOI miscalculations. By using the Eq. 6.3 or Eq. 6.6, the w-DOI correlation is better described without any parameterization or assumptions.

CHAPTER 7

TIMING PERFORMANCES MEASUREMENTS

In this chapter, the timing performances of the proposed modules are tested. In particular, the method to include DOI information in the interaction time evaluation is presented at the end of the chapter.

7.1 CTR evaluation

For the CTR performances evaluation, the timing setup presented in section 4.5.4 is used. Due to electronic readout constraints and the unfeasibility of an energy linearization method of the NINO chip, it is not possible to separate the crystals by using the light sharing mechanism. The signal of all the crystals coupled to the same MPPC is considered as one single crystal signal. The tested module is the 8x8 LYSO matrix. The source and the reference crystal are then aligned on the same direction of one MPPC detector of the module. The first step of the timing performances evaluation is to select the photopeak events in both reference crystal and module. This ensures that only back-to-back gamma rays are considered in the analysis.
Due to TOT nature of this acquisition system, energy response is not linear as previously mentioned. A linearization process was investigated but the results pointed out a lack of precision in the evaluation of energy linearity. This linearization approach shows no clear benefits and it is not feasible. In any case, in the photopeak region, the non linearity of the acquisition chain is not strong. This allows to identify and select the 511 keV gamma ray interactions as reported in Fig. 7.1. After the selection of the 511 keV events in both components, for each event the detection time difference between reference crystal and module is computed giving the first evaluation of the timing performances. In Fig. 7.2, the time difference distribution is plotted and fitted by a gaussian function. The σ of the distribution is 148 ps resulting in a CTR of 348 ps FWHM.

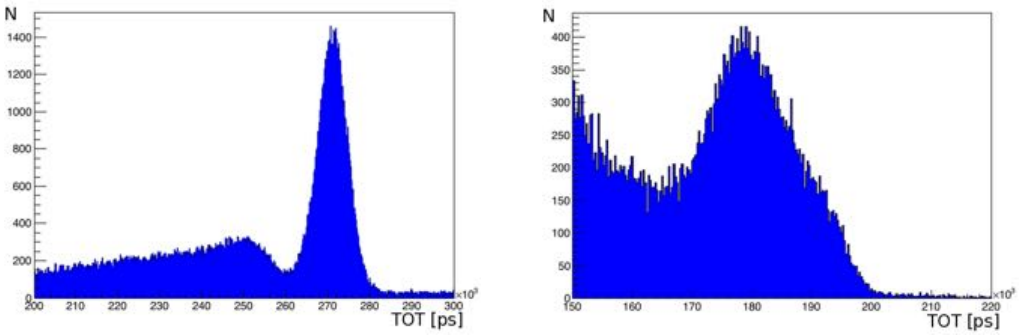

FIGURE 7.1. Photopeak events for reference crystal (left) and module (right).

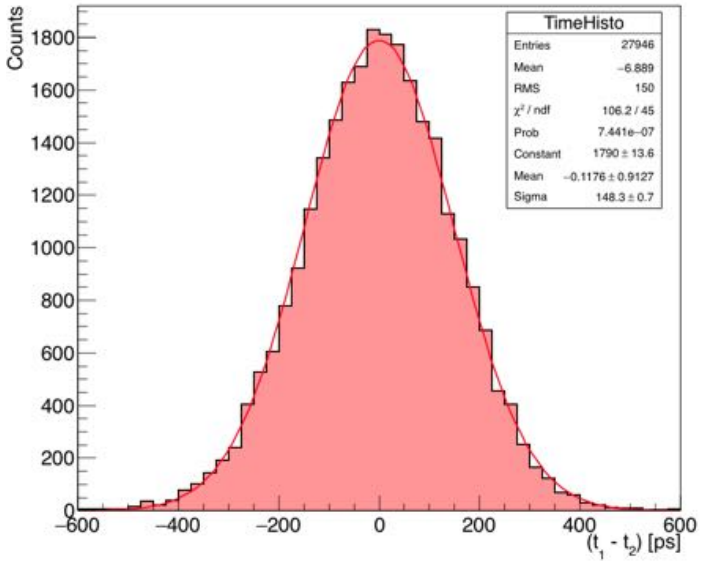

FIGURE 7.2. The detection time distribution.

This result is achieved by using a system based on two components (reference crystal and module) with different timing properties. In order to quantify the CTR of a complete detector composed entirely by modules, it is important to decouple the contribution of the reference crystal from the time performances evaluation. The same measurement described above is repeated by using two identical reference crystals resulting in a CTR of 219 FWHM ps. The timing performances contribution of the single crystals is obtained by the following equation.

$$STR_{single\ reference\ crystal} = \frac{CTR_{total}}{\sqrt{2}} \tag{7.1}$$

The result shows a single crystal contribution of 155 ps FWHM. If this contribution is decoupled from the previous CTR value of 348 ps, the contribution of the individual module is obtained. If it is multiplied by $\sqrt{2}$, returns the CTR of 436 ps FWHM which represents the time performance of a

system made entirely by the proposed module read out by an electronic chain based on NINO chip.

$$CTR_{system\ of\ modules} = \sqrt{2} \times \sqrt{\left(CTR^2_{measured} - STR^2_{single\ reference\ crystal}\right)} \tag{7.2}$$

The result is compared to the one achieved by a module with same configuration but polished lateral surfaces. The measurement procedure replicates the method previously described and the polished module shows a CTR of 321 ps FWHM. The results are consistently far between each other and the reason has to be found in Eq. 4.1 as already discussed. The lateral surfaces depolishing degrades the timing performances.

7.2 DOI corrected CTR

In section 4.3, a method to correct for the DOI dependent time jitter of optical photons is presented. This method is tested by using a simulation approach in GEANT4 before being applied to the experimental measurements. A depolished module with one to one coupling configuration between scintillators and detector is built in GEANT4. In particular, the MPPC detector consists in a layer of silicon with on top a thin layer of epoxy replicating the interface window. 511 keV gamma rays are shot perpendicularly to one crystal. The emission time represents the simulation reference time. When incoming gamma rays interact with LYSO, optical photons are generated according to the properties of the scintillating material and they spread isotropically in crystals. Optical photons that release their energy in the silicon layer are considered detected and their properties are stored in a file to be analyzed. The simulation does not include the electronic chain and so the obtained results have to be considered just for a comparison between the corrected and not corrected timing performances.
For each photoelectric event in the selected crystal, the time distribution for detector directly coupled and the nearby ones is plotted as presented in Fig. 7.3. The timing distribution of optical photon is obtained as the difference between optical photon detection time and gamma rays emission time.
As in Fig. 7.4, if these distributions are scatter plotted as a function of the DOI information, it possible to observe that DOI plays a role in the timing distribution not only in the hit crystal but also in the nearby ones. This allows evaluating the arrival delays $\delta_i(DOI)$ for each crystal.
The $\delta_i(DOI)$ are evaluated by performing a fit slice on the scatter distributions. A linear relation between arrival time and DOI is established opening the possibility to compute the corrected interaction time $\hat{t}$.
Two possible corrections are considered according to available channels number. The first one corrects the arrival time by considering only the hit crystal contribution. In the Eq. 4.7 i is equal to one and it corresponds to the signal from the single crystal considered. The detection time distribution is less broaden by applying this correction. Even more interesting it is the correction which involves all the nearby detectors. The time distribution width is further reduced. The

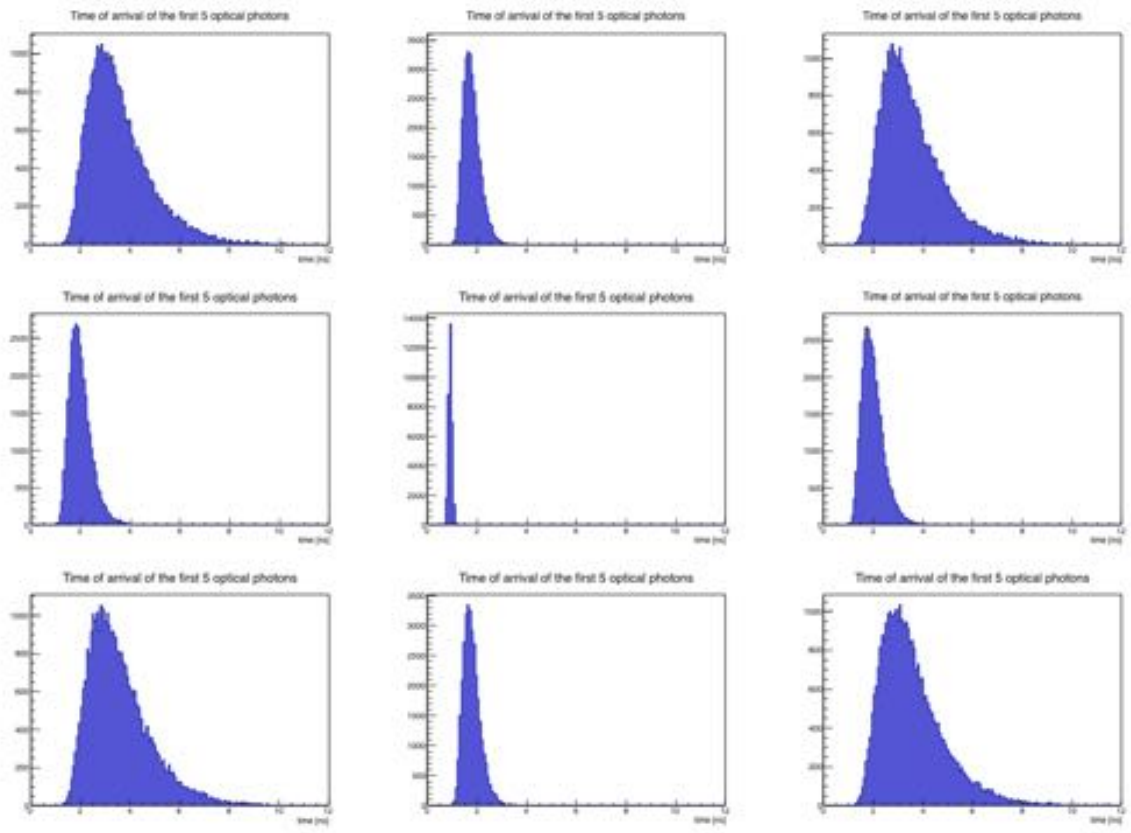

FIGURE 7.3. The arrival time distribution of the nine crystals considered in the simulation. The central crystal is the one where the incoming gamma interacts while the eight nearby ones represent the time distribution of the shared light.

results are shown in Fig. 7.5 (left). The CTR is evaluated for each correction and different crystal lengths are simulated and tested in order to verify the procedure generality. The results are shown in Fig. 7.5 (right) for 15mm, 20 mm, 25 mm and 30 mm length. Again, these CTR results do not include any contributions from electronic chain and acquisition system noise. The evidence which arises from this simulation study is that timing performances are improved by evaluating the DOI related delays. The DOI capability does not represent a limit in the timing performance of a PET module if the DOI information is exploited to correct the detection time distribution of the optical photon. Furthermore, the best result is obtained while the information of the shared light is included in the timing correction supporting the idea that the light sharing mechanism can be exploited to better estimate the interaction time of the gamma ray in a PET module.
However, it is worth to remember that by using the experimental equipment described before, it is not possible to collect the information about the energy of the shared light. The reason has to be found in TOT technique exploited by NINO chip to access the energy and timing

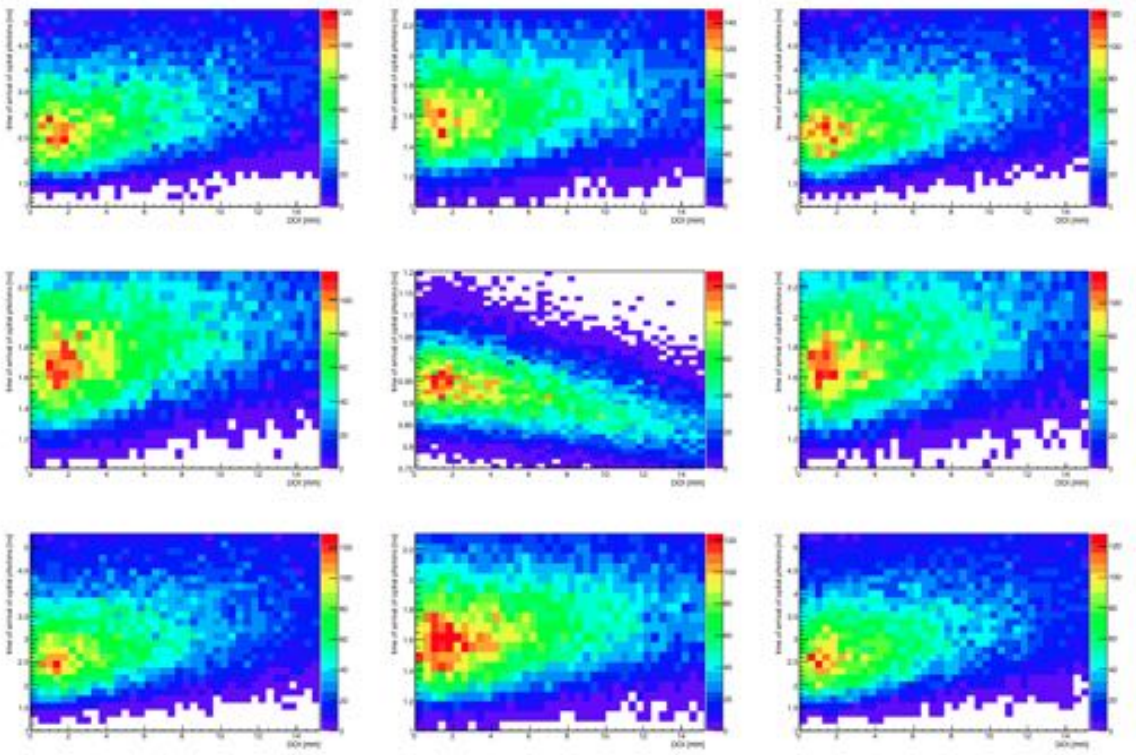

FIGURE 7.4. The dependency of the detection time distribution from the DOI for the nine crystals considered in the simulation. This correlation takes place not only in the crystal directly hit by the incoming gamma ray but also in the nearby ones underlining the DOI dependency of the shared light.

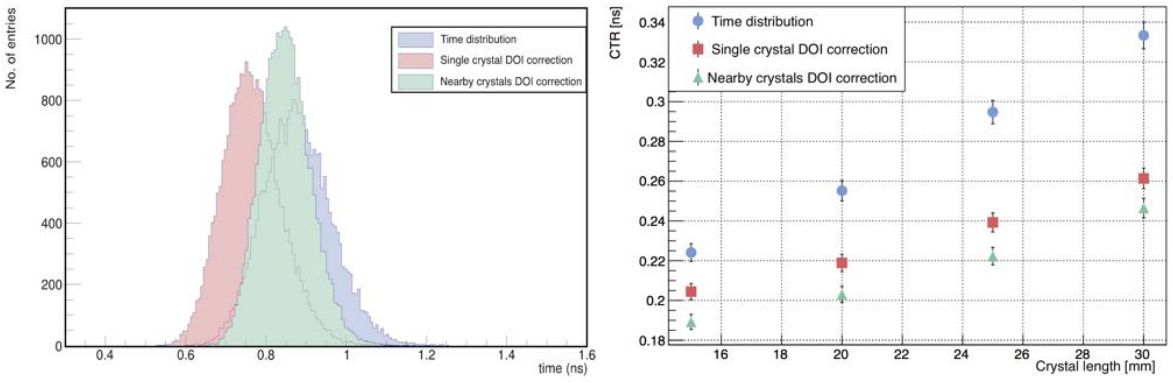

FIGURE 7.5. (Right) The comparison between the uncorrected and corrected arrival time distributions. (Left) Comparison between different corrections as function of crystal length.

information. As already mentioned, in this procedure TOT information does not scale linearly with incoming gamma energy. This study relies on light sharing mechanism and this represents a limit unless a linearization procedure is applied. In details, the majority of the scintillation light generated by gamma ray interaction is collected by the detector directly coupled. The remain optical photons are spread in the nearby scintillators. The information about total deposited energy is recovered by summing the different contribution in the detectors. This procedure leads to an energy misevaluation if the electronic response is not linear. In other words, the fraction of optical photons shared in the nearby detectors arises a smaller TOT signal compared to the one collected in the directly coupled crystal. They can not be summed together without a linear relation between the energy and the TOT. This effect excludes also the possibility to evaluate the w coordinate that by definition involves the energy deposited in all the nearby detectors. TOT signal of the hit crystal is the only indicator of the DOI dependent different light output along the scintillator main axis.

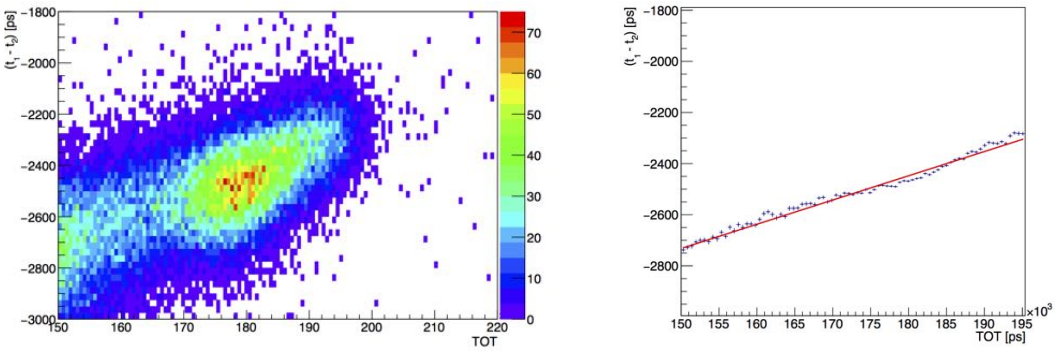

FIGURE 7.6. The scatter plot of the time distribution as a function of the TOT and the linear fit on the graph of the slice means.

The procedure of single crystal time correction is applied to measured data, as shown in Fig 7.7, starting by scatter plotting the time distribution as a function of the TOT. The dependency between the two variables is clear and can be corrected by performing a linear fit on the graph that reports the mean value of each slice of the scatter plot.
If the timing performance of the external tagging crystal is decoupled, a CTR of 353 ps is reached. Compared to polished module results, it differs for 30 ps. It is worth to remember that this correction takes into account only the contribution of a single crystal. Simulation results show that including also the contribution of the shared light the obtained result can be further improved with an appropriate readout system able to manage and collect the light sharing signal with a linear energy response.
Future research studies will be based on an acquisition chain which keeps separated energy and time information. This procedure is based on a split of the detector pulse. A digitizer will performe the integration of the signal in order to access to the DOI information by evaluating

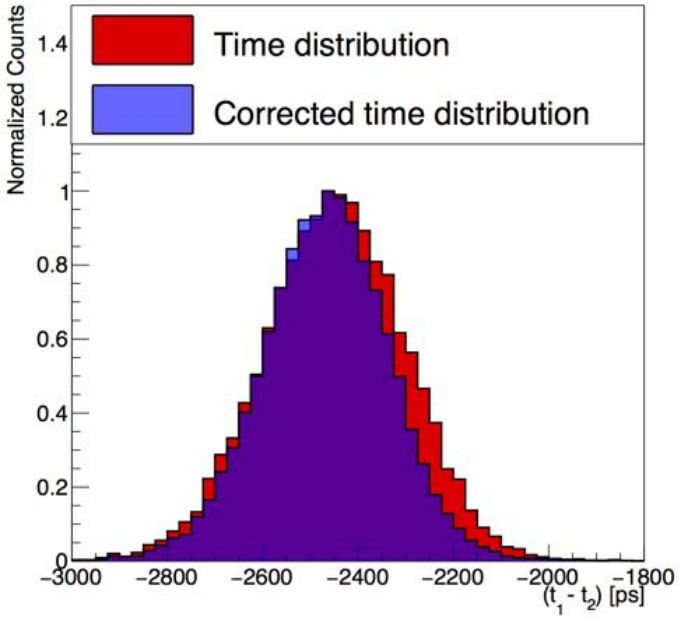

FIGURE 7.7. The improvement of the CTR in the uncorrected and corrected arrival time distributions.

the w coordinate. The timing information will be instead provided by a NINO chip coupled to a timing digitizer. The purpose is to collect the information in order to be able to exploit the shared light in the DOI based CTR correction.

CHAPTER 8

IMAGE RECONSTRUCTION STUDIES

In this chapter, an image reconstruction study is presented based on GATE simulation. In particular the effect of normalization process and the benefit of DOI information are discussed. At the end of the chapter, a TOFPET approach is studied to evaluate the improvement in image quality for different timing performances.

8.1 Gate simulation

To be able to control all the physics processes and detection mechanism, the best procedure is to adopt a simulation approach. An useful tool is GATE. The OpenGATE collaboration developed this opensource software in order to create a numerical simulation tool dedicated to medical imaging and radiotherapy applications. It was presented in 2004 by S. Jan *et al* in the work "GATE: a simulation toolkit for PET and SPECT" [27]. Without going into details, GATE consists in a multilayer structure with two developed layers, core and application ones, and an user layer on top of them. A scheme of the software architecture is shown in Fig. 8.1. The developer layers are implemented in C++ and they include some Geant4 mandatory classes for geometry construction, physics mechanisms, visualization and event generation. In user layer, commands to run simulations are provided by Geant4. Each class has a proper command interpreter class to make this software available also for the endusers without the C++ knowledge.
One of the advantages of using GATE is the possibility to describe the electronic chain by defining the parameter of the digitizer module. The software takes care of acquisition processes performing blurring on data to match the desirable energy resolution. It is able to collect events as set of coincidences according to the chosen time window. The output of a GATE simulation is the coincidence events collection. For each of them the information about deposited energy, detection

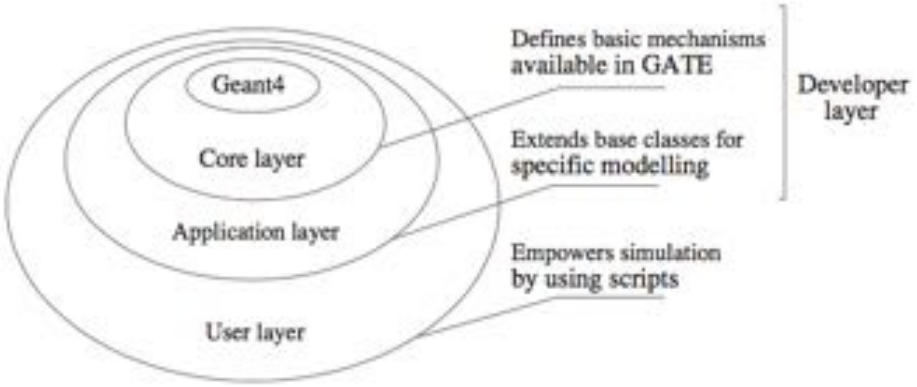

FIGURE 8.1. Scheme of the GATE software architecture (picture from S. Jan *et al* in the work "GATE: a simulation toolkit for PET and SPECT").

time and interaction point position of gamma rays are provided.
In order to test a small animal or an organ dedicated PET system, the 8x8 LYSO module is built in GATE. According to measured performances (spatial, DOI, energy and time resolution), this 8x8 module is the most suitable for this applications.
Crystals are the only active area in the simulation. This means that the scintillators are the only regions where energy deposition is possible. If this happens, the events are recorded. In addition, also the plastic holder and the glass light guide are simulated in order to reproduce a more realistic system. For the same reason also the MPPC array is included in the simulation system even if it does not perform directly the collection of the light. Due to the fact that the optical component of the scintillation mechanism is not included in this GATE simulation, the MPPC is not meant to convert the optical light into a voltage pulse. It just represents a mean with which the gamma ray can scatter. In details, the MPPC array is simulated by a thin layer of silicon with a glass window on top according to the dimension provided by Hamamatsu. In Fig. 8.2, it is possible to appreciate the geometry of the simulated module. In particular in yellow the LYSO, in magenta the plastic holder, in blue the glass component, in grey the silicon and in red the ESR on top of the light guide.
The simulated PET system consists in a single ring of modules. The single module is duplicated 60 times in order to cover a circumference of 125 mm radius. This is a typical dimension for a PET detector that targets the diagnosis of breast or brain lesions. To summarize the simulation configuration, there are 60 modules with 64 crystals each for a total of 3840 scintillators. Each module has 8 crystals along the vertical directions and therefore the entire system can be considered an eight detectors rings PET scanner.
Digitizer parameters are set to match the proposed module performances and in particular an energy resolution of 12%. The coincidence window is evaluated according to FOV dimension and

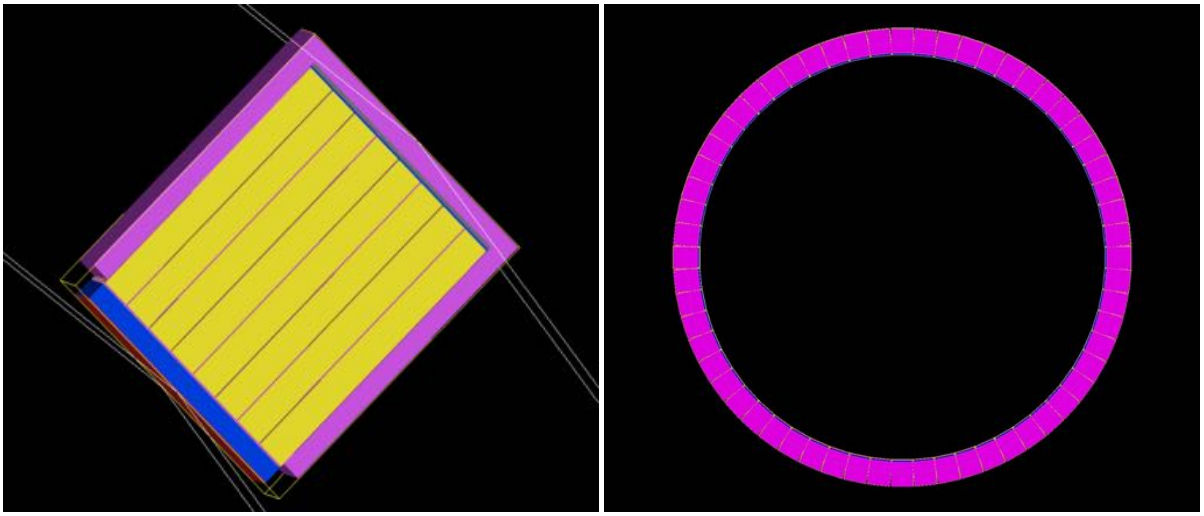

FIGURE 8.2. The simulated PET system. On the left part, the section of a single module. On the right part the complete ring geometry.

set to 6 ns. Dead time is ignored affecting only system sensitivity which is not considered in this study. Sources with different geometry are exploited according to the feature which needs to be evaluated. In order to exclude the effect of positron range, sources consist in back-to-back emissions of two 511 keV gamma rays. In addition, the entire simulation takes place in the vacuum avoiding the scatter and the attenuation effect simplifying the reconstruction processes. Scatter and attenuation corrections are planned to be developed in a future study.

8.2 Normalization process

As explained in the previous chapter, ClearPEM reconstruction algorithm is meant for a dual plates system which rotate concurrently around the FOV. During the acquisition, the relative position of gamma rays interaction and the two plates orientation are recorded in a list-mode file. The information is elaborated by the algorithm in order to calculate the interactions absolute position in (x, y, z) space. To obtain a better coverage of the FOV avoiding rotations and develop a more efficient simulation, a complete ring geometry is chosen. The reconstruction method works exactly in the same way as the dual plates geometry if the rotation angle is always fixed and the information recorded in list-mode file is the absolute (x, y, z) position.
The first test is to observe the normalization mechanism which mitigates the non uniform sensitivity of the FOV. It is worth to notice that in this step the TOF is not included in the reconstruction because it will be largely discussed later in this chapter. The first simulation consists in an acquisition of a uniform cylindrical source with a radius of 55 mm. The source covers the totality of crystals along the axial direction.
Due to the dual plates geometry, the ClearPEM normalization is performed by a long acquisition of

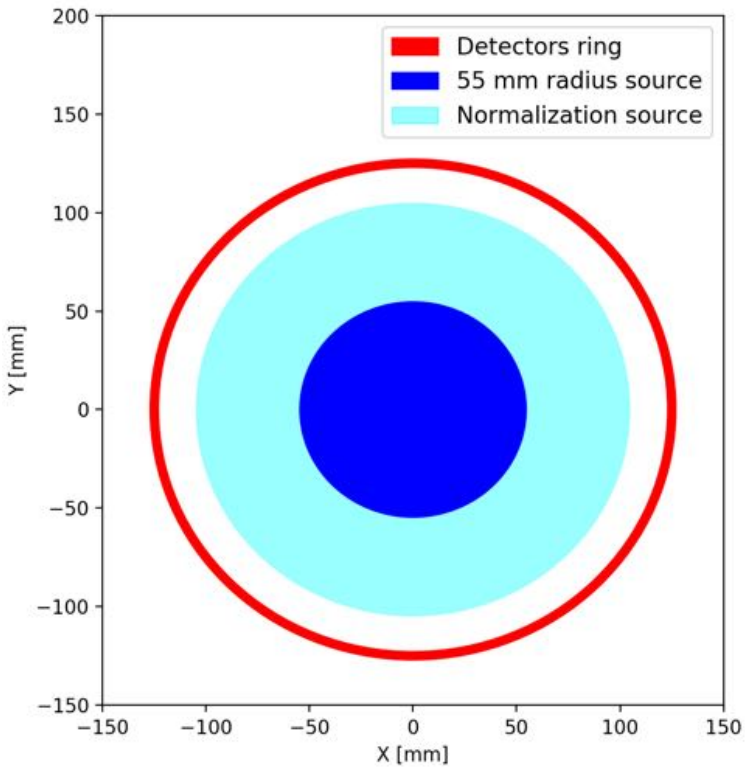

FIGURE 8.3. Positioning of the sources in the GATE simulation.

a planar source placed in between the two modules plates at fixed orientation. This measurement is able to take into account the different sensitivities of all detectors and correct the reconstructed image in order to have a uniform response to the same activity in each position of the FOV. In the proposed ring configuration there are no rotations and a uniform cylindrical source has to be simulated to achieve the same uniform response. This normalization source covers almost the entire FOV and it has a radius of 105 mm. Clearly, the FOV region where sensitivity is uniform is restricted to the area included by the normalization source. Therefore sources or phantoms have to be contained in a cylinder with these dimensions in order to be correctly reconstructed. In Fig. 8.3 it is possible to appreciate dimensions and position of simulated sources.
The simulation results are shown in Fig. 8.4 where a comparison between non normalized and normalized images is presented. In the non normalized image, it is possible to identify artifacts and spikes due to position dependent sensitivity. In the normalized image, these effects are mitigated and an uniform activity is detected from the 55 mm radius source.
As previously mentioned, in the iterative algorithms the signal increases according to the number of iterations till a saturation plateau while the noise continues to increases linearly. It is possible to evaluate the optimal number of iterations to be performed in order to obtain the best

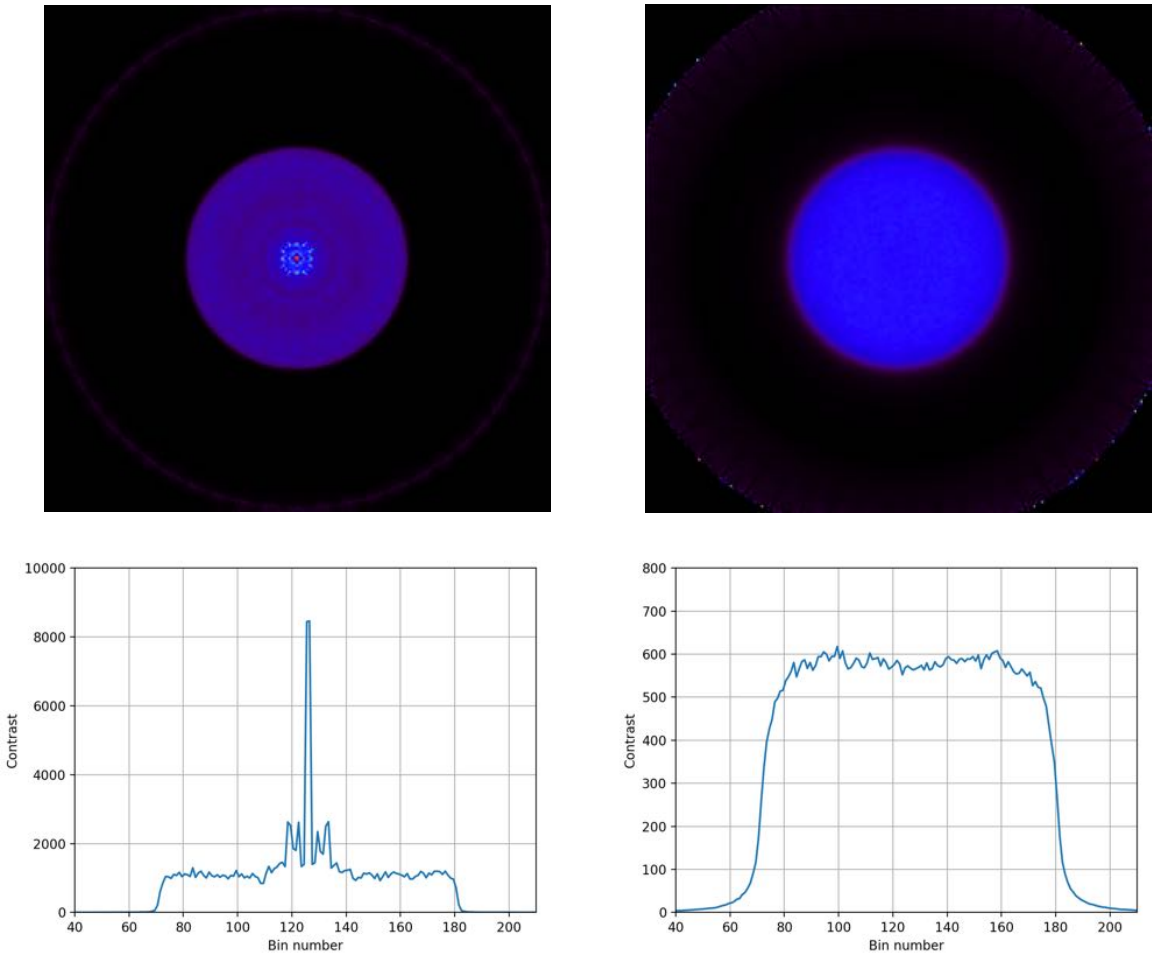

FIGURE 8.4. Comparison between the non normalized and normalized images. In the top part the reconstructed images (non normalized on the left, normalized on the right) and in the lower part the relative profiles.

reconstructed image. This optimal number is the lower iteration in which the signal starts to reach a stable value and the noise is as low as possible.
In normalized image presented in Fig. 8.4, the signal is evaluated by measuring the contrast mean value in a cylindrical region of interest (ROI) contained in the source volume. Noise value is provided by the mean standard deviation. It is possible to observe that the 7^{th} iteration appears to be the best value where the reconstruction process can be stopped. The signal is saturating and the standard deviation is still low.

8.3 Parallax error evaluation on reconstructed images

Before going into the details of DOI information benefits in the reconstructed images, it worth to present the correct procedure to determine the gamma interaction point. GATE simulation

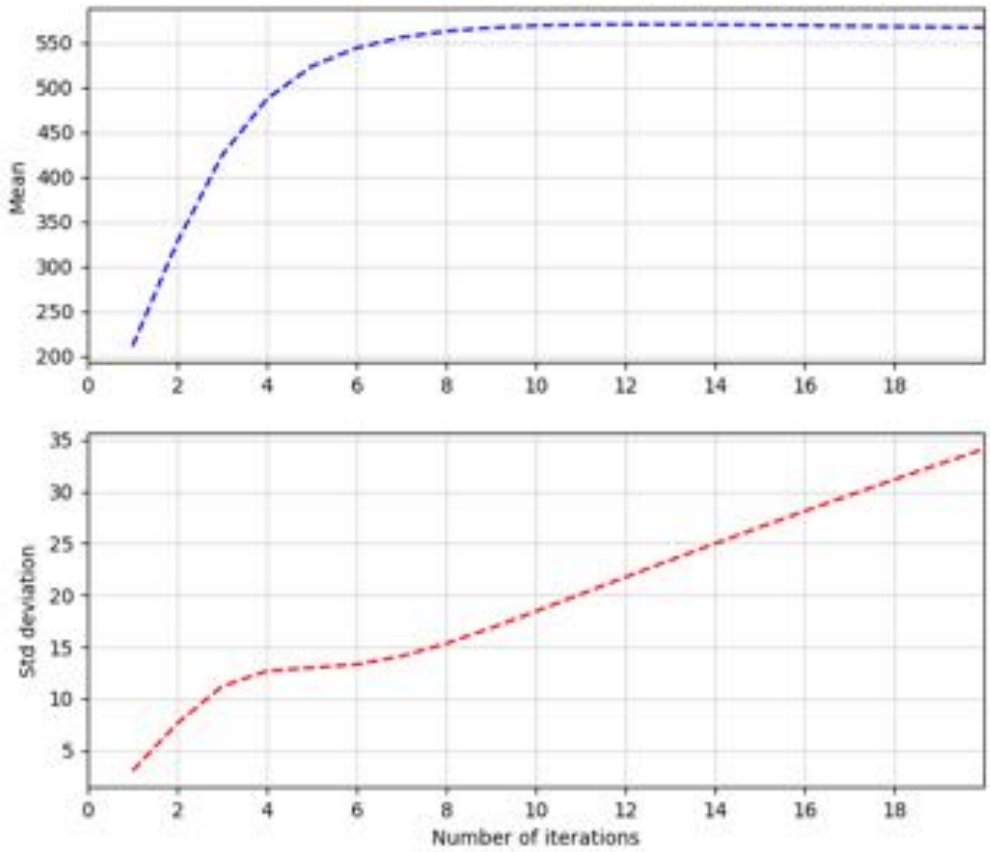

FIGURE 8.5. Mean value and standard deviation as function of the iteration number.

returns the exact (x, y, z) interaction point but it is not realistic to use this information as the input of the reconstruction algorithm. As already discussed, in PET devices based on pixelated modules the interaction position is recovered by identifying the hit crystal and, if it is available, the DOI information. The identification uncertainty is determined by the system performances. GATE simulation output is re-elaborated in order to move the detected events in each crystal on its main axis. A C++ code is developed to fulfill this operation by giving the possibility to simulate different DOI resolutions and to evaluate their impact on reconstructed image quality. DOI uncertainty is obtained by a gaussian smearing of the position with a sigma σ that corresponds to the system DOI resolution.

To test the reduction of the parallax error effect by introducing DOI information, several point sources with a diameter of 1 mm are simulated. They are arranged in a line which covers a large FOV portion separated by 5 mm as presented in Fig. 8.6. To ensure a correct reconstruction, all the sources are contained into the normalization source volume. Three DOI resolutions are simulated. The first one is the usual method to handle the data when no DOI information is

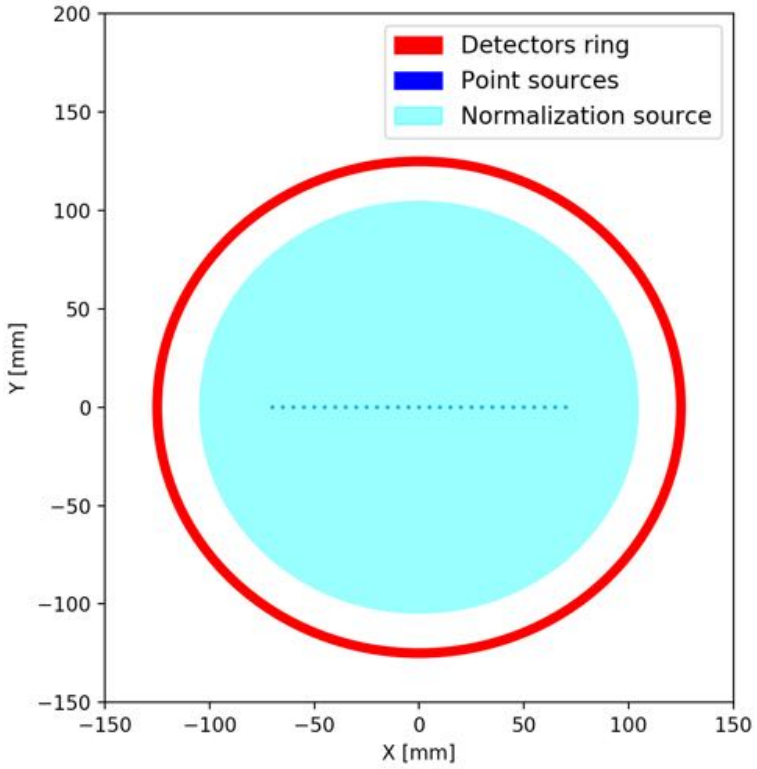

FIGURE 8.6. Positioning of the point sources in the GATE simulation.

provided by the system. It consists in placing all events at a fixed depth along the scintillator main axis. The most common possibilities are positioning the events at the beginning or at the half length of the crystal. The latter is adopted in this study. The second one represents the perfect situation in which DOI information is known exactly with an infinite resolution. This means that no gaussian smearing is applied to the data. Even if it is an unfeasible condition, it is an ideal reference to evaluate the effect of different DOI resolution. The third one corresponds to the 3 mm FWHM resolution of the proposed module.

Only one simulation is run and the same dataset is re-elaborated with the C++ code to obtain the different DOI configurations. For each of them, the ClearPEM algorithm is applied to reconstruct the activity distribution. The results are shown in Fig. 8.8, Fig. 8.7 and Fig. 8.9 respectively for the perfect positioning of the event along the crystal main axis, the fixed positioning at the half of the length of the scintillator and for the positioning with the 3 mm FWHM DOI resolution. Furthermore, a profile is drawn for each reconstruction image along the line where point sources rely.

As expected, compared to the reference image with perfect events positioning, the image without DOI information presents a spatial resolution degradation due to parallax error. The effect is

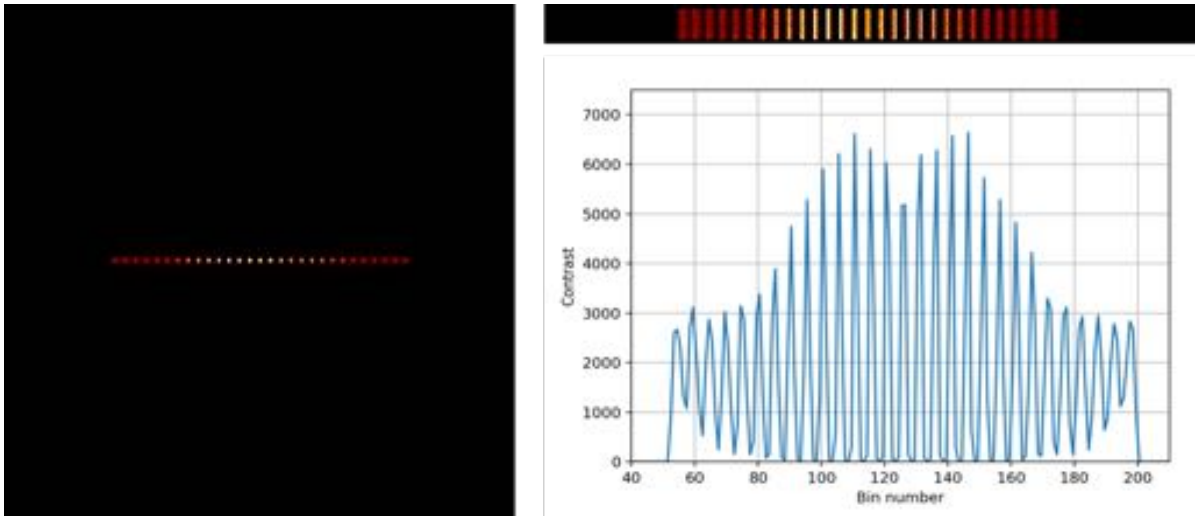

FIGURE 8.7. Results of the image reconstruction with no DOI information. In particular, the coronal and the transversal views are displayed with the profile of the sources in the transversal plane.

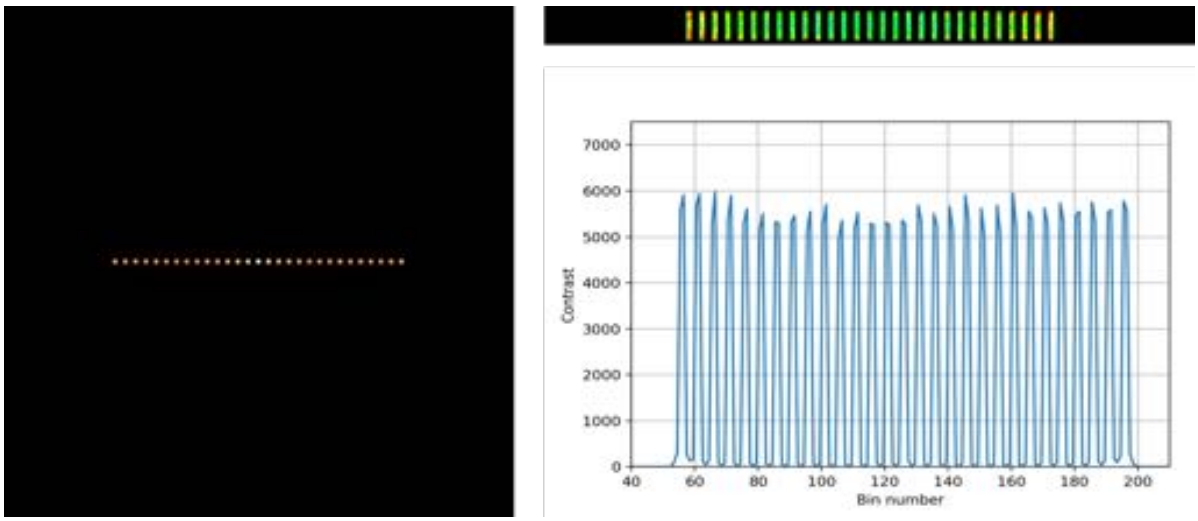

FIGURE 8.8. Results of the image reconstruction with an infinite DOI resolution. In particular, the coronal and the transversal views are displayed with the profile of the sources in the transversal plane.

stronger when the activity comes far from the FOV center. This effect is mitigated by introducing the DOI information as it is possible to observe in Fig. 8.9. To quantify the benefits of achieving DOI information, the analysis is focused on a source in the FOV center and one close to the edges.

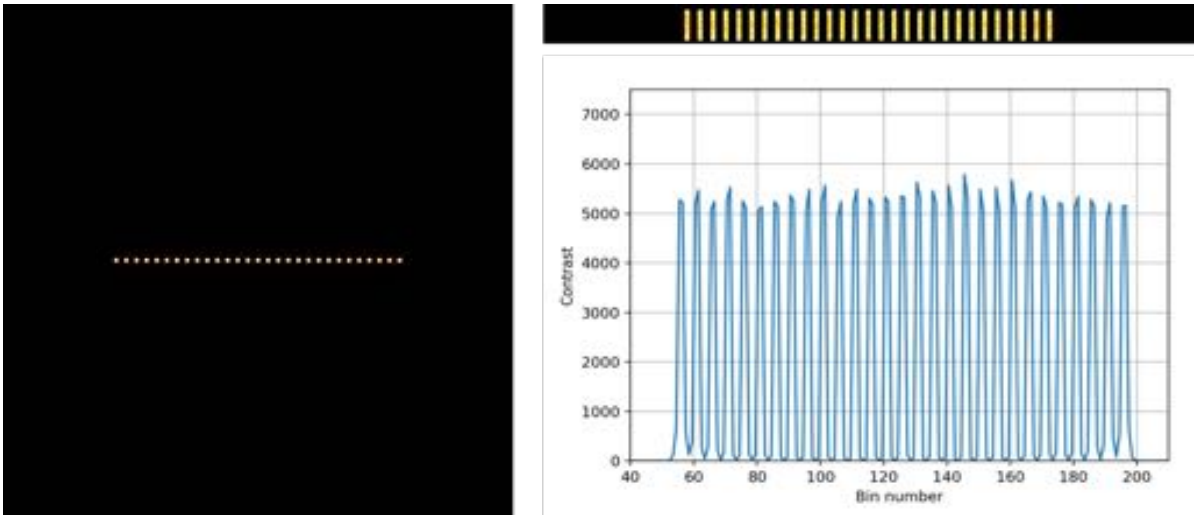

FIGURE 8.9. Results of the image reconstruction with 3 mm FWHM DOI resolution. In particular, the coronal and the transversal views are displayed with the profile of the sources in the transversal plane.

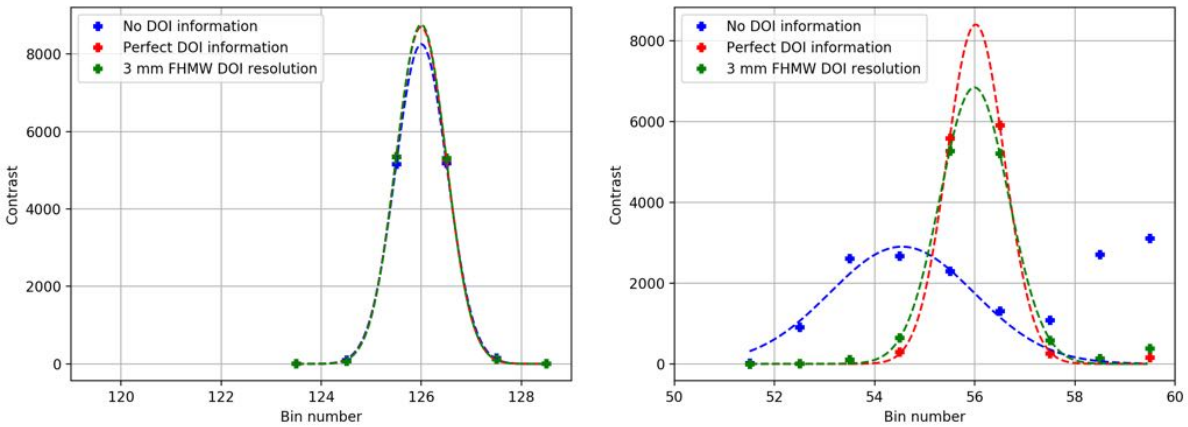

FIGURE 8.10. Comparison of the source profile in the center (left part) and at the edge (right part) of the FOV. In red the source profile when the DOI information is known with an infinite resolution, in green with a 3 mm FWHM resolution and in red when all the events are placed at the same position at the half length of the crystal along its main axis.

In the FOV center, the three different DOI configurations are reasonably comparable while it is not the case in the source close to the edges. If the DOI information is not provided, the activity peak is blurred and it merges with the close one. Also the position of the peak is incorrect. This

effect is reduced by DOI information which makes the peak profile still comparable with the reference one. By performing a gaussian fit of the peaks it is possible to perform a quantitative study summarized in the Tab. 8.3. The quantitative analysis confirms no substantial differences as long as the activity is placed in the center of the FOV. Close to edges, the FWHM degrades from 1.35 mm for the reference DOI resolution to 3.4 mm with no DOI information provided. An offset of 1.5 mm is also introduced. This behavior is mitigated by reaching 3 mm FWHM DOI resolution which returns a FWHM of 1.61 mm. From this analysis, it is possible to evaluate the spatial resolution of the proposed 8x8 LYSO crystals module. The spatial resolution is in the order of 1.2 mm FWHM which degrades to 1.6 mm at FOV edges.

	Central Source (Bin position 126)	Lateral Source) (Bin position 56)
Perfect DOI information		
Peak Position	125.996 ± 0.002	56.017 ± 0.008
FWHM	1.19 ± 0.03	1.35± 0.05
No DOI information		
Peak Position	126.001 ± 0.002	54.5 ± 0.1
FWHM	1.22 ± 0.02	3.4± 0.4
3 mm FWHM DOI resolution		
Peak Position	125.999 ± 0.001	55.99 ± 0.02
FWHM	1.18 ± 0.02	1.61± 0.08

TABLE 8.1. The evaluation of the parallax effect for the different DOI configuration for a source placed in the FOV center (bin position 126) and a source close to the FOV edges (bin position 56).

8.4 Evaluation of TOFPET reconstruction

In this section, the TOF reconstruction study by using the upgraded version of the ClearPEM algorithm is presented. In order to avoid misunderstanding, DOI resolution is set to 3 mm FWHM for all simulations. Also the scanner ring geometry is slightly modified. The total number of detector drops from 60 to 30 with the presence of gaps between each component. Each gap has the dimension of a module. The reason for these gaps is related to the effect of timing information in reconstruction processes. TOF approach recovers information that is lost in a conventional non TOF approach. For example, a more accurate positioning of the positron-electron annihilation point is provided. Keeping in mind that in this simulation environment there are no scatter or attenuation effects, having a complete FOV coverage leads to a faster convergence of reconstructed images. On the other hand, artifacts can arise in non TOF reconstruction in a gaps configuration and the timing information can mitigate this effect increasing the image quality.
It is necessary to define parameters which contain information useful to compare different images and to quantify the quality of the reconstruction results. Already discussed parameters are the mean value of the activity regions and the standard deviation. They act as indicator of signal convergence and noise level. An additional parameter is the signal to noise ratio (SNR) defined as in the work of S. Surti and J.S. Karp "Design considerations for a limited-angle, dedicated breast, TOF PET scanner" [17] presented in 2008. The SNR is defined as follow:

$$SNR = \frac{\frac{C_S}{C_B} - 1}{\sqrt{\left(\frac{\sigma_S}{C_S}\right)^2 + \left(\frac{\sigma_B}{C_B}\right)^2}} \tag{8.1}$$

where C_S and C_B are the mean counts in signal and background ROIs while σ_S and σ_B are the counts standard deviation. Following the work of C. J. Groiselle and S. J. Glick entitled "3D PET list-mode iterative reconstruction using time-of-flight information" [28], the chosen source for this study consists in 6 hot cylindrical sources with a diameter of 10 mm placed in a radioactive background with a diameter of 160 mm. The sources are positioned uniformly on an ideal 40 mm radius circumference inside the background source as presented in the left part Fig. 8.11. The activity concentration is higher in hot sources than in the background. It is set to 5:1 as it is possible to observe in the profile plot in the right part of Fig. 8.11.
On reconstructed images, the values of C_S, C_B, σ_S and σ_B need to be evaluated starting from the definition of signal and background ROIs. For the signal evaluation, the natural choice is to consider the entire volume of the hot sources. Signals ROIs are therefore 6 regions with exact dimensions and placed in the same position as the hot sources. Ideally, also for the background region it is possible to follow the same method but it is not the most suitable choice. Having a small dimension of 10 mm diameter opens the possibility to confuse possible artifact as the background overestimating or underestimating the SNR expressed in Eq. 8.1. The best configuration is to consider ROIs in between two consequent hot sources with a diameter that covers the

entire distance between them. Thanks to this approach the mistakes of identifying artifact as background is confined.

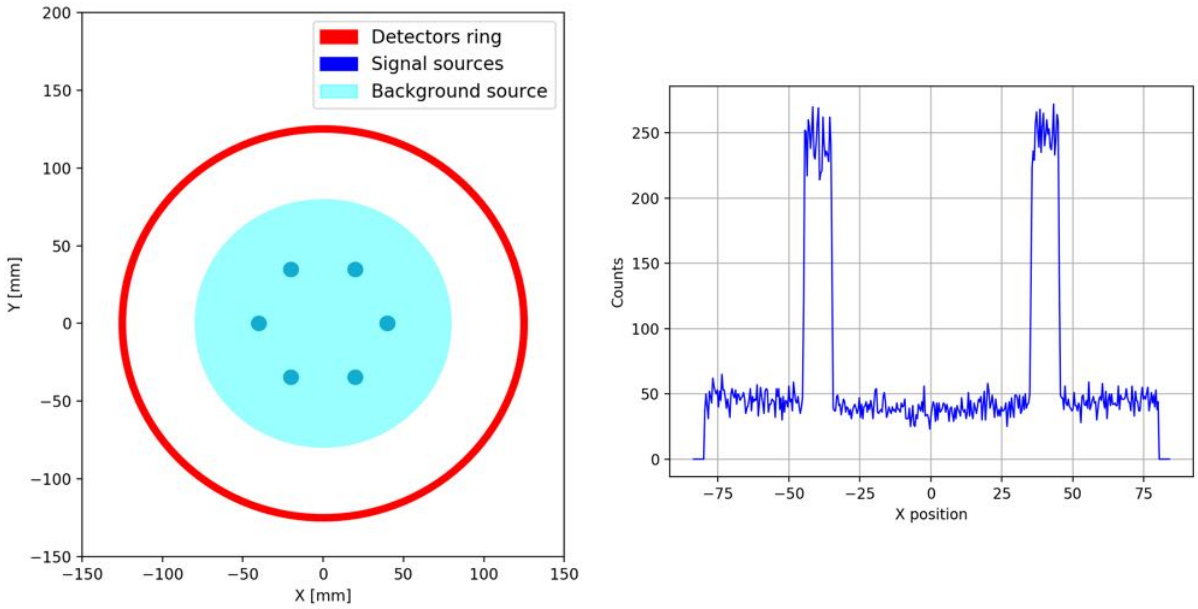

FIGURE 8.11. Visual description of the source simulated for the TOF reconstruction study. On the left part the positioning of the sources. It worth to notice that the normalization source is not displayed anymore. On the right part a profile that underlines the different activity concentrations between the hot sources and the background.

The analysis is performed with different timing resolutions. In particular, the study starts from a non TOF reconstruction that is considered the reference model and it explores 400 ps, 200 ps, 100 ps and 50 ps of CTR (FWHM) of the system. The simulation allows us also to test the ultimate timing resolution of 10 ps and a part of this section is later dedicated to reconstruction processes with this challenging timing performance.
Two simulations are needed to perform this study. One consists in an acquisition with the source described above in Fig. 8.11 while the second one is a longer simulation with the normalization source. For the different timing resolution the simulation output is the same but it is re-elaborated by a C++ code. The dataset from simulations contains the information of the perfect time difference of detected gamma rays. A gaussian smearing is applied in order to match the desired timing performances. Also the results of the normalization source acquisition are treated separately for each time resolution. FOV sensitivity, in fact, changes according to the precision with which time information is known.
The results of the reconstruction with different resolutions are displayed in Fig. 8.12 after 4 iterations. Just by a qualitative comparison, it is evident the improvement of the image quality for better timing resolution. As soon as a CTR value of 200 ps FWHM is reached, the presence

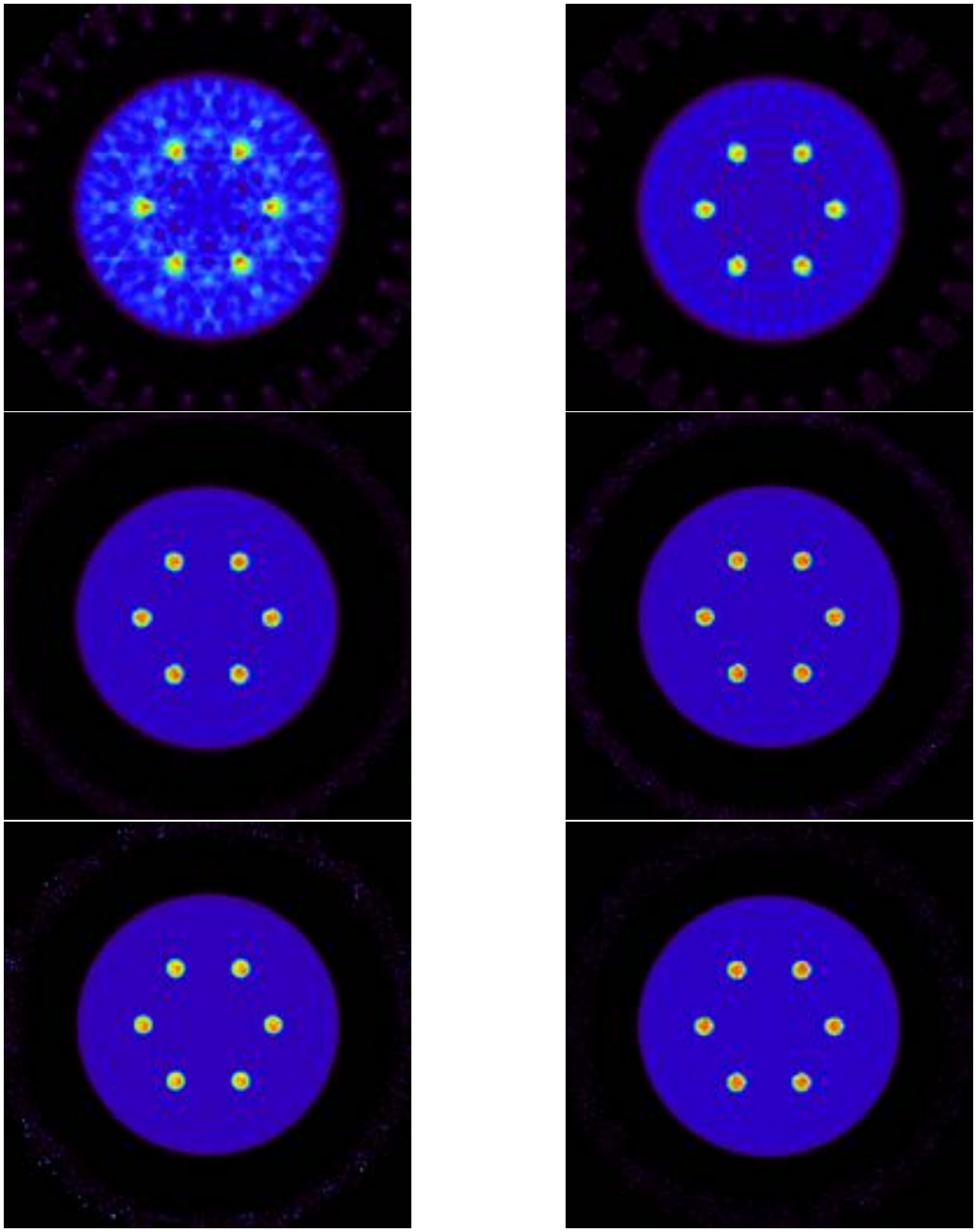

FIGURE 8.12. Reconstructed images with different timing resolutions. All the images are obtained after 4 iterations of the reconstruction algorithm. Starting from the top left part there is the results of non TOF, 400ps, 200 ps, 100 ps, 50 ps and 10 ps CTR (FWHM).

of artifacts in the reconstructed images is drastically reduced. To conduct a quantitative study the analysis on the signal and background ROIs needs to be addressed and particular attention has to be dedicated to the mean counts and the SNR value as functions of the number of the

iterations as presented in Fig. 8.13.

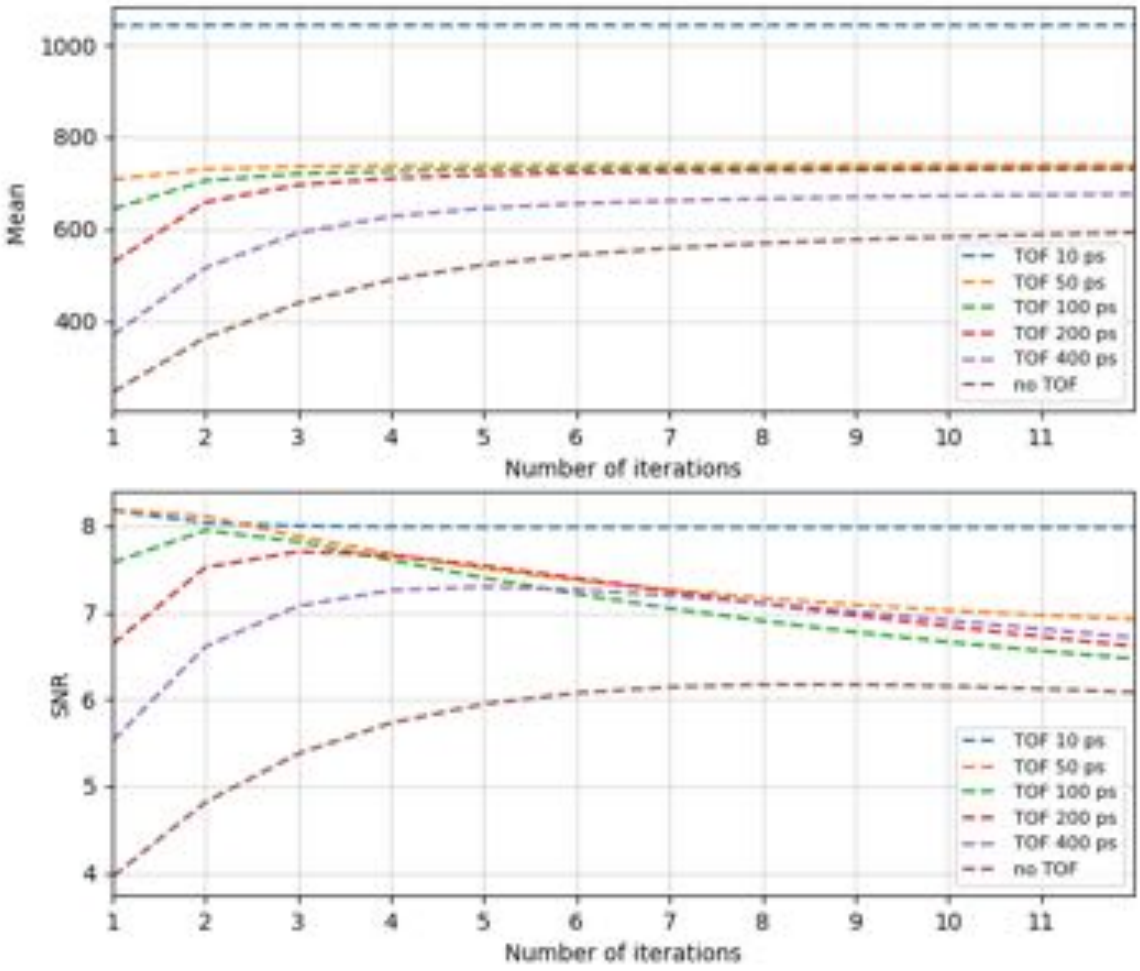

FIGURE 8.13. Behavior of the mean counts and the SNR as a function of the iterations number for different timing performances.

It can be appreciated a faster signal convergence for higher timing resolutions. This means that the computing time needed to obtain high quality images is reduced. From the SNR trend, the benefits of exploiting TOF reconstruction are proven returning a better contrast between signal and noise regions. To quantify the SNR gain, the ratio between the value obtained with different timing resolutions and non TOF approach can be computed as a function of the iterations number as presented in Fig. 8.14.

The results shown in this plot represent the SNR gain at same iteration number and it includes the algorithm convergence time improvement. In other words, it means that the best SNR value is reached at different iteration number for different timing resolutions. In order to remove the

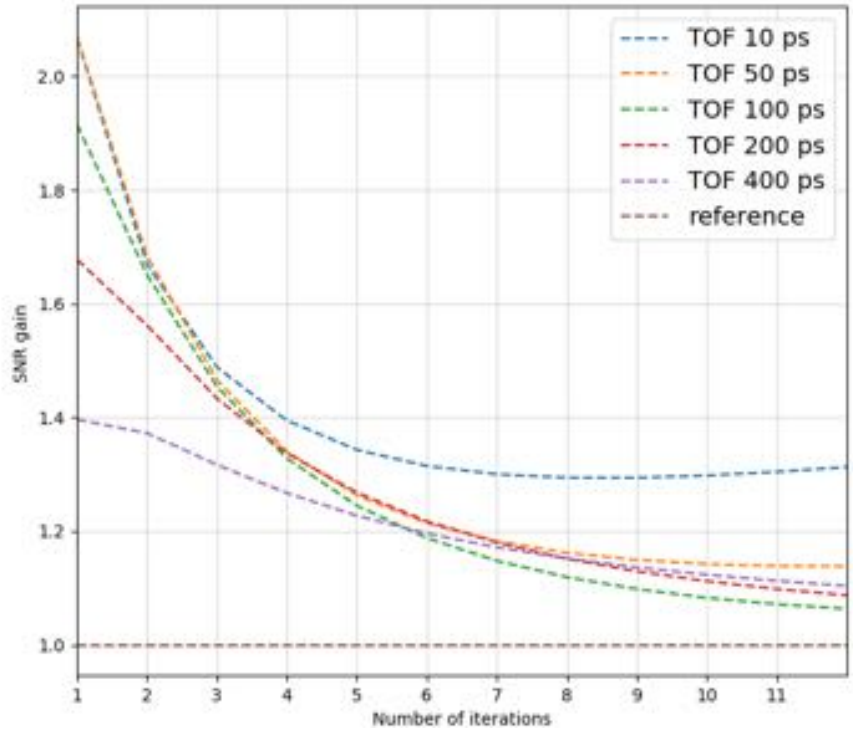

FIGURE 8.14. Gain in the SNR for the different timing resolution as a function of the iteration number.

effect of the different convergence time, the ratio between the higher value of SNR for each timing resolution and the one of the non TOF approach has to be computed and the results are shown in the Tab. 8.2. The results show a clear improvement in the SNR but far from the theoretical ones evaluated by Eq. 2.16 and reported in Tab. 2.2. The reason for this deviation has to be found in the idea that the TOF approach is more efficient when there is information that is not provided by the usual non TOF method. Usually, this lack of information or uncertainties arises from scatter or random events and in a low statistics collection of data. Our simulation excludes both scatter and random events but it is possible to play with the number of coincidence events. The results are shown in the Tab. 8.2 for 50% and 10% of the number of the LORs included in the previous reconstruction. In details, a reduction in the number of LORs emphasizes the effect of the TOF approach.

For reconstruction at 10 ps FWHM timing resolution, the results presented till now are comparable with the ones at 50 ps. Clearly, the reconstructed image at 10 ps has an immediate convergence but it does not affect the SNR gain as expected. A possible explanation for this behavior is the idea that reaching the uncertainty of 1.5 mm in the annihilation point positioning makes the tomography reconstruction inefficient. It defines the so called reconstruction-less PET approach. The image can be reconstructed as 3D histogram of activity distribution which is built

Timing resolution (FWHM)	SNR absolute gain	SNR absolute gain (50 % of the LORs)	SNR absolute gain (10 % of the LORs)
400 ps	1.18	1.21	1.27
200 ps	1.24	1.28	1.39
100 ps	1.28	1.32	1.46
50 ps	1.33	1.38	1.51
10 ps	1.32	1.37	1.43

TABLE 8.2. SNR gain for the different timing resolutions.

in real time. This opens the possibility to decide the PET examination duration in real time. This approach is far from being realized for two main reasons. The first one is that the current PET scanners are not even in the order of magnitude of such a high timing resolution. The second one regards attenuation, scatter and random corrections that, at the current status of the art, require still a tomography based approach.

After the study of the scanner geometry with detectors ring configuration, it is interesting to examine another system configuration based on two plates geometry without rotations. The reason to start studying this system is the possibility to perform organ dedicated examination, for example in the abdominal region, reducing the distance between the targeted organ and the detectors as suggested by S. Surti and J.S. Karp in the work "Design considerations for a limited-angle, dedicated breast, TOF PET scanner". Furthermore, in such a limited angle geometry system, timing performances play a central role in the images quality and the SNR gain can only be emphasized. In simulation, this two plates configuration is reached activating only 15 detectors on one side and the correspondent 15 on the other in the no gaps configuration presented in Fig. 8.2. According to a full ring system with 60 detectors, in this configuration the acceptance angle is reduced by a factor two. The same study previously discussed is performed and the results of the reconstructed images can be observed in Fig. 8.15.

As expected the results are different from the gaps configuration. In particular non TOF approach leads to a failure in reconstructing the activity distribution. In details, background regions are not reconstructed as a uniform activity distribution. It presents a higher contrast in the regions close to the detectors while a lower one in the center of the FOV. In this situation, introducing time information is mandatory to obtain the images with a proper quality. In particular, the presence of artifacts is removed only when the timing resolution drops below 100 ps FWHM. The same analysis of the SNR and of the convergence previously presented can be performed also on these images except for the non TOF approach. Evaluating the mean and the standard deviation for the signal and noise ROIs results in an overestimation of the SNR when these values are evaluated in a lower activity region and vice versa. The results are presented in Fig. 8.16.

The SNR curves for each timing resolution are more separated if compared to the ones obtained in the gaps geometry presented before in Fig. 8.13. Even if it is not possible to access directly the

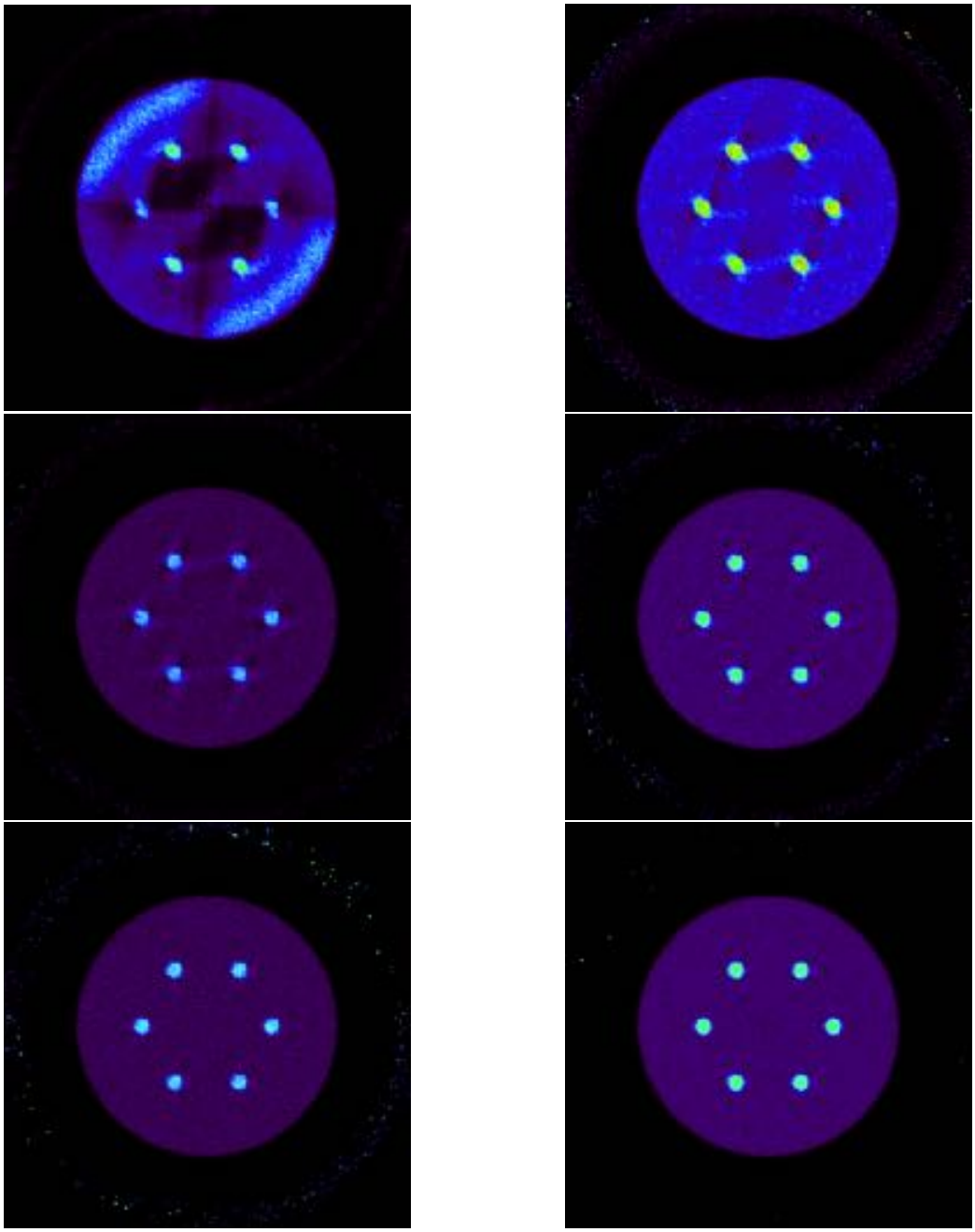

FIGURE 8.15. Reconstructed images with different timing resolutions for the two plates geometry. All the images are obtained after 4 iterations of the reconstruction algorithm. Starting from the top left part there is the results of non TOF, 400ps, 200 ps, 100 ps, 50 ps and 10 ps CTR (FWHM).

SNR gain due to the fact that it can not be calculated for the non TOF approach, it is undeniable the central role played by timing information in limited angle geometry. After the previous study about the statistics of the acquisition, the idea that the TOF reconstruction method is more

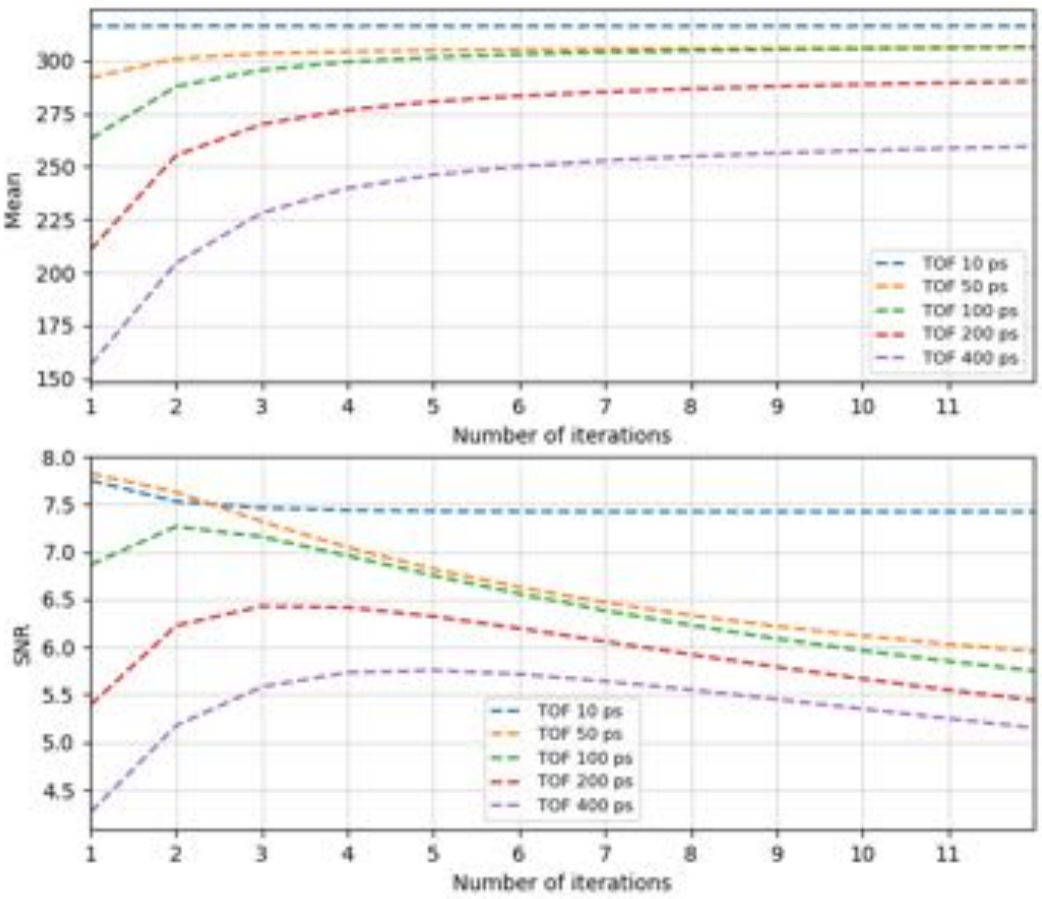

FIGURE 8.16. Behavior of the mean counts and the SNR as a function of the iterations number for different timing performances for the two plates geometry.

efficient in a configuration where some informations are not collected is further confirmed.
The improvement of the SNR has also an effect on the spatial resolution and in the resolving power of the system. The source was used before is not the perfect candidate for this kind of evaluation due to the dimension and the distance of the hot cylindrical sources placed in the background. A well know method is to take the advantage of a Derenzo phantom that consists in several cylindrical sources with different dimensions and different distance between them. It is possible to observe it in Fig. 8.17 obtained directly by simulation from the (x, y) emission position of two back-to-back gamma rays.
The technical features of the Derenzo phantom are shown in the Tab. 8.3 and each source has the same activity density. In order to compare the TOF and non TOF approaches, the simulation geometry is the gaps configuration presented above. As a reminder, this configuration presents 30 modules with a gap of module dimension between two consecutive ones.

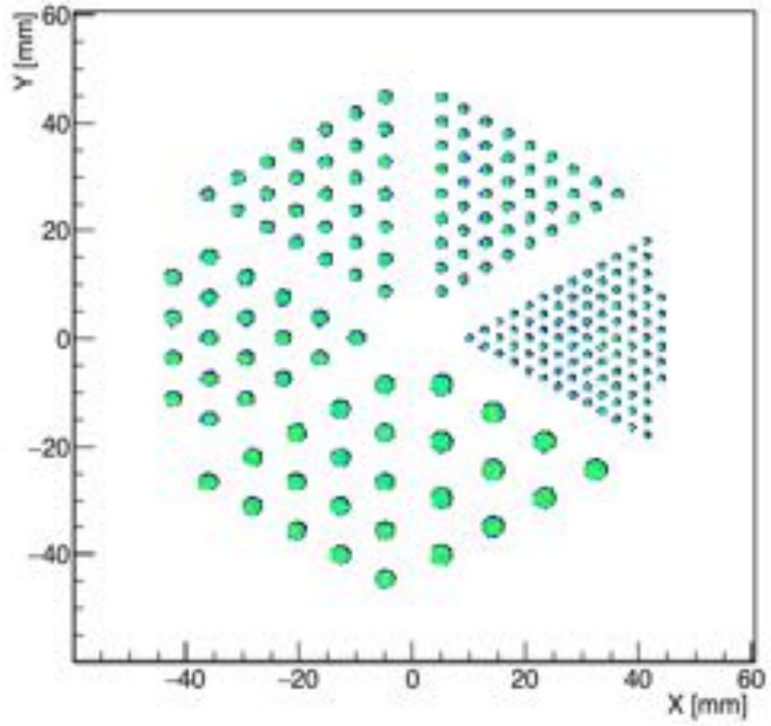

FIGURE 8.17. Scheme of the Derenzo phantom geometry.

Radius of the source	Distance between the centers of the sources
0.5 mm	3 mm
0.75 mm	5 mm
1 mm	6 mm
1.25 mm	7 mm
1.5 mm	8 mm
1.75 mm	9 mm

TABLE 8.3. Derenzo phantom dimensions.

Reconstruction results are presented in Fig. 8.18 with a zoom on the smallest sources in Fig. 8.19. From these reconstructed images, it is possible to appreciate that the SNR improvement has a beneficial effect on the resolving power of the system enhancing the spatial resolution. The sources with a radius of 0.75 mm are not distinguishable until a timing resolution of 200 ps FWHM is achieved. The separation quality improves according to the timing performances. It is worth to notice that, even if it is not possible to observe an evident difference between 50 ps FWHM and 10 ps FWHM timing resolution in the SNR study, the Derenzo phantom results show a better separation of the smallest sources with 10 ps FWHM CTR. In particular, the halo around each source is reduced allowing to better recognize all the sources. This is an effect that

was not possible to be observed before due to a larger distance between the sources.
To conclude this chapter, several achievements have to be enumerated. The first one is the development of a reconstruction algorithm, based on the ClearPEM one, able to include DOI and timing information. Thanks to this algorithm a complete study of parallax error effect in a small PET device is presented stating the importance of achieving good DOI resolution. Furthermore, an intensive description of the images quality performances as a function of timing resolution value is addressed showing the importance of TOF approach. This is the only feasible approach in the case of a dual plates geometry without rotations.

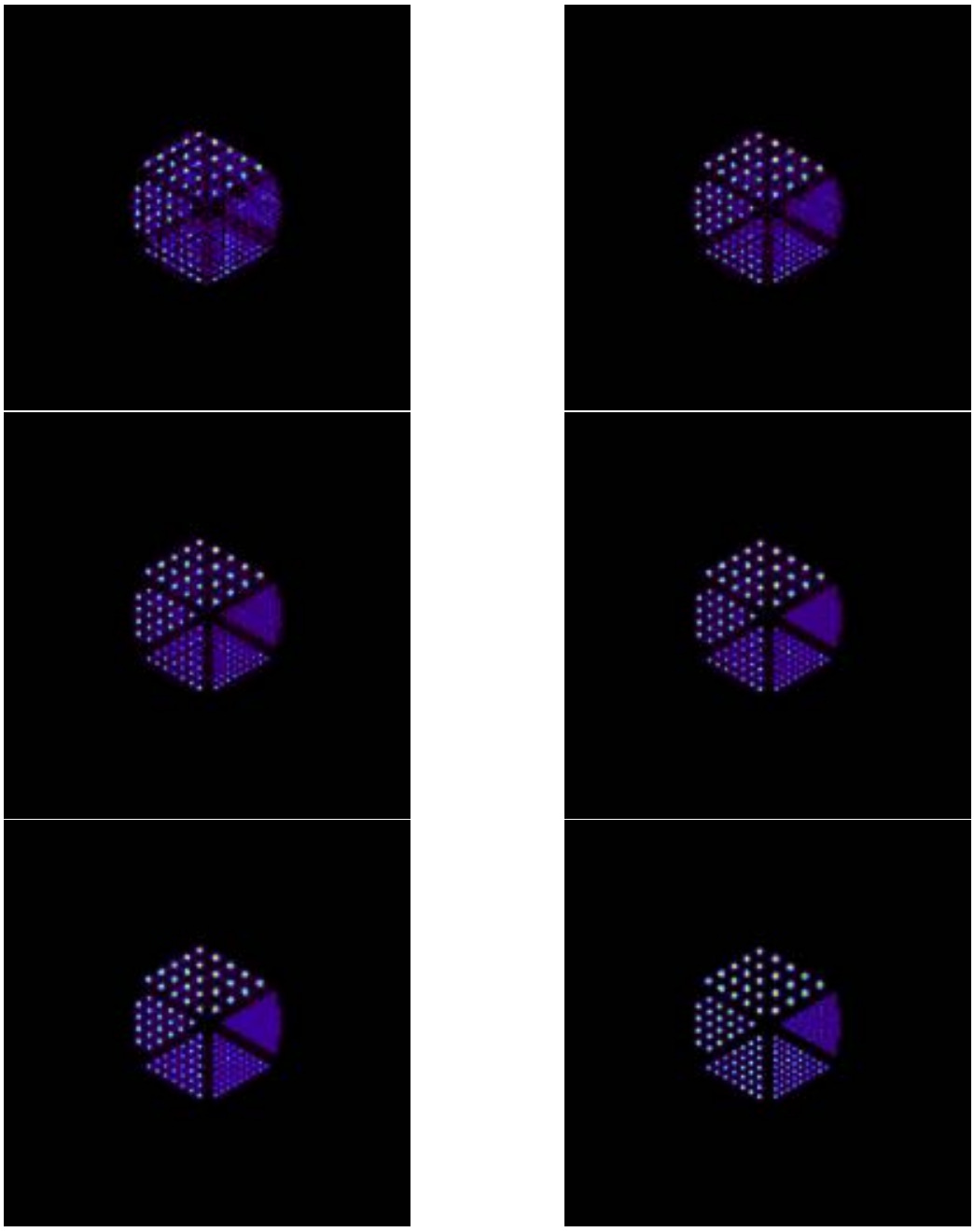

FIGURE 8.18. Derenzo reconstructed images with different timing resolutions. Starting from the top left part there is the results of non TOF, 400ps, 200 ps, 100 ps, 50 ps and 10 ps CTR (FWHM).

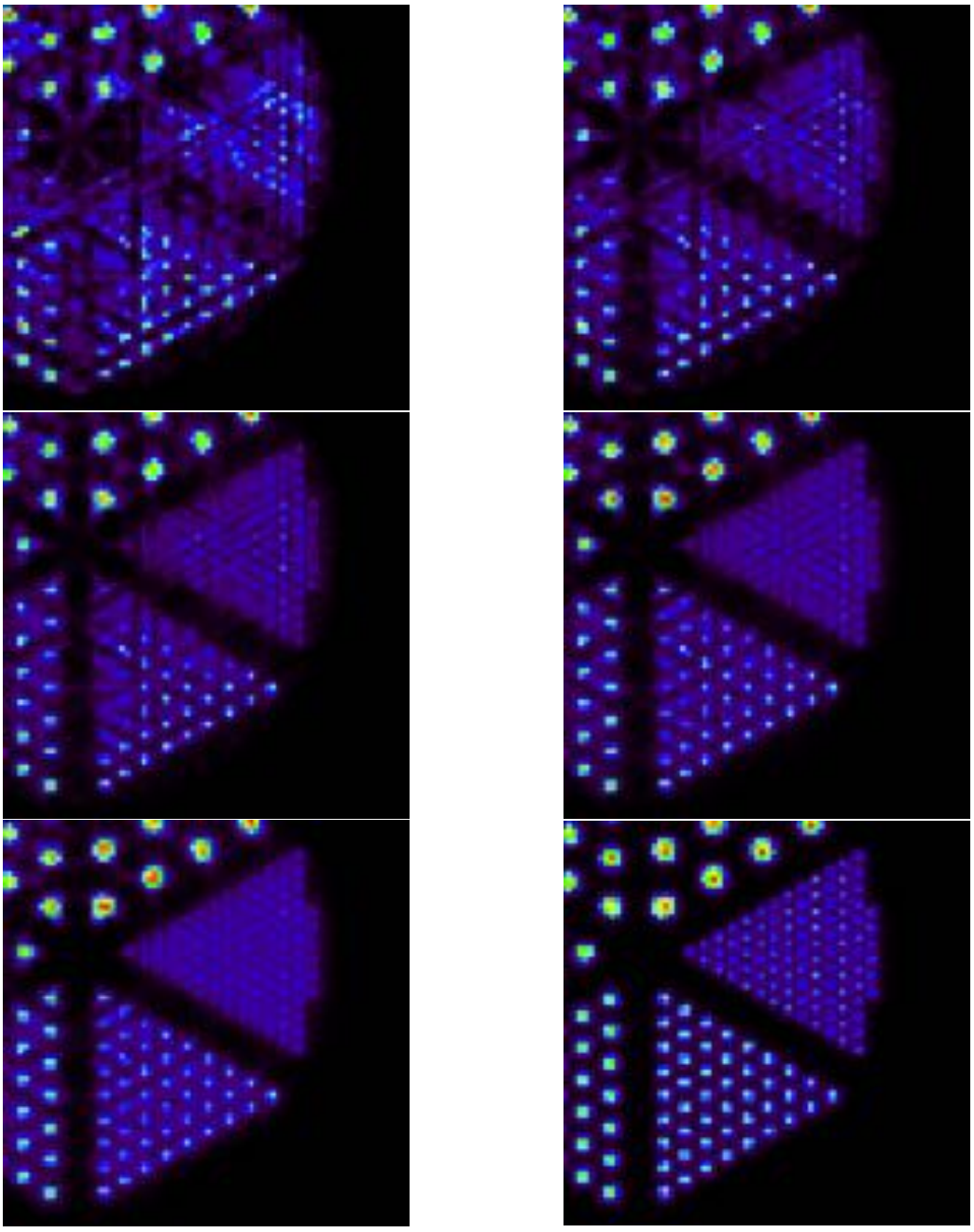

FIGURE 8.19. Details of the Derenzo reconstructed images with different timing resolutions. Starting from the top left part there is the results of non TOF, 400ps, 200 ps, 100 ps, 50 ps and 10 ps CTR (FWHM).

CHAPTER 9

CONCLUSIONS

In PET applications, reaching high performances in term of energy, DOI and timing resolution is the key to recover high quality metabolic images. In oncology, these images play a fundamental role in tumor lesions diagnosis recovering the anomalies in glucose absorption. Furthermore, PET scanners costs and complexity have to be maintained reasonably low in order to make them accessible and suitable for hospital facilities. In this work, a new method to achieve high performances in pixellated PET modules is presented based on light sharing mechanism. Thanks to this mechanism, a single side readout configuration is adopted based on the recirculation and spread of optical light in crystals. Studying the light distribution, it is possible to adopt greater than one to one coupling between scintillators and detector improving the system spatial resolution without increasing the channel needed for the readout. Furthermore, DOI information is achieved by exploiting the shared light and an attenuation behavior over the crystal length reaching 3-4 mm FWHM resolution. A DOI based clustering algorithm is developed to separate the single crystal spectrum and DOI information is also included in the evaluation of the energy performances. Samples with four and nine to one coupling are successfully tested showing good identification of the crystals in which the gamma ray interaction takes place and an energy resolution in the order of 12-15%. In addition, a DOI calibration method is presented suitable for application on complete assembled devices in hospitals facilities. Timing performances are measured in the order of 350 ps FWHM thanks to a DOI based correction able to mitigate the negative effect of depolishing on timing. Furthermore, the DOI correction of the timing performances is not fully exploited due to limitations in the electronic setup. With a dedicated acquisition chain which is able to collect both the time and charge information, the timing resolution could be improved reaching the benchmark of 249 ps of the Siemens Biograph Vision.
The presented PET module prototypes are good candidates for small animal or organ dedicated

PET devices (8x8 LYSO matrix) or for whole body PET scanner (4x4 LYSO matrix).
A dedicated algorithm is developed to reconstruct metabolic images based on Siddon's algorithm and ML-EM technique. The importance of DOI information is tested in a small FOV geometry showing the parallax error mitigation. From simulations, it is possible to evaluate the spatial resolution of the system which is between 1.18 (FOV center) and 1.61 (FOV edges). Comparing these results to the available preclinical PET devices, it is possible to observe an improvement in the performances.
The software includes not only DOI but also timing information in reconstruction processes. This opens the possibility to perform a complete simulation study on the effect of timing performances in images quality. In particular, the results show better reconstructed images according to SNR and signal convergence in a ring detectors geometry. Thanks to this study, the need of having the timing information is confirmed for limited angle coverage systems in which conventional non TOF approach is not able to provide metabolic images. This result opens the possibility for development of abdominal region dedicated scanners based on two plates without rotations but with a reduced distance from the targeted organ.

BIBLIOGRAPHY

[1] P. J. Slomka, T. Pan and G. Germano. **Recent Advances and Future Progress in PET Instrumentation**. Seminars in Nuclear Medicine, Vol. 46, 2016.

[2] A. L. Goertzen et al. **NEMA NU 4-2008 Comparison of Preclinical PET Imaging Systems**. J Nucl Med Vol. 53, 2012.

[3] Knoll, Glenn F. **Radiation detection and measurement**. John Wiley, 4th edition, 2010.

[4] C. Kittel. **Introduction to solid state Physiscs**. John Wiley, 8th edition, 2004.

[5] H. Suzuki and T. A. Tombrello. **Light Emission Mechanism of $Lu_2(SiO_4)O$:Ce**. IEEE TRANSACTION IN NUCLEAR SCIENCE, Vol. 40, 1993.

[6] J. D. Naud et al. **The Role of Cerium Sites in the Scintillation Mechanism of LSO**. IEEE TRANSACTION IN NUCLEAR SCIENCE, Vol. 43, 1996.

[7] SensL. **Introduction to SiPM**.

[8] E. Garutti. **Silicon Photomultipliers for High Energy Physics Detectors**. arXiv:1108.3166v2, [physics.ins-det], 22 Sep 2011.

[9] A. Del Guerra, N. Belcari and M. Bisogni. **Positron Emission Tomography: Its 65 years**. Riv. Nuovo Cimento, 39, 2016.

[10] M. Pizzichemi. **Positron Emission Tomography: state of the art and future developments**. JINST, Vol 11, 2016.

[11] D. Schaart et al. **Sub-200 ps CRT in monolithic scintillator PET detectors using digital SiPM arrays and maximum likelihood interaction time estimation**. Physics in Medicine and Biology, Vol. 58, 2013.

[12] J.A. Neves et al. **The ClearPEM breast imaging scanner**. Nuclear Instruments and Methods in Physics Research A 628, 2011.

[13] M. Zvolsky et al. **EndoTOFPET-US - A Miniaturised Calorimeter for Endoscopic Time-of-Flight Positron Emission Tomography**. Journal of Physics: Conference Series 587, 2015.

[14] C. Levin. **Design of a high-resolution and high-sensitivity scintillation crystal array for PET with nearly complete light collection**. IEEE TRANSACTION IN NUCLEAR SCIENCE, Vol. 49 , 2002.

[15] J. S. Karp and M. E. Daube-Witherspoon. **Depth-of-interaction determination in NaI(TL) and BGO scintillation crystals using a temperature gradient**. Nuclear Instruments and Methods in Physics Research A 260, 1987.

[16] R. Bugalho et al. **Experimental characterization of the Clear-PEM scanner spectrometric performance**. Journal of Instrumentation, Vol. 4, 2009

[17] S. Surti and J.S. Karp. **Design considerations for a limited-angle, dedicated breast, TOF PET scanner**. Physica Medica 32, 2016.

[18] A. Alessio and P. Kinahan. **PET image reconstruction**. Nuclear medicine 1, 2006.

[19] L. A. Shepp and Y. Vardi. **Maximum likelihood reconstruction for emission tomography**. IEEE TRANSACTIONS ON MEDICAL IMAGING 1, no. 2, 1982.

[20] B. Frisch et. al. **Towards Multimodal Positron Emission Mammography and Ultrasonography: the ClearPEM-Sonic Project**. IEEE TRANSACTIONS ON MEDICAL IMAGING, 2013.

[21] R. L. Siddon. **Fast calculation of the exact radiological path for a three-dimensional CT array**. Medical Physics, Vol.12, N. 2, 1984.

[22] H. O. Anger **Scintillation camera**. Review of Scientific Instruments, Vol. 29, 1958.

[23] M. Pizzichemi et al. **A new method for depth of interaction determination in PET detectors**. Physics in Medicine and Biology, Vol. 61, 2016.

[24] F. Anghinolfi et al. **NINO: An Ultrafast Low-Power Front-End Amplifier Discriminator for the Time-of-Flight Detector in the ALICE Experiment**. IEEE TRANSACTION IN NUCLEAR SCIENCE, NO. 5, Vol. 51, 2004.

[25] Y. Shao, R. Yao and T. Ma **A novel method to calibrate DOI function of a PET detector with a dual ended scintillator readout**. Physics in Medicine and Biology, Vol. 35, 2008.

[26] G. Stringhini et al. **Development and evaluation of a practical method to measure the Depth of Interaction function for a single side readout PET detector**. JINST, Vol. 11, 2016.

[27] S. Jan et al. **GATE: a simulation toolkit for PET and SPECT**. Physics in Medicine and Biology, Vol. 49, 2004.

[28] C. J. Groiselle and S. J. Glick. **3D PET List-Mode Iterative Reconstruction Using Time-Of-Flight Information**. IEEE Symposium Conference Record Nuclear Science, 2004.